Investigation of Heavy Ion Reaction Mechanisms by Means of the Inclusive ^{93}Nb(^{12}C,^{7}Be) and ^{93}Nb(^{12}C,^{9}Be) Reactions

Bruce Becker

A thesis submitted to the Faculty of Science,
University of Cape Town

Cape Town, 2002

I declare that this thesis is my own, unaided work.
It is being submitted for the degree of Master of
Science at the University of Cape Town.
It has not been submitted for any degree or examination
at any other university.

_____

_____ day of _____ 2002

Abstract

Inclusive continuum cross-sections for the reactions ^{93}Nb(^{12}C,^{7}Be) and ^{93}Nb(^{12}C,^{9}Be) were measured at the NAC using a $\Delta E - E$ setup. A theoretical light output model which could account for the mass and charge dependance of the NaI E detectors was employed to calibrate the NaI(Tl) detectors. The model is outlined and it is shown that the nonlinearity of the detector response is only due to a term which describes the mass-dependance.

Investigation of the cross-sections revealed interesting facts about the dominant reaction mechanisms in the interaction of ^{12}C with heavy targets. A theoretical model developed by the Milano group has been very successful in describing the continuum cross-sections of α particles (including ^{8}Be) created in similar reactions of ^{12}C and ^{16}O, incident on heavy targets. The analysis shows that the same description of the continuum cross-sections of ^{7}Be and ^{9}Be gives good agreement with the data (with different energy-loss parameters and survival probabilities), although there are discrepancies, especially at the lower incident angles. These small discrepancies may indicate the presence of a multistep direct reaction between the detected fragment and the residual nucleus in the exit channel.

The most notable result of the analysis of the data was that the spectra of ^{7}Be and ^{9}Be, previously suspected to be created in a final-state interaction of ^{8}Be with the residual nucleus, are well-described by a friction-dissipative breakup mechanism.

This work is dedicated to the living memory of

Dr. Duncan Mark Elliott,

whence I draw my daily inspiration:

"As a matter of fact, (Cephalus)" I said, "I enjoy talking to very old men, for they have gone before us, as it were, on a road that we too must probably tread, and it seems to me that we can find out from them what it is like and whether it is rough and difficult or broad and easy. You are now at an age when you are, as the poets say, about to cross the bar, and I would like to find out from you what you have to tell us..."

Plato, The Republic (Book I)

Il existe, dit-on, une philosophie
Qui nous explique tout sans révélation,
Et qui peut nous guider à travers cette vie
Entre l'indifférence et la religion
J'y consens—O'u sont-ils, ces faiseurs de systèmes,
Qui savent, sans la foi, trouver la vérité,
Sophistes impuissants qui ne croient qu'en eux-mêmes ...?

Je vois rêver Platon et penser Aristote;
J'écoute, j'applaudis et poursuit mon chemin.
Sous les rois absolus, je trouve un Dieu despote;
On nous parle aujourd'hui d'un Dieu républicain.
Pythagore et Leibniz transfigurent mon être.
Décartes m'abandonne au sein des tourbillons.
Montaigne s'examine, et ne peut se connaître.
Pascal fuit en tremblant ses propre visions.
Pyrrhon me rend aveugle, et Zénon insensible.
Voltaire jette à tout bas tout ce qu'il voit debout.
Spinoza fatigué de tenter l'impossible,
Cherchant en vain son Dieu, croit le trouver partout...

Voilà donc les débris de l'humaine science !

Alfred de Musset,

"Espoir en Dieu"

Contents

List of Figures

List of Tables

Chapter 1

Introduction

1.1 Overview and historical perspective

About twenty years ago, the physics of collisions between complex nuclei (so-called 'heavy-ion' physics) had developed into two branches. On the one hand, and somewhat surprisingly, these collisions had proven useful for spectroscopic studies, where Coulomb excitation, inelastic scattering, nucleon transfer and capture and fusion reactions were established as tools for populating nuclei in the $Z - N$ plane (away from the valley of stability) and investigating the properties of the residual nuclei.

On the other hand, the main hope of the study of interactions between two large pieces of nuclear matter, in order to learn something of the bulk properties of the nucleus, had found a fulfilment in the discovery and exploration of deep-inelastic collisions. In the case of deep-inelastic *scattering*, there was large momentum (or nucleon) transfer from the projectile to the target. In this type of collision, there is viewed to be an exchange of nucleons from both the projectile to the target and vice versa. In some views, the nuclei are seen to first come into contact with each other, then slide surface upon surface and slow down until they finally come to rest with respect to each other and then separate. Other authors envisage interpenetration of the two interacting nuclei to a large extent. Many macroscopic concepts have been successfully applied to these collisions, such as deformation, friction, temperature, *etc.*

(see *e.g.* the review by Schröder and Huizenga [1]).

One of the common tendencies of all branches of physics involving accelerators is to proceed to higher and higher energies. In the vein of research that is undertaken here, it seemed relevant to expose the nucleus to increasing stress, so that it would break up. Breaking apart, and the manner in which this happens, would yield more information on the nature of the nuclear cohesion. Such stress may be exerted by mechanical forces, heat and/or pressure. Whatever the case, it requires higher collision velocities.

Once the collision velocities started to reach the Fermi energy régime, it was widely expected that there would be a transition in reaction mechanism. Since the Fermi motion of nucleons in the nucleus mediates the response to a perturbation, in the case of collisions close to or exceeding the Fermi energy ($\sim 35A$ MeV), the nucleus will no longer respond as a whole to each change resulting from a collision. A portion of the nucleus may be easily removed, and there may be local heating or compression.

It was expected that the then familiar reaction mechanisms at low energy (below $10A$MeV) — fusion, deep-inelastic reactions, quasi-elastic transfer — would disappear and indeed, the fusion cross-section (in terms of two completely amalgamating nuclei) was found to fade away between 2 and 20 AMeV above the Coulomb barrier. This point is illustrated in the reviews by Grégoire and Tamain (1986) [2] or Gelbke and Boal [3]. Transfer reactions only become impossible at energies where the momentum of the particle can no longer be contained by the field of the target, at about $200A$MeV. The formation of very hot nuclei and all sorts of hot nuclear subsystems are anticipated in this energy régime.

1.1.1 Direct fragmentation versus decaying hot zones

An observation made by Gelbke *et al.* [4] highlighted two themes which dominated discussion during the mid-nineties. Bombarding ^{208}Pb nuclei with ^{16}O projectiles of energy $20A$MeV, they found that the strength in forward-angle energy spectra of ejectiles with $Z > 8$ seemed to be concentrated at velocities close to that of the projectiles. The interesting property was the spread in the velocities about their mean value. Ex-

pressed by the linear momentum relationship $\sigma^2 = \langle m^2 \Delta v^2 \rangle$, this was found to depend approximately as $A_F \left(\frac{A_P - A_F}{A_P - 1} \right)$ on the fragment and projectile masses, A_F and A_P respectively, with a proportionality constant of approximately $\sigma_0^2 = (90 MeV/c)^2$. Two possible interpretations were discussed:

1. Part of the projectile containing $(A_P - A_F)$ nucleons is torn off of the incoming nucleus, while the remaining fragment (with A_F nucleons) continues on, essentially undisturbed. This fragment acts as a 'spectator', and its final momentum is the same as that which it had in the moment of dissociation due to the Fermi motion of the nucleons. This yields a momentum spread depending on A_F as above. From the known Fermi momentum, σ_0 is indeed calculated to be about 90 MeV/c [4]. It was assumed that the projectile remains in its ground state and the spectator stays unexcited or 'cold', up until the moment of separation. One may thus speak of 'cold fragmentation'.

2. Another possible interpretation of the momentum spread could be attributed to thermal particle emission from the projectile, which is now assumed to be excited above a certain temperature. This spread happens to follow the same mass dependence as above [5]. The measured width of the momentum spread constrained the available excitation energy to be shared amongst at most 6 nucleons - a 'hot spot' would have to be created in the nucleus.

The generally accepted interpretation is in favour of the first mechanism, but the two alternatives, 'cold fragmentation' and 'hot emitting subsystem' appear as interpretative opposites in most aspects of fragmentative nucleus-nucleus collisions.

1.2 Theoretical models for breakup

Adopting the picture of cold fragmentation as a starting point for our description of the fragmentation of the projectile, we can begin by constructing the simplest possible picture of fragmentation - the case of breakup into two pieces. Accordingly, we will review some theoretical attempts at describing this kind of breakup reaction.

1.2.1 DWBA approaches

The earliest attempts at describing heavy-ion breakup processes worked within the **D**istorted **W**ave **B**orn **A**pproximation (DWBA). The reaction is viewed in lowest order: breakup of the projectile is followed by the eventual (non-elastic) interaction of a fragment with the target. Using DWBA, Frölich *et al.* [6] and Udagawa *et al.* [7] identified two components in the projectile-like fragment (plf) spectra: a beam velocity component due to direct breakup and a lower-energy component due to transfer of the light projectile. An attempt was made later [8] to understand the α spectra as being caused by break-up followed by the fusion of the heavier fragment with the target, but could only roughly reproduce the high-energy part of the α spectra

McVoy and Nemes [9] proposed in 1980 a simplification on the full-scale DWBA. It was shown that a local momentum (Coulomb corrected) plane-wave Born approximation (LMPWBA) could reproduce the DWBA results rather well. Using this approximation, Hussein *et al.* [10] managed to decompose the plf spectra from 315 MeV ^{16}O on ^{208}Pb into three components: direct break-up, breakup followed by inelastic scattering and a 'multi-step' reaction component.

Of course, we are dealing with a perturbation theory, so it is only reasonable to expect these models to work for peripheral collisions. Also, it is necessary to have a good wavefunction to describe the internal motion of the two fragments in the projectile, in order to formulate the break-up amplitude (see chapter 4). It is for this last reason that breakup models were only initially formulated for fragments no heavier than α particles.

1.3 Experiment PR 51 and the Milano group

The interaction of ^{12}C and ^{16}O with heavy targets has been investigated before by our group [11, 12, 13, 14] when studying various reaction mechanisms. Advances were made in the description of the cross-sections and relative importance of various components, such as elastic and inelastic break-up, pre-equilibrium emission, nuclear friction, *etc.*

Investigation of the double-differential cross-section $\frac{d^2\sigma}{dEd\Omega}$ of α fragments emitted in the interaction of ^{12}C with ^{93}Nb and ^{59}Co revealed many refinements of the perturbative Serber approximation [15, 16], as well as detailed information on the pre-equilibrium particle yield [13, 17]. The investigation was extended later to describe ^{8}Be fragments. These were assumed to be produced in their ground state and thus the spectra obtained described in some sense the *entrance channel* reaction mechanism.

A comprehensive theoretical framework developed over the past 10 years in Milano (see ref. [14] and references therein) was applied to the results obtained from experiment PR 51, which was performed at iThemba LABS (formerly known as the National Accelerator Center) during March-April 2000. Various reaction mechanisms were taken into account, concentrating on one-step breakup (including a friction component) and coalescence (described below). The decay history of the nucleus is modelled by a set of coupled rate equations collectively known as the 'Boltzmann Master Equations' (BME).

The Milano approach essentially views the colliding nuclei as two Fermi gases, where the particles move in the mean field described by the N–N potential. The first part of the reaction's time evolution is the very fast perturbative breakup, after which we are generally left with an interacting fragment and a spectator. The interacting fragment may undergo complete or partial fusion with the target nucleus, and the composite which is thus formed is hence in an excited state. The excitation energy of the residual nucleus (target + participant) is calculated by considering the energy dependance of the mean field, Fermi effects, Coulomb deceleration of the projectile and the CM energy available.

The de-excitation of the residual (the decay history) is then modelled by a set of coupled rate equations collectively known as the 'Boltzmann Master Equations'. The rate equations (describing the rate of transition between discrete states of the compound residual, or probabilities of escape of certain particles) are then solved at discrete (but small) time intervals, so that intermediate particle-hole distributions can be evaluated (in both position and momentum spaces). Correlations between particle

positions and momenta may then lead to coalescence, which is the probabilistic emission of correlated nucleons. The coalescence is modelled with a Monte Carlo method, where the probability is evaluated from inverse reaction cross-sections (for the coalescence of two neutrons and two protons to form an α : $2n + 2p \longrightarrow \alpha$ for example, the inverse reaction cross-section of $\alpha \longrightarrow 2p + 2n$ is used). Peripheral interactions of fragments are described by multiple scattering in a reduced nuclear density.

The full kinematic histories of all ejectiles can thus be tracked and stored, building up a spectrum of any measurable process. This makes the model extremely flexible, allowing one to investigate new reactions, or modify existing ones, to achieve a better description of the data and thus a better understanding of the physics.

Generally good agreement has until recently been found between the experimental data and the theoretical predictions, although there were notable discrepancies. The areas where the model and the data show differences were suggestive of final-state interactions between the outgoing ^{8}Be fragment and the residual nucleus. This would be significant, especially at the lower incident energies, so it was decided to take measurements of the double-differential cross-sections of fragments which might be produced in such final-state interactions – ^{7}Be and ^{9}Be. A possible reaction channel for the lighter fragment could be neutron stripping from the outgoing ^{8}Be:

$$^{8}\mathrm{Be} \rightarrow ^{7}\mathrm{Be} + n^{0}$$

For the heavier fragment, neutron pickup is envisaged as a possible production mechanism:

$$^{8}\mathrm{Be} + n^{0} \rightarrow ^{9}\mathrm{Be}$$

If the neutron transfer mechanism were correct, it would be described in terms of DWBA. An alternative production mechanism for the two observed fragments would be the (in)elastic break-up channel. Comparisons between experimental spectra and calculated break-up cross-sections would give some information as to the validity of the perturbative Serber Approximation approach, as an alternative to the neutron-transfer channel. Herein will lie the hypothesis test of this thesis.

1.4 Outline

This thesis will be laid out in the following chapters:

Theoretical Background to the analysis of the data is given in **Chapter 2**. DWBA formalism is described but the emphasis is on the perturbative break-up mechanism. The reason for this inequality will become clear in the chapters which follow.

The Experiment is described in **Chapter 3**, where it is explained how the cross-sections were measured using the well-known $\Delta E - E$ detector telescope method. The physical setup of the detectors and scattering chamber is discussed, along with relevant aspects of the signal processing data acquisition.

Calibration of the measured spectra is an important part of the analysis and the implementation of a scintillation light output code used to calibrate the NaI detectors, among other things, is described in **Chapter 4**.

Data Analysis follows in **Chapter 5**, where the process of converting the calibrated spectra into absolute cross-sections is described (including a description of the sorting code), along with an error analysis.

Experimental results and analysis Chapter 6, where a discussion the data and its interpretation is given, along with theoretical calculations.

Finally, a summary of the **Conclusions** drawn from all the results is presented in **Chapter 7**.

Chapter 2

Theoretical Background

2.1 Introduction

Heavy nuclei are complex objects, made up of many particles, which are bound by poorly understood forces. Consequently, when two such nuclei collide, there are any number of reaction mechanisms that compete, although at a specific energy, there will be a few dominant reaction channels. With this in mind, in order to reach a significant understanding of what happens when two nuclei collide, it is necessary to obtain information on as many different reaction mechanisms as possible [18].

In the field of heavy-ion nuclear reactions at intermediate energies, there have generally been two complementary approaches to investigating the mass and momentum transfer. One approach is to direct the experiment towards light fragments, near the projectile mass, and the other is aimed at detecting the heavy fragments. These may be called the projectile residues and target residues respectively. Both techniques have been employed since the late sixties to yield important information regarding the reaction channel.

Angular and kinetic energy distributions of light nuclei generally yield an unambiguous interpretation of the experimental data, but when the outgoing particle shows a sizable mass or kinetic energy deficit, no definite conclusion can be drawn about the reaction mechanism [19]. The second type of experiment, detecting the target-

like residues, involves recoil range studies and angular distributions of recoil nuclei. This method provides information about the majority of involved nucleons, but it was initially not possible to proceed to a kinematic analysis, because simultaneous measurements of angular distributions and recoil energies for each angle were not performed. This hurdle was overcome with later experiments [12] which yielded important information on the reaction channels followed by heavy ions interacting at intermediate energies.

It was during the late seventies that the idea of a generalised critical angular momentum model was proposed to account for different reaction mechanisms such as breakup and nucleon transfer [20, 21, 25]. In this description, different reaction modes dominate at different windows of angular momentum of the projectile. During the eighties, it was becoming clear that there are several important reaction mechanisms for light heavy ions, even at energies as low as 5 MeV per nucleon. The processes may be broadly classified in terms of the degree of *momentum transfer* from the projectile to the target, creating observed projectile-like fragments (plf's) and target-like fragments (tlf's) in the first stage of the reaction.

In 1997, a comprehensive study of reaction mechanisms[1] was undertaken by Gadioli *et al.* [11] induced by ^{12}C , which used the activation technique of investigating linear momentum transfer. Previous attempts at this method used a *thick-target thick-catcher* configuration, which gave results averaged over several tens of MeV and at only a few incident energies. This method did not provide detailed information on the energy evolution of the reaction mechanisms involved, but three important classes of reactions have come to be identified :

complete fusion involving full momentum transfer and an excited compound nucleus residue,

incomplete fusion where one part of the projectile behaves essentially as a spectator, hardly interacting with the target, while the remainder fuses with the target,

[1] We will concentrate on ^{12}C-induced reactions here, though reactions induced by ^{16}O were also previously investigated

leading to a fractional transfer of momentum (essentially equal to the fraction of projectile mass that the participant carried) and

direct reactions involving the transfer of a single nucleon or cluster of nucleons, in a grazing collision, with very little momentum transfer.

The earliest attempt to describe the interaction of light heavy ions with heavy targets was made by Serber in 1947 [15]. The continuum spectra of projectile-like fragments were investigated by various authors , but was not necessarily the focus of attention. By the late seventies, there began to emerge an interest in the dynamics of the continuum bump itself [16]. Up until that stage, the cross-section had been discussed in terms of projectile fragmentation. This was described by the so-called perturbative Serber approximation by several authors [15, 4, 26]. A fairly simple expression was arrived at by Matsuoka *et al.* [16] for the double differential cross-section of breakup fragments, depending mainly on the relative momentum wavefunction of the spectator and participant inside the projectile. This approach was extended by Hussein *et al.* [10], Parker *et al.* [30], Vergani *et al.* [27] and Gadioli *et al.* [12, 13, 14].

At higher energies (above 10 MeV per nucleon), pre-equilibrium emission also becomes important [17, 28]. During the early nineties, it became apparent that to develop a good description of heavy ion dynamics, a comprehensive description of all reactions present when two nuclei collide was required.

The most general description of a direct nuclear reaction is given by the first-order **DWBA** [10]. The high energies of the unobserved fragment imply a 'transfer into the continuum' and calculations of this sort are extremely complex [29]. For any multi-step reaction, involving transfer, fragmentation, elastic scattering, *etc.*, the calculation would have to be generalised to include coupled-channels. Even then, the calculation is not in principle well defined, since the wavefunctions do not go to zero at infinity. In short, direct scattering amplitudes are in principle calculable, but we need many thousands of them for scattering into continuum states. This is beyond the scope of this thesis.

2.2 Generalised critical angular momentum model

As stated above, the different reaction channels dominate at various intervals of angular momentum. This concept of a *generalised critical angular momentum* model is not new, but was described comprehensively by Wilczńska *et al* [21]. This model sets *windows* of projectile angular momentum, where different reaction mechanisms are thought to dominate the total cross-section. There will be critical angular momenta for each reaction mechanism, from zero up to the so-called *hard-grazing* angular momentum, characterised by the distance of closest approach being equal to the sum of the half-density radii of the two colliding nuclei. It is assumed that the heaviest fragment is preferentially captured (if allowed by angular momentum limitations) and that every virtual fragment of the projectile carries a part of the total angular momentum that is proportional to its mass number. For α-particle incomplete-fusion in ^{12}C-induced reactions (with increasing angular momentum), the windows fall into categories of [21]:

$$\begin{aligned}
\text{Complete fusion :} \quad & 0 < l < l_{cf} \\
^{8}\text{Be capture - } (^{12}\text{C}, \alpha) : \quad & l_{cf} < l < \tfrac{12}{8}\, l_{cf} \\
\alpha \text{ capture - } (^{12}\text{C}, 2\alpha) : \quad & \tfrac{12}{8}\, l_{cf} < l < \tfrac{12}{4}\, l_{cf} \\
3\alpha \text{ break-up - } (^{12}\text{C}, 3\alpha) : \quad & \tfrac{12}{4}\, l_{cf} < l < l_{hg}
\end{aligned}$$

where l_{cf} and l_{hg} are the complete fusion and hard-grazing angular momenta, respectively. The values of the angular momentum windows are given by the ratios of the masses of the fragments ($\alpha - particle$, ^{8}Be, *etc* to the projectile mass).

This work shows, however, that there are other fragmentation modes apart from 3-α breakup that are important. In our case, the values for the l for the different incomplete fusion reactions involving ^{7}Be and ^{9}Be would have to be estimated from the reaction cross-section [22]. For a given angular momentum window, an expression for the cross-section of the dominant process is given by

$$\sigma_i = \frac{\pi}{k^2} \sum_{l=l_i}^{l=l_i+1} (2l+1) T_l \tag{2.1}$$

where $k^2 = \frac{2\mu E}{\hbar^2}$, $\mu = \frac{m_{\text{target}} m_{\text{proj}}}{m_{\text{target}} + m_{\text{proj}}}$ (m_{target} and m_{proj} are the target and projectile masses respectively) is the reduced mass of the colliding system and $E = E_{\text{lab}} \left(\frac{m_{\text{target}}}{m_{\text{target}} + m_{\text{proj}}} \right)$ [23].

To a good approximation, the transition coefficient $T_l \sim 1$ for $l \leq l_{\max}$ [24], so we find that

$$\sigma_i = \frac{\pi}{k^2}(l+1)^2 \tag{2.2}$$

and consequently

$$L_i = \sqrt{\frac{\sigma_i k^2}{\pi}} - 1 \tag{2.3}$$

The angular momentum window for a particular incomplete fusion reaction is thus approximately given by the reaction cross-section.

2.3 Heavy ion reaction mechanisms at intermediate energy

2.3.1 Aside: The internal structure of the projectile

There has been considerable discussion as to the existence and nature of clustering in nuclei. The question is essentially put as such : Are there preformed clusters in a given nucleus (at a particular time), or is there some probabilistic, quantum mechanical description, which would give the amplitude for the combination of nucleons into various configurations.

Some authors give certain nuclei a very large probability of clusters; it is then assumed that there exist preformed clusters within these nuclei. On the other hand, in the quantum mechanical, superposed-states view, the nucleus may contain at a certain time, a set of correlated nucleons which when asked, will tell you that they were all travelling in roughly the same way, giving the impression of a cluster. These two hypotheses have been tested, mainly using deep-inelastic scattering methods, but as far as the author can tell, there has not been a conclusive outcome to the debate. For this work, we will assume the projectile nucleus to consist of preformed α particles, which is widely accepted to be a rather accurate description. However the issue of clustering in nuclei remains a contentious one.

2.3.2 Perturbative breakup of nuclei

It was initially proposed by Serber in 1947 [15] that nuclei may break up while interacting with heavy targets. There are assumed to be preformed clusters within the ^{12}C which have a certain relative momentum[2]. The perturbation of the target field breaks the bond between the two fragments, creating a *spectator* and *participant.* The detected fragment is the spectator, while the participant may interact with the target. If the participant is absorbed by the target, then an intermediate excited composite system is formed, which decays via a number of reaction channels. There are certain dominant reaction channels at increasing time intervals. Initially, there is fast re-emission, where the ejectile (the participant) is seen to have lost only a small portion of it's initial energy. This is well described by multiple scattering in a reduced-density (peripheral) target field [13]. The next phase is pre-equilibrium emission of particles, ranging from protons to even quite heavy particles. The pre-equilibrium stage includes the 'coalescence' mechanism. After some equilibration, there is a stage of statistical nucleon evaporation, after which comes the final de-excitation by means of gamma emission to the ground state.

The main aim of this work will be to investigate the details of the first and very fast (direct) stage – breakup – which will include possible final-state interactions between the spectator and the target. Once a theoretical foundation has been laid for the interpretation of data, refinements on the model can be made. We will include various effects of increasing sophistication, including the effect of the Coulomb barrier, friction dissipative mechanisms and possible multi-step direct reactions. An attempt will be made to reconcile characteristics of the experimental data with the predictions of the model, until we are satisfied that we have described the results of the experiment, or have ruled out a particular reaction mechanism.

[2]Although this may not necessarily be the case (as detailed above), the perturbative Serber approximation is valid if one assumes that a fraction of the projectile nucleus is separated and continues essentially undisturbed

2.3.3 Development of breakup theory

In describing the breakup cross-section of a projectile, one starts by decomposing the momentum of the fragment (spectator) into a component due to the CM motion (beam) and a component due to internal motion of fragments inside the projectile. The CM component of fragments are equal (since both are moving on average with the beam velocity), while they have opposite relative momenta. It is important to keep in mind that we are describing the relative momentum of the fragments *at the time of breakup.* The cross section is then calculated in terms of the wavefunction describing the relative motion of the two fragments. If the spectator fragment momentum and mass are $\vec{P}_s$ and m_s respectively, the projectile momentum and mass are $\vec{P}_{\rm proj}$ and $m_{\rm proj}$ respectively and the participant momentum and mass are $\vec{P}_{\rm p}$ and $m_{\rm p}$ respectively, with the relative momentum of the spectator and participant being of course $\vec{p}_{\rm rel}$. Keeping in mind that in the projectile frame, $\vec{v}_{\rm spec} = -\vec{v}_{\rm part}$, one can then write :

$$\vec{p}_{\rm spec} = \frac{m_{\rm spec}}{m_{\rm proj}} \cdot \vec{P}_{\rm proj} \tag{2.4}$$

The *Serber Approximation* then states that :

$$\frac{d^2\sigma}{dEd\Omega} \propto \mid \psi(\vec{p}_{\rm rel}) \mid^2 . \tag{2.5}$$

2.3.4 Early attempts

Otherwise stated, the breakup probability amplitude is proportional to the modulus squared of the internal momentum distribution of the spectator fragment. It is thus important to find a good wavefunction that describes the relative motion of the fragments inside the projectile. This will be the Fourier transform of a good relative *position* wavefunction and that will give us the desired *momentum* wavefunction. A widely used wavefunction for the spatial separation of fragments in a nucleus is given by the Yukawa wavefunction [13]:

$$\psi(r) \propto \left(\frac{\alpha}{2\pi}\right)^{\frac{1}{2}} \frac{e^{-\alpha r}}{r}, \tag{2.6}$$

where $\alpha = \hbar\sqrt{2\mu\epsilon}$ with ϵ being the binding energy of the two fragments in the projectile and μ is the reduced mass of the two fragments. The corresponding Fourier transform is then given by :

$$\psi(\vec{p}) = \frac{1}{\sqrt{2\pi\hbar}} \int dr\, \psi(r) \cdot e^{-\frac{i}{\hbar}(\vec{p}\cdot\vec{r})}. \tag{2.7}$$

Given the above relative momentum wavefunction, Matsuoka *et al.*derived the following expression [16] for the square of the transition matrix :

$$|\,T\,|^2 \propto \frac{1}{\pi^2} \cdot \frac{\sqrt{2\mu\epsilon}}{\left[2\mu\epsilon + \left(\frac{m_s}{m_{proj}}\mathbf{P}_{\rm proj} - \mathbf{P}_s\right)^2\right]^2}. \tag{2.8}$$

One then has to multiply by the three-body phase-space factor in order to get an expression for the energy distribution of the detected spectator fragment[3]:

$$\frac{d^2\sigma}{dEd\Omega} \propto \frac{1}{\pi^2} m_s P_s \sqrt{2\mu\epsilon} \cdot \int \mathbf{P}_A d\mathbf{P}_p \delta\left(\mathbf{P}_s + \mathbf{P}_p + \mathbf{P}_A - \mathbf{P}_{\rm proj}\right) \times$$
$$\delta\left(E_{\rm s} + E_{\rm p} + E_{\rm A} - E_{\rm proj} + \epsilon\right) \cdot \left[2\mu\epsilon + \left(\frac{m_{\rm s}}{m_{\rm proj}}\mathbf{P}_{\rm proj} - \mathbf{P}_{\rm s}\right)^2\right]^{-2}. \tag{2.9}$$

A similar expression was derived using similar arguments by Parker *et al.* [30].

If the target is much heavier than the projectile, in particular $\frac{m_p}{m_{proj}}A \gg 1$, then equation (2.9) reduces to [16]:

$$\frac{d^2\sigma}{dEd\Omega} \propto \frac{4}{\pi} \cdot m_s m_p \frac{\sqrt{2\mu\epsilon} P_s P_p}{\left[2\mu\epsilon + \left(\frac{m_s}{m_p}\mathbf{P}_{\rm proj} - \mathbf{P}_s\right)^2\right]^2} \tag{2.10}$$

Although the above Yukawa wavefunction gave reasonable results for the light-particle induced breakup reactions, it was found that when it was used to describe the spectra of α particles produced in the interaction of ^{12}C on ^{59}Co, there was an unwanted high-energy tail, which did not appear in the data [13]. A wavefunction which describes the internal distribution of the fragments was used by Gadioli *et al.* [14], which is described below.

[3]Initial system consists of projectile, final system consists of residue, participant and spectator - hence 3-body phase-space factor.

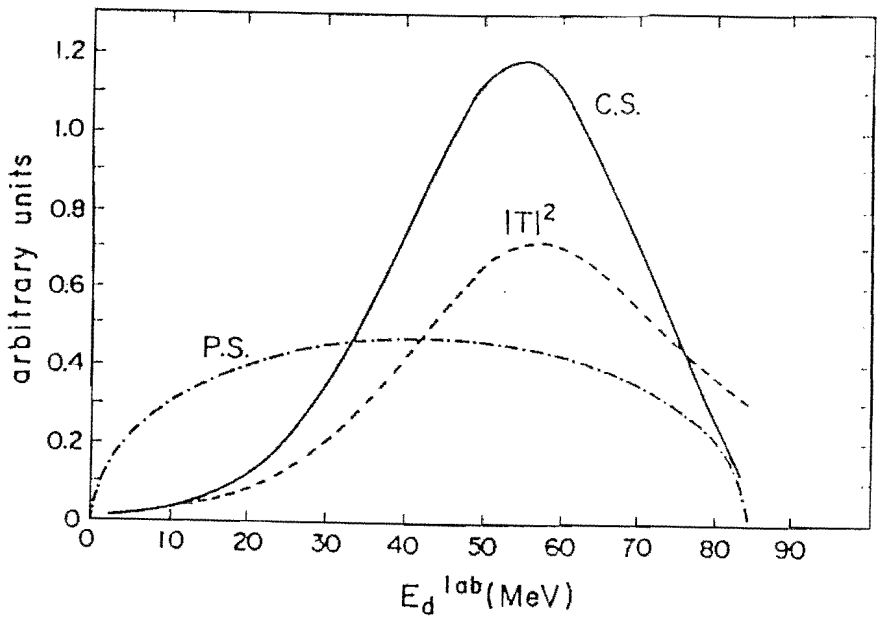

Figure 2.1: Figure showing the contributions to the total cross-section (CS) from the phase-space (PS) and $|T|^2$ factors [16]. Note that the figure shows the contributions from phasespace and $|T|^2$ factors for the particular case of ^{3}He breakup into $d^+ + n^0$. In the case of, *e.g.* $^{12}C \longrightarrow ^7$Be + ^{5}He, The factor $|T|^2$ would be much more sharply peaked and fall to zero faster. In the non-zero region of $|T|^2$, the phase-space factor is essentially constant.

2.3.5 Coulomb barrier correction

For peripheral collisions, the incoming projectile will be slowed down by the target's Coulomb field, most noticeably at low incident energies [16, 27]. To a first approximation, the energy of the projectile will decrease by the amount $E_C^{\rm proj}$ in the entrance channel and then regain $E_C^{\rm frag}$ in the exit channel, where $E_C^{\rm s}$ is the Coulomb barrier at a radius of $R = 1.4A^{\frac{1}{3}}$ fm. This can be accounted for by defining a 'local' momentum and using these as substitutes in the calculation of $\mid T \mid$. The corrected local momenta can be written as [16, 27] :

$$\mathbf{P}_{\rm proj} \longrightarrow \mathbf{P}^L_{\rm proj} = \sqrt{1 - \frac{2m_{\rm proj}E_C^{\rm proj}}{P_{\rm s}^2}} \cdot \mathbf{P}_{\rm s} \tag{2.11}$$

and

$$\mathbf{P}_{\rm s} \longrightarrow \mathbf{P}^L_{\rm s} = \sqrt{1 - \frac{2m_{\rm s}E_C^{\rm s}}{P_{\rm s}^2}} \cdot \mathbf{P}_{\rm s}\,. \tag{2.12}$$

Once these transformations have been made, the squared transition matrix can then be written as [16]:

$$|T|^2 \propto \frac{1}{\pi^2} \frac{\sqrt{2\mu\epsilon}}{\left[2\mu\epsilon + \left(\frac{m_s}{m_{\rm proj}}\sqrt{1-\frac{2m_{\rm proj}E_C^{\rm proj}}{P_{\rm proj}^2}}\cdot \mathbf{P}_{\rm proj} - \sqrt{1-\frac{2m_s E_C^s}{P_s^2}}\cdot \mathbf{P}_s\right)^2\right]^2}, \tag{2.13}$$

while a similar expression was obtained by Vergani *et al.* [27], namely

$$\frac{d^2}{dEd\Omega} \propto \frac{\sqrt{E_s E_p}}{\left[2\mu\epsilon + \frac{2m_s^2 E_{\rm proj}}{m_{\rm proj}} + 2m_s E_s - 4\left(\frac{m_s^3 E_{\rm proj} E_s}{m_{\rm proj}}\right)^{\frac{1}{2}}\cos(\theta)\right]^2}. \tag{2.14}$$

where θ is the angle between the direction of the emitted fragment and the beam velocity in the lab. frame. This expression is equivalent to that obtained by Matsuoka *et al.*in equation (2.13).

2.3.6 Refinements on the breakup model

As stated previously, when investigating the angular dependance of emitted α particles, it was found by Gadioli *et al.* [13] that the calculated cross-sections displayed a high-energy tail, which was not present in the data. They proposed to remedy the situation by using a more sophisticated wavefunction for the relative separation of the fragments. Instead of the Yukawa-type expression in (2.6), it was found that a wavefunction of the form $\psi(r) = \mathcal{R}(r)/r$, describing a square-well potential with a hard-core (of radius b) would give a better description of the data. Here,

$$\begin{aligned} \mathcal{R}(r) &= Ar^2 & 0 < r \leq b+f \\ \mathcal{R}(r) &= B\sin K(r-b) & b+f < r \leq b+R \\ \mathcal{R}(r) &= C\exp\left(-\tfrac{r}{R_0}\right) & r > b+R, \end{aligned}$$

where

$$K = \frac{\sqrt{2\mu(V_0-\epsilon)}}{\hbar}. \tag{2.15}$$

The quantities f and V_0 are free parameters, while b and R are given by

$$b = \frac{2\tan Kf - Kf}{K} \tag{2.16}$$

and

$$R = \frac{1}{K}\arctan - KR_0 \tag{2.17}$$

respectively. The constants A, B and C are matching and normalisation coefficients, which are given by [13]

$$\begin{aligned}
A &= B\frac{\sin(Kf)}{(b+f)^2} \\
B &= \frac{1}{2\sqrt{\pi}}\cdot\left[\frac{b+f}{5}\sin^2(Kf)+\frac{1}{2}(R-f)-\frac{1}{4K}(\sin(2KR)-\sin(2Kf))+\frac{R_0}{2}\right]^{-1/2} \\
C &= B\exp\left(\frac{b-R_0}{R_0}\right)\sin(KR),
\end{aligned}$$

The corresponding Fourier transform of the above wavefunction is given by [13]:

$$\begin{aligned}
\psi(\mathbf{p}) = {} & \frac{4\pi B(\hbar c)^2}{(2\pi\hbar c)^{3/2}}\cdot\frac{1}{pc}\left\{\frac{\sin(Kf)}{pc}\left[\frac{2(\hbar c)^2}{(pc)^2(b+f)^2}\left\{\cos\left(\frac{pc(b+f)}{\hbar c}\right)-1\right\}\right.\right. \\
& \left.\left.-\cos\left(\frac{pc(b+f)}{\hbar c}\right)+\frac{2\hbar c}{pc(b+f)}\cdot\sin\left(\frac{pc(b+f)}{\hbar c}\right)\right\}\right] \\
& +\frac{1}{(\hbar cK)^2-(pc)^2}\left[pc\sin(KR)\cos\left(\frac{pc(R+b)}{\hbar c}\right)-\hbar cK\cos(KR)\sin\left(\frac{pc(b+R)}{\hbar c}\right)\right. \\
& \left.-pc\sin(Kf)\cos\left(\frac{pc(b+f)}{\hbar c}\right)+\hbar cK\cos(Kf)\sin\left(\frac{pc(b+f)}{\hbar c}\right)\right] \\
& +\frac{\sin(KR)}{\left(\frac{\hbar c}{R_0}\right)^2+(pc)^2}\left[pc\cos\left(\frac{pc(R+b)}{\hbar c}\right)+\frac{\hbar c}{R_0}\sin\left(\frac{pc(R+b)}{\hbar c}\right)\right]\Bigg\}.
\end{aligned} \tag{2.18}$$

This wavefunction gives very good reproduction of the total yield of α particles and also describes the angular distribution very well [13].

2.3.7 Friction Dissipative Models

A further contribution to the breakup spectrum was proposed by, among others [5, 10], Gadioli *et al.*[14], namely a friction dissipative mechanism. It was assumed that there exists a survival probability for the incoming ion, which depends on the energy loss of the projectile due to the interaction in the target field. As a first approximation, a survival probability of $P(E_l) = 1$ was given for values of energy loss E_l below some

critical limit $E_{l,min}$. As a result, the break-up cross-section should be zero in that region. If one assumes, for simplicity, that there is constant energy loss per unit length ($dE_l/dx = 1/k$) and a constant break-up probability per unit length k' when $E_l > E_{l,min}$ then by combining these two conditions, one immediately obtains for the *survival probability* of the projectile after an energy loss E_l :

$$P(E_l) \propto \exp -kk'(E_l - E_{l,min}). \tag{2.19}$$

A further assumption was that the multiplicity spectrum $\frac{d^2N^S(E_C,E',\theta)}{dE'd\Omega}$ of breakup fragments (normalised to unity when integrated over the full energy E' and solid angle $d\Omega$), whose energy has been reduced from E_0 to $E_C = E_0 - E_l$, may still be evaluated in the perturbative Serber approximation. As the incoming projectile continues to lose energy, there comes a point where further survival is highly unlikely. Then, for the break-up spectra of the fragment emitted, one obtains the relation:

$$\frac{d^2\sigma}{dE'd\Omega}(E_0,E',\theta) = \frac{\int_0^{E_0} P(E_l)S(E_C,E',\theta)dE_l}{\int_0^{E_0} P(E_l)dE_l}, \tag{2.20}$$

where

$$\begin{aligned} P(E_l) &= 1 \quad E_l < E_{l,min} \\ P(E_l) &= \exp[-kk'(E_l - E_{l,min})] \quad E_{l,min} \le E_l \le E_0 \end{aligned} \tag{2.21}$$

and

$$\begin{aligned} S(E_C,E',\theta) &= 0 \quad E_l < E_{l,min} \\ S(E_C,E',\theta) &= \frac{d^2N^S(E_C,E',\theta)}{dE'd\Omega} \quad E_l \ge E_{l,min}. \end{aligned} \tag{2.22}$$

Note that the sharp limit $E_{l,min}$ is not physically meaningful, beside being a consequence of introducing the nuclear friction mechanism in a somewhat naïve fashion [14]. In order to justify this assumption, a more detailed model of the dissipative interaction is needed.

2.3.8 Incomplete fusion

Incomplete fusion is a process whereby a fragment is absorbed into the target, but may be re-emitted after only a few interactions. Fragments which undergo an incomplete

fusion reaction are seen to retain a large part of their original energy [11, 12], which may be explained by the fact that these processes involve low-density (peripheral) regions of the target nucleus. The fragment may be re-emitted after only a few inter-nucleon collisions, simply because it is likely to be scattered towards even more peripheral nuclear regions [13].

The predicted angular distribution of scattered fragments after a single nucleon collision is well reproduced by [62]

$$\frac{d^2\sigma}{dEd\Omega} = C\exp\left(-\frac{\theta}{\Delta\theta}\right), \tag{2.23}$$

where $\Delta\theta = \frac{2\pi}{k\Delta R}$, k is the particle wavenumber and ΔR is the thickness of the nuclear surface regions where the fragments-nucleon collisions are expected to occur. The thickness ΔR is given by $\Delta R = cA^{1/3}$ [13]. The angular distribution of the emitted fragments is evaluated by means of a Monte-Carlo method, by assuming that after each collision, equation (2.23) gives the fragment angular distribution with respect to it's direction before the collision.

2.3.9 Nucleon Transfer

The original title of experiment PR51 was "FINAL-STATE INTERACTIONS BY MEANS OF THE INCLUSIVE (^{12}C,^{7}BE) AND (^{12}C,^{7}BE) REACTIONS ON ^{93}NB AND ^{59}CO." Careful analysis of the ^{8}Be spectra at various angles of emission indicated possible evidence for the existence of final-state interaction between the outgoing ^{8}Be fragment (presumably nucleon transfer) and the residual target nucleus. As the title suggests, the experiment was aimed at detecting and calculating the double-differential cross-sections for the fragments of ^{7,9}Be that are emitted in the interaction of ^{12}C on heavy targets. It was conjectured that the heavier of the two would be produced by a neutron transfer from the target to an outgoing ^{8}Be fragment (a stripping-like reaction) and the lighter ejectile would be produced in the opposite reaction, with a neutron being captured by the target (a pickup-like reaction).

While this reaction channel is in principle possible, calculations made by our collaborators in Milano have shown that including final-state interactions do not improve

the agreement with the experimental data [31]. Thus, while mention is made of the one neutron transfer cross-section (described in terms of a DWBA formalism - see chapter 1), it is beyond the scope of this thesis to delve into a detailed theoretical discussion.

2.4 Pre-Equilibrium Emission

Pre-equilibrium emission is a process where fast particles are emitted prior to the equilibration of the compound nucleus. The yield of ejectiles from reactions induced by light ions is described by the exciton model [32], or by the Master Equation approach [17, 33].

2.5 Master Equation approach

2.5.1 Introduction

The Boltzmann Master Equation approach, initially described by Harp, Miller and Bern [33, 34], is also commonly used to evaluate the emission of pre-equilibrium particles in nuclear reactions. Although it was initially used to describe the thermalisation of excited nuclei produced in light-particle induced reactions, its use was extended to describe heavy-ion reactions by Blann *et al.* [35, 36] and the Milano group [37, 38, 40, 41, 42].

This description of the decay of highly excited nuclei starts with the excited composite system. The de-excitation is described by the set of coupled rate equations known collectively as the 'Boltzmann Master Equations'. The approach labels the particle and hole states (for neutrons and protons respectively) according to their energy ε_i and divides them into bins of energy $\Delta\varepsilon_i$. One has the number of occupied states per energy bin N_i, which is simply the total number of states in that bin g_i multiplied by the occupation probability of that state n_i:

$$N_i = g_i n_i \quad , \quad 0 \leq n_i \leq 1. \tag{2.24}$$

Once we have found the occupation of all the bins, we now allow the particles in bins i and j to interact, scattering into bins l and m respectively. There is of course also the possibility that unbound particles may escape, having an energy of $\varepsilon_i' = \varepsilon - \varepsilon_F - B_i$ where ε_F is the Fermi energy of the residual and B_i is the binding energy of the particle which was emitted.

2.5.2 De-excitation of the excited residual nucleus

The compound residual nucleus is then described as a two-component (proton and neutron) gas and its de-excitation follows from a set of coupled equations, the Boltzmann Master Equation (BME) [37, 39, 40, 42]:

$$\begin{aligned}\frac{d\left(n_i g_i\right)}{dt} &= \sum_{jlm}\left[\omega^{\pi\pi}_{lm\to ij} g_l^\pi n_l^\pi g_m^\pi n_m^\pi \left(1-n_i^\pi\right)\left(1-n_j^\pi\right) - \omega^{\pi\pi}_{ij\to lm} g_i^\pi n_i^\pi g_j^\pi n_j^\pi \left(1-n_l^\pi\right)\left(1-n_m^\pi\right)\right] \\ &+ \sum_{jlm}\left[\omega^{\pi\nu}_{lm\to ij} g_l^\pi n_l^\pi g_m^\nu n_m^\nu \left(1-n_i^\pi\right)\left(1-n_j^\nu\right) - \omega^{\pi\nu}_{ij\to lm} g_i^\pi n_i^\pi g_j^\nu n_i^\nu \left(1-n_l^\pi\right)\left(1-n_m^\nu\right)\right] \\ &- n_i^\pi g_i^\pi \omega^\pi_{i\to i'} g_{i'}^\pi \delta\left(\epsilon_i^\pi - \epsilon_F^\pi - B_i^\pi - \epsilon_{i'}^\pi - \frac{d\,D_i^\pi}{dt}\right),\end{aligned} \tag{2.25}$$

where

π, ν represent the proton and neutron respectively,

g_i are the total number of states in bin i,

$\omega_{ij\to lm}$ are the internal transition decay rates of particles between states,

$\omega_{i\to i'}$ is the decay rate for single particles into the continuum and

$\frac{dD_i}{dt}$ is a depletion term which accounts for the emission of particles (either as single particles or bound in clusters).

An analogous expression holds for neutrons.

2.5.3 Modified BME Theory

The set of equations above can be modified [43], so that the indices i, j, l, m refer to angles as well as energies. To solve these modified equations, the momentum space is divided into bins with

$$p_i^2 - \frac{\Delta p_i^2}{2} \leq p^2 < p_i^2 + \frac{\Delta p_i^2}{2} \tag{2.26}$$

and

$$p_{i,z} - \frac{\Delta p_{i,z}}{2} \leq p_z < p_{i,z} + \frac{\Delta p_{i,z}}{2} \tag{2.27}$$

where p is the momentum of the nucleon and p_z is its component along the beam axis (which is the axis of azimuthal symmetry). Given two initial nucleon momenta $\vec{p}_i$ and $\vec{p}_j$ in the CM frame of the two interacting ions, the end points of the vectors representing the two possible final momenta $\vec{p}_l$ and $\vec{p}_m$ must be diametrically opposed points on a sphere S of diameter equal to p (half the relative momentum of the two nucleons, centred around their centre of mass). An assumption is made that all points on that sphere may be reached with equal probability by the scattered nucleon momenta (which implies an isotropic distribution of scattered nucleons in their CM frame).

Once the interacting nucleons' momenta $\vec{p}_i$ and $\vec{p}_j$ are given, the decay rate (*i.e.* the decay probability per unit time) of an interaction leading one nucleon into bin l (and the other into a completely defined bin m), $\omega_{ij\to lm}$, depends on the interaction cross-section σ_{ij}, the relative velocity of the two nucleons v_{ij}, and the probability $\Pi_{ij\to lm}$. This factor is calculated as the ratio of the area Δa_l on the sphere S that was recently defined above, which may be reached by all the final momenta falling in bin l, to the total area of S, A. We thus have that [43]:

$$\omega_{ij\to lm} = \frac{\sigma_{ij} v_{ij} \Pi_{ij\to lm}}{V} = \frac{\sigma_{ij} v_{ij} \Delta a_l}{AV} \tag{2.28}$$

where V is the nuclear volume. The calculation of Δa_l, for $\Delta a_l \ll A$, is given (by considering the geometry of the situation) as a function of

- $\vec{P} = \frac{\vec{p}_i + \vec{p}_j}{2}$: sum of interacting nucleons;
- $p = \frac{|\vec{p}_i - \vec{p}_j|}{2}$: relative momentum of the two nucleons;

- p_l : momentum in the centre of bin l;
- $\theta_l = \arccos \frac{p_{l,z}}{p_l}$: the angle between the final momentum p_l and its component along the beam axis, $p_{l,z}$, and
- $\sin \alpha$, where α is the angle between $\vec{p}_l$ and $\vec{P} - \vec{p}_l$.

One finds a useful geometric relation, namely $\Delta a_l = \Delta_a \cdot \Delta_l$, where

$$\Delta_a^2 = \left[p_l^2 \left(\Delta\theta_l\right)^2 + p_l^2 \sin^2 \theta_l \left(\Delta\phi_l\right)^2\right] \tag{2.29}$$

and

$$\Delta_l = \frac{\Delta p_l}{\sin \alpha} \tag{2.30}$$

The quantities Δp_l and $\Delta\theta_l$ may be calculated from the chosen bin widths Δp_l^2 and $\Delta p_{l,z}$. The angle ϕ_l here is the azimuthal angle of the momentum vector $\vec{p}_l$, which is the possible final momentum in bin l following the interaction of the two nucleons with initial momenta $\vec{p}_i$ and $\vec{p}_j$ and is given by

$$\phi_l = \arccos \frac{\left(P^2 + p_l^2 - p^2\right) - 2Pp_l \cos\theta \cos\theta_l}{2Pp_l \sin\theta \sin\theta_l}. \tag{2.31}$$

The angle θ is given by $\theta = \arccos \frac{P_z}{P}$, where P_z is the z-component of P and $\Delta\phi_l = \frac{\partial\phi_l}{\partial\theta_l}\Delta\theta_l$.

The decay rate $\omega_{ij\to lm}$ is then finally obtained by numerically averaging over all possible values of the azimuthal angles of $\vec{p}_i$ and $\vec{p}_j$, (ϕ_i and ϕ_j). Thus, the transitions between bound states are determined.

The continuum decay rate $\omega_{i\to i'}$ is given by

$$\omega_{i\to i'} = \frac{\sigma_{\text{inv}} v_{i'}}{g_i \Omega}, \tag{2.32}$$

where σ_{inv} is the inverse cross-section of the process, $v_{i'}$ is the relative velocity of the emitted particle and the residual nucleus, and Ω is the laboratory volume. This factor cancels neatly with a similar factor in the expression for $g_{i'}$ [37].

The differential multiplicity of the particles that are emitted in time interval dt at an angle θ with energy E' is given by

$$\frac{d^2\mathcal{N}'\left(E', \theta, t\right)}{dE' d\theta dt} = R\mathcal{N}\left(\epsilon, \theta, t\right) \frac{\sigma_{\text{inv}} v'}{V'} \rho\left(E'\theta\right) \tag{2.33}$$

and the measured multiplicities are obtained by integrating 2.33 over time :

$$\frac{d^2M}{dE'd\Omega} = \int_0^{t^*} \frac{1}{2\pi \sin\theta} \frac{d^2\mathcal{N}'(E',\theta,t)}{dE'd\theta dt} dt. \tag{2.34}$$

In the above formulæ, E' is the continuum energy of the emitted particle, $\mathcal{N}(\epsilon,\theta,t)$ is the occupation probability of the states of the particle we are describing (inside the composite nucleus) and we have introduced a 'survival factor' R, which takes into account the possible dissolution of the cluster before emission [43]. The last factor in (2.33) is the density of particle states in the continuum, given by

$$\rho(E',\theta) = \frac{\sin\theta}{2}\rho(E'). \tag{2.35}$$

The value of t^* in the integral in (2.34) is the time at which the emission of high-energy particles can be assumed to be over, usually a few tens of fm/c.

For clusters with energy E_c inside the nucleus, moving in a direction θ_c with respect to the beam, the multiplicity is given by

$$\mathcal{N}(E_c,\theta_c,t) = \prod_i (n_i^\pi)^{P(E_c,\theta_c)Z_c} \cdot \prod_i (n_i^\nu)^{P_i(E_c,\theta_c)N_c}, \tag{2.36}$$

where the index i runs over all bins in which the nucleons comprising the cluster are found and $P_i(E_c,\theta_c)$ is the fraction of the bin i within the Fermi sphere of the cluster c, which has radius p_{c_F}. The cluster survival factor $R \equiv R_c$ introduced above may be explained by assuming that only clusters formed near the surface of the composite nucleus can be emitted. The value of R_c is of course smaller than unity, except for α particles, where it is assumed that since they are so tightly bound that they will survive ($R_\alpha = 1$), no matter how far from the surface they are formed [43, 70]. Finally, Z_c and N_c are the number of protons and neutrons that for cluster c.

To account for energy conservation, we write that for the cluster emitted into the continuum with energy E'_c

$$E'_c = E_c + q_c - A_c(\varepsilon_F - \varepsilon_{F_c}) \tag{2.37}$$

where $A_c = N_c + Z_c$ is the mass of the cluster, Q_c is the cluster Q-value and ε_F and ε_{F_c} are the composite nucleus and cluster Fermi energies respectively.

The last term describing the de-excitation of the nucleus in equation (2.25, the depletion term, is given by

$$\frac{dD_i^{\pi}}{dt} = \sum_c \int \int P_i\left(E_c, \theta_c\right) Z_c \frac{d^3\mathcal{N}'\left(E_c', \theta_c, t\right)}{dE_c' d\theta_c dt} dE_c d\theta_c, \tag{2.38}$$

where the summation runs over all possible clusters and the integrals are taken over all the angles and energies of clusters containing a proton (or similarly, a neutron) in bin i.

Chapter 3

The Experiment

3.1 Introduction and Aim

The aim of this experiment (named PR 51) was to measure inclusive continuum spectra using $\Delta E - E$ telescopes, with the ultimate goal of extracting double-differential cross-sections. The gains and the electronics were adjusted so as to select the ^{9}Be and ^{7}Be fragments, which we were primarily interested in, but the spectra of a few other fragments were also measured. Various aspects and considerations of the experimental procedure will be discussed in this chapter.

3.2 ^{12}C Beam energies

The main accelerator of iThemba LABS is a $k = 200$ separated sector cyclotron (SSC) for which the maximum energy possible for a $^{12}C^{+5}$ ion is about 33.3 MeV/nucleon. It was decided to have beams of 200, 300 and 400 MeV, corresponding to 16.6 MeV, 25 MeV and 33.3 MeV/nucleon respectively. These energies, apart from being convenient to produce, were far enough apart to show subtle effects which should still be described by the same physics [44].

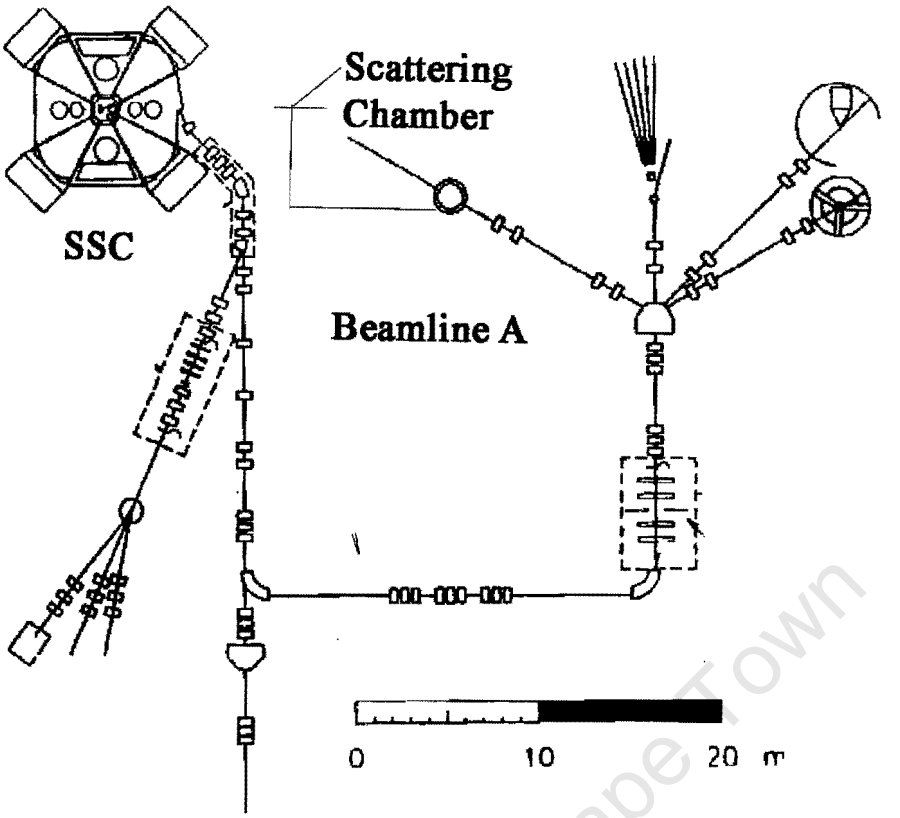

Figure 3.1: Schematic diagram of the beamlines and experimental vaults in use at iThemba LABS. The label 'SSC' designates the separated sector cyclotron accelerator and our scattering chamber is located on beamline A.

3.3 The scattering chamber

One of the experimental facilities at iThemba LABS is the 1.5 m diameter scattering chamber. It is situated on beam line A of the iThemba LABS and can house various hardware necessary for the detection of particles and the transport of the electronic signals to the data-acquisition room. Figure 3.1 shows the large-scale setup of beam lines and experimental vaults at iThemba LABS.

The scattering chamber is made up of a cylinder-shaped chamber, in which the targets, detector arms and the detectors themselves were housed. The targets are held on a vertical ladder, one above the other. Different targets are inserted into the path

of the beam by selecting the vertical position of the target ladder, so that the selected target is centred on the beam. The vertical height of the target ladder, which can be determined to an accuracy of ~ 0.25 mm, is selected from a control panel in the data room. It is also possible to rotate the target ladder about its vertical axis, to select a target angle relative to the beam's direction. This angle can be selected with an accuracy of 0.1°.

The rotatable detector arms are at slightly different heights above the floor of the chamber, hence one refers to the upper- and lower arms. The angular positions of the detectors can be controlled with an accuracy of up to 0.1°, which is also done from a control panel in the data room.

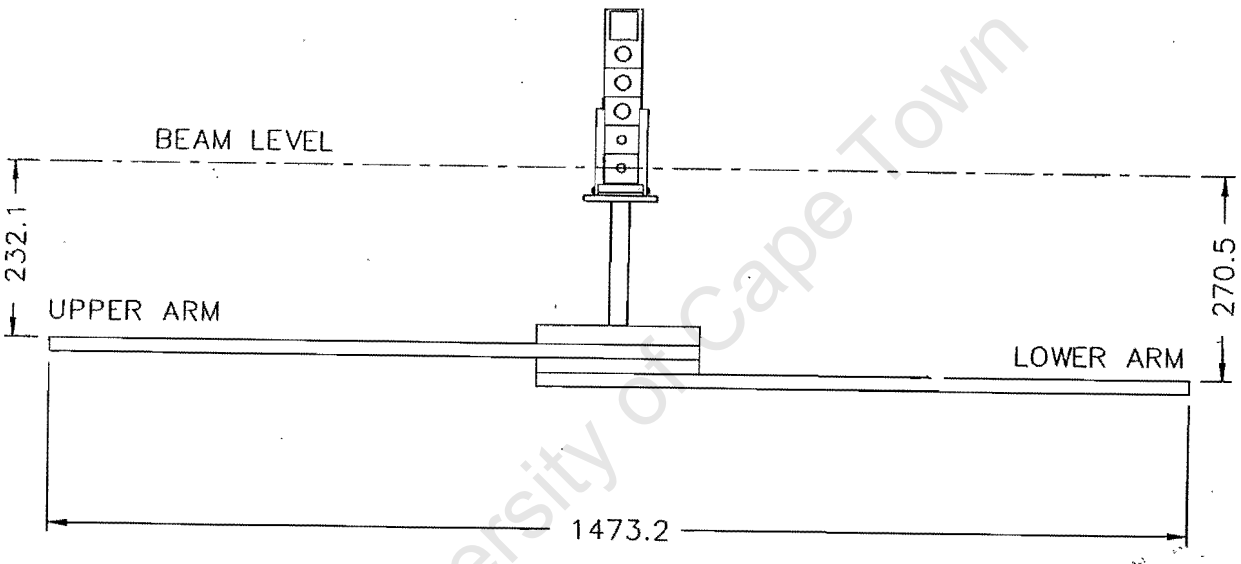

Figure 3.2: A scale diagram showing the target ladder and rotatable detector arms. All dimensions are in mm. The alignment with the incoming beam is shown.

The wall of the chamber contains ten ports for various purposes. There are the two main ports, diametrically opposed, which delineate the beam direction; one of them houses the incoming beam line and the port opposite continues to the beamdump a few meters further on. Just above the beam entrance port is a perspex window to which a CCTV camera is attached. The purpose of this camera is to observe the scintillation of the beam spot on a ruby crystal (Al_2O_3), which gives visual assistance in the tuning

and focusing of the beam from the control room. Another port of the chamber is connected to a hand valve for venting the chamber with air or Nitrogen. There are six outlets for the feedthroughs for high voltage and signal cables coming from the pre-amps, which in this experiment were mounted together with the detectors inside the chamber. There is a patch panel near the scattering chamber, which is attached via BNC co-axial cables and high-voltage cables to a corresponding patch panel in the data room. During the experiment, the scattering chamber was kept at a vacuum pressure of $10^{-4} - 10^{-5}$ mbar.

Electronic signals produced by the detectors were subject to noise, as always. To reduce signal deterioration during the journey from the vault to the data room, the chamber had to be properly earthed. A cross-sectional view of the scattering chamber is given in figure 3.3.

3.4 Targets

A variety of self-supporting thin targets were used in the beam tuning, calibration procedures and in the experiment proper. For data-taking, a ^{93}Nb target with a thickness of $1.7205 \cdot 10^{-3}$ g/cm was used. A mid-mass target ($A \sim 100$) was chosen to suit the physics that we wished to observe : a target which was too light would not allow sufficient nucleon interactions to justify a statistical model such as BMET, and a very heavy target would be vulnerable to undergoing fission.

As mentioned above, to assist in the beam tuning procedure, a scintillating ruby crystal with a 3 mm diameter aperture in its centre was used. This generally allowed the technicians constrain the beam to a spot not much bigger than 3 mm in diameter (although the beam was not always this good), by giving a visual indicator (monitored by the CCTV camera attached to the chamber port) of where the beam spot occurred.

The beam could not always be confined to a perfect spot, producing what is known as 'beam halo'. The presence of beam halo is to some extent inherent in all charged particle beams and had to be monitored as it poses a potentially significant source of error.

The measurement of the beam halo was done in the following manner : an empty frame was placed in the beam path, with the detectors set to forward angles (8°). The counts detected with the empty frame - counts(empty) - were compared to the counts with a target in place - counts(target), giving an estimate of the beam halo. The ratio $\left(\frac{\text{counts(empty)}}{\text{counts(target)}}\right)$ was kept below 10 % for both detector telescopes (at 8° for both T1 and T2) during the experiment. Due to the nature of halo production (small angle scattering of the beam off the beampipe, beam-gas interactions, defocussed projectiles, etc.), as the angle increases, the halo measured with the empty frame dramatically decreases.

For the purposes of the beam angle offset measurement, a ^{12}C foil target was used. The elastic scattering peak was observed on both sides of the beam line and from the scattering angles giving equal count rates, the beam offset was deduced. Although the beam offset was different each time the beam was tuned, it never exceeded 0.5° and was corrected for by adding the offset to the detector angle for each arm.

3.5 Detector telescopes

Each detector telescope was made up of two principal components: a Si surface barrier ΔE detector and a NaI(Tl) E detector. Our choice of NaI(Tl) crystal as the stopping E detector was based on its acceptable efficiency and resolution in the required energy region, and their availability at the time. The telescopes were fixed to the movable arms by means of aluminium mounts inside the scattering chamber.

3.5.1 Silicon ΔE detectors

Since good energy resolution was needed over the full allowed kinematic range of the fragments, it was decided to have two different thicknesses of Si ΔE detectors. Both were EG&G Ortec semiconductor radiation detectors. The lower arm (T2) had a thickness of 24.4 μm and the upper arm (T1) had a thickness of 58.0 μm. The two different thicknesses of Si detectors yielded a good separation of the two Be loci over

the full energy range. The experimental vault was cooled to 14° C by means of an air conditioning system, in order to reduce thermal noise levels in the detectors.

3.5.2 NaI(Tl) detectors

The energy resolution requirements of our experiment were such that we needed to separate the spectra of ^{7}Be and ^{9}Be, which was adequately met by the NaI(Tl) crystals. The 12.7 mm thickness of the NaI(Tl) crystal was set by the consideration that we were aiming to stop the highest energy Be fragments from a 400 MeV ^{12}C beam. The problem of the energy calibration of the NaI(Tl) stopping detectors was an interesting one, since the scintillation response of these detectors to the ions of interest is nonlinear. An in-depth discussion of how it was achieved is presented in chapter 4.

3.5.3 Physical Setup

An important issue in the physical setup of the detectors was their adequate shielding from low-energy electrons and extraneous electro-magnetic fields. It was also important to have a well-focused beam, to reduce the uncertainty in the detector solid angle. These factors, along with other considerations (such as the alignment of the detectors with the beam axis) were taken into account when it came to the physical arrangement of the detectors inside the scattering chamber.

The shielding of the detector consisted of a tantalum passive collimator and metal shielding of the NaI(Tl) crystal and PM tube. The Si surface barrier detectors were preceded by a thin 7 μm thick Kapton shield, which stopped low energy electrons from entering the detector, but had negligible effect on the ^{12}C heavy ejectiles that we measured. Since the thick NaI(Tl) stopping detectors are hygroscopic, they were encased in light- and air-tight metal shieldings, with HAVAR windows at the entrance.

Care had to be taken to account for possible gain-drifts of the photomultiplier tubes. This was done by monitoring the light output of a pulsed LED embedded in the detector crystal. The pulser appeared in the spectra and it's peak centroid position was monitored at regular intervals; refer to chapter 3 for a full discussion. A cross-sectional

view of the physical setup of the detector telescopes is given in figure 3.4. The centres of all of the components were aligned with respect to the centre of the target foil.

The solid angle subtended by the detector at its distance from the target centre was 1.023 msr, and depended on the collimator. Because of the geometrical arrangement inside the scattering chamber, there were limitations of the minimum scattering angle and detector separation angle. We could not reach scattering angles smaller than 8° because at that angle, the collimator began to intercept the beam and we would create a shower of secondary particles as the high-energy ^{12}C ions scattered off of the collimator mounting. The minimum detector separation angle that could be reached was 26°; when the detectors came closer to each other than this, they would touch, and this would destroy our accurate alignment.

To keep electronic dead-time to a minimum, it was necessary to keep the count rates below a certain value. The count rates depended on the beam current and the detector solid angle. The beam currents were typically kept at about 10-11 nA for the small separation angles, and were increased when the detectors were at larger angles, to about 17-20 nA. We had to take care to minimise the effects of radiation damage, as it would increase the leakage current and decrease the energy resolution. As a result the count rates were monitored and, by adjusting the beam current, were kept to below 1.5×10^3 s^{-1}.

3.6 Electronics

The electronic setup converted electric (in the case of the Si-ΔE detectors) and light (in the case of the Si(Tl)-E detectors) pulses produced by particles in the detectors, into amplified electronic signals which could be processed by a computer once they had been digitised by an ADC. The electronic setup for the processing of the signals was kept the same throughout the experiment.

3.6.1 Detector Signals

In this experiment, we were dealing with two types of electronic signals, namely *linear* and *logic* signals.

Linear signals

These gave the information on the measured energy of the incident particle that was detected. The output signals were fed to pre-amps, which shaped and amplified the signal before being sent to the patch-panel in the experimental vault. From there, the linear signals were sent via the 93 Ω signal cables to a similar patch panel in the data room. The impedance of the signal cables was chosen to match the impedance of the NIM modules. Once the linear signals were taken from the preamplifier, and sent to the data room, they were processed by the NIM modules in the following way :

The linear signals were taken from the pre-amps of the NaI(Tl) (E) and Si (ΔE) detectors, (referred to as elements $\langle$A$\rangle$ and $\langle$B$\rangle$ respectively) and were fed into the patch panel. At the other end of the data cables in the data room, the signals were taken from the corresponding patch panel and processed by passing them through a series of modules. The raw signals were passed through a amplifier and a delay amplifier before being passed into a linear gate and stretcher (LGS). The signals were finally processed by an analog to digital converter (ADC) and transported via the CAMAC crate to the data aquisition computer.

A symbolic flow chart of the processing of the linear signals for one telescope is shown in figure 3.5. Signals from events of interest or pulser events were selected by using certain logical requirements, which were provided by timing conditions, and sent to the respective scalers and the pattern register module.

Logic Signals

One condition on the positive identification of a particle was that we have a time coincidence of events in elements $\langle$A$\rangle$ and $\langle$B$\rangle$. To do this, we needed fixed-shape signals carrying either the logical value 1 or 0, generated by a constant fraction discriminator

(CFD). If a particle was detected in element ⟨A⟩, the logical signal from the CFD would be sent to a coincidence module as a **START** signal, after a certain delay. The delay was necessary, since solid-state detector produces a fast signal, compared to the slow process time of the electronics; care had to be taken to ensure that the signals arrived at the correct time. If the signal from element ⟨B⟩ arrived before the **STOP** signal (set by the gate), then the coincidence requirement would be satisfied and an event would be registered.

If another event arrived while the electronics were engaged in processing the previous one, they would be insensitive to the presence of that event; in effect the electronics would be *'dead'*. This is the well-known effect of dead time and had to be corrected for. A signal was generated for every event that the CAMAC crate was busy processing, the '**BUSY**' signal. This was fanned out to veto the logical operations, blocking the coincidence unit and the inhibited scalers. Details of the dead time correction are given in chapter 5.

3.6.2 Current Integrator

A parameter of interest was the total amount of accumulated charge, which was necessary to calculate the absolute cross-section (described in chapter 5). This was recorded by a module called the current integrator. The number of output pulses from the current integrator was integrated to give the total charge collected.

3.6.3 Pulsers

The pulsers were fired at a rate proportional to the beam current and had two purposes:

- they were used to determine the gain drifts in the NaI(Tl) detectors
- and they were used to calculate the dead time during experimental runs, which will be discussed in the next subsection.

Both of the above aspects of the experiment were corrected for during the data analysis (see chapter 5) . The pulser signals were triggered using the digital output signals from

the current integrator, which was fed via a timing single channel analyser (TSCA) to a prescaler. This gave prescaled signals at a rate proportional to the beam current i to the LED pulser module for the NaI detectors, which fired both LEDs simultaneously.

3.6.4 Scalers

Two scaler modules counted the number of telescope events, including the pulser events. The input of one of the scalers was inhibited by the computer **BUSY** signal, described above in section 3.6. An independent, continuously running timer was linked to a TCSA and served as an 'electronic clock'. A scaler was linked to the output of this electronic clock, (denoted as 'uninhibited', since it was continuously running). Another scaler (denoted as 'inhibited' since it was stopped during dead time *i.e.*, connected to the output of the computer**BUSY** signal) served as a 'computer clock'. The ratio of the inhibited scalers to the uninhibited, gives one the dead time.

3.7 Data Acquisition

Once the analog electronic signal had arrived at the ADC, it was converted into digital data and processed as a set of data '*words*' into an '*event*'.

The event was transported to the data acquisition computer where the data acquisition program (**XSYS**) was used to write the data to disk via a CAMAC crate. **XSYS** was also used as an online interface for viewing the data. The data acquisition process was automatically controlled by the computer, once the **XSYS** *BEGIN* command had been entered.

The data that had been acquired was written to a hard disk in the form of data words, containing the pulse-height information of the ΔE and E signals. These raw data words had to be sorted, which involved the application of the energy calibration to the particle, putting them into the correct histograms, *etc.* and thus building up a particle identification (PID) spectrum. Part of the event structure was the pattern register word, which would tell the sorting code whether the event was a pulser event

or a non-pulser ('physics') event.

3.8 Data Sorting

For each energy, and each pair of detector angles we had chosen, a run of data was saved as an event file. This was just raw data in the form of events (as described above), which needed to be processed by means of the so-called **EV**ent **A**nalysis **L**anguage, **EVAL**. The data stored were then replayed offline from disk using this code to obtain corrected counts per bin spectra. A FORTRAN code described in chapter 5, `SIGMA`, was written to calculate the absolute double differential cross-sections from these spectra.

3.8.1 EVAL code

It was necessary to set up the necessary data areas needed in the experiment, such as the 1- and 2-D histograms and various variables and constants, such as the calibration constants. These data areas would then be incremented accordingly as the data were sorted. Events were immediately sorted into two types : pulser events and non-pulser ('physics') events.

As stated before, this was the job of the **EVAL** file. It contained various subroutines for the identification of particles, their energy calibrations and the determination of the dead-layer corrections needed. The dead layer correction and energy calibration subroutines were an implementation of the procedures explained in chapters 3 and 4 respectively. A more in-depth discussion of the **EVAL** code, it's constituent subroutines and their respective functions will be given in chapter 4.

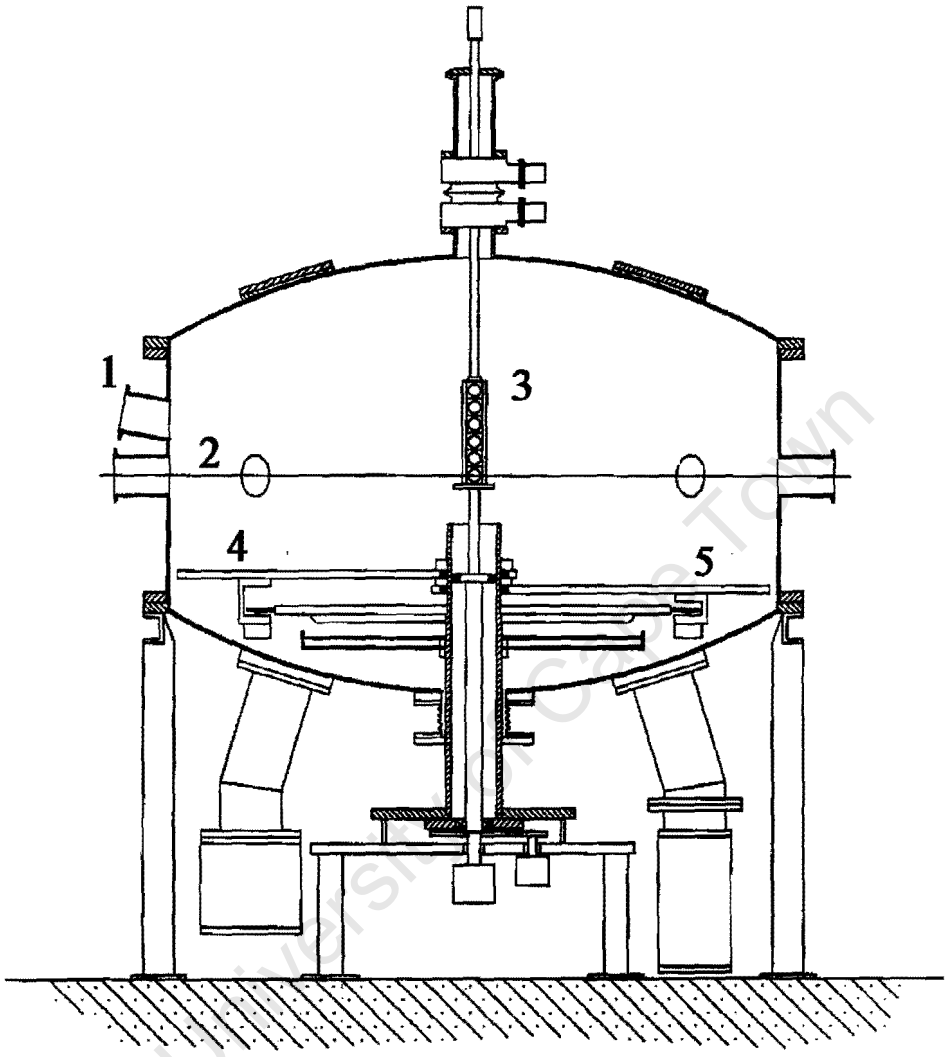

Figure 3.3: A cross-sectional view of the experimental scattering chamber with the CCTV camera port (1) above the beam entry port (2) on the left, showing target ladder (3) and detector telescope arms (4,5).

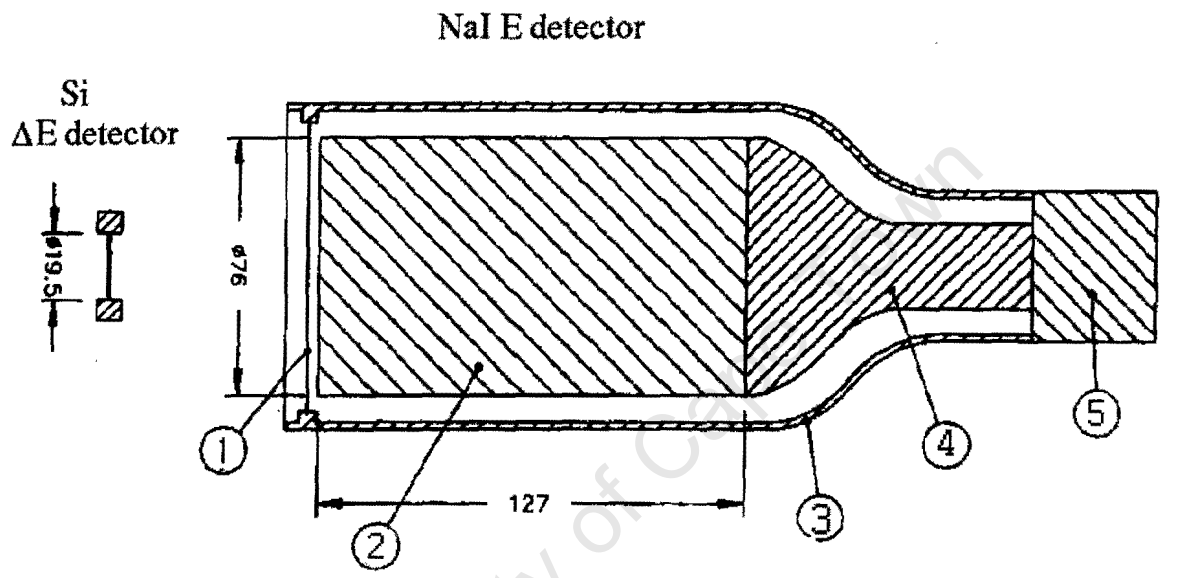

Figure 3.4: A cross-sectional view of the NaI E and Si ΔE detector telescopes. Shown are: Si-ΔE detector (left), 7μm thick HAVAR entrance window (1), NaI(Tl) scintillator crystal (2), metal shielding (3), photomultiplier tube (4) and base (5). All dimensions are given in mm.

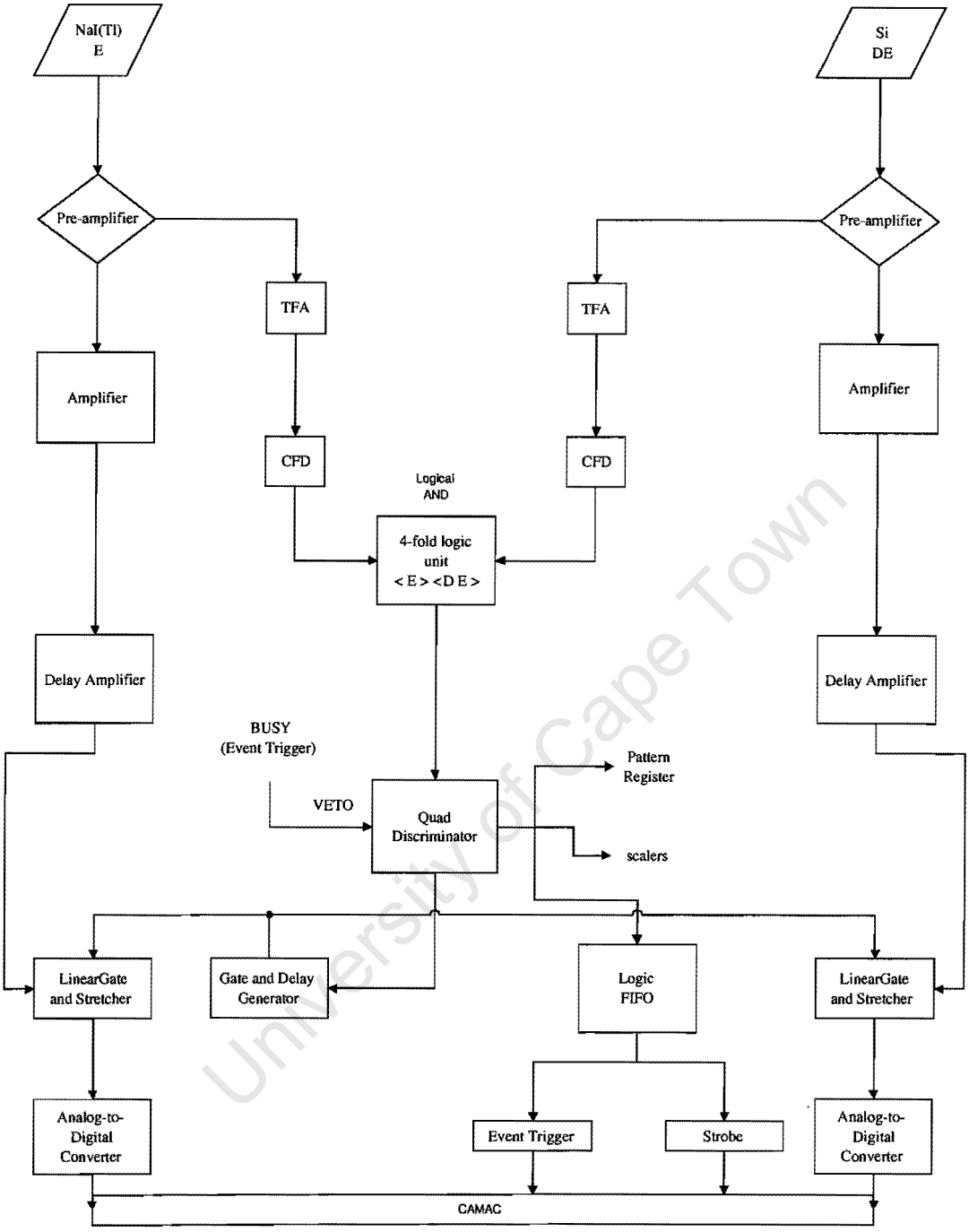

Figure 3.5: Schematic representation of the electronic modules used in the experiment, for one telescope.

Chapter 4

Calibration of the stopping detectors

4.1 Introduction

In order to rigorously calibrate a detector in an experiment such as this, it is essential that the response of the detector to the ejectile ions to be measured is well known. One usually measures the response function by having incident beams of the desired particles at known energies and then measuring the signal (light) output of the detector at various energies. For the stopping E detectors, this is usually done by measuring the elastic scattering peak cross-section at various angles and comparing the results with the corresponding two-body kinematics prediction for elastic scattering. In our case, this was not possible. Apart from the fact that the absolute response functions are not known in the intermediate energy range for the ions in which we were most interested, ^{7}Be and ^{9}Be, it was not feasible to produce beams of these ions. In short, we were forced to find another way to calibrate our NaI detectors.

In this chapter, we will show that there was a need for a very good energy calibration. A discussion of the theory of electron energy deposition that helped us to solve the problem and the implementation of a scintillation light-output model will be discussed. Particular emphasis will be placed on the implementation of the model and

the choice of parameters that we used.

4.2 Need for a rigorous calibration

A rough calibration was done (to first order)by fitting specific energy-loss curves ΔE *vs* E to the experimental data. These were calculated using a code named `KINMAT`, which predicted the specific energy loss for each ion, given the experimental details of the detector, such as the energy loss per unit length of a particular ion, the total thickness of the detector, *etc.* This method would lead to uncertainties of about 20 %, which was reasonable for a preliminary discussion of the data, but unsatisfactory for a detailed comparison with calculations. The reason for this was that the particle identification spectra (PID) spectra were not so well defined as to permit the unambiguous determination of the parameters that described the curves for each ion. Figure 4.1 shows the

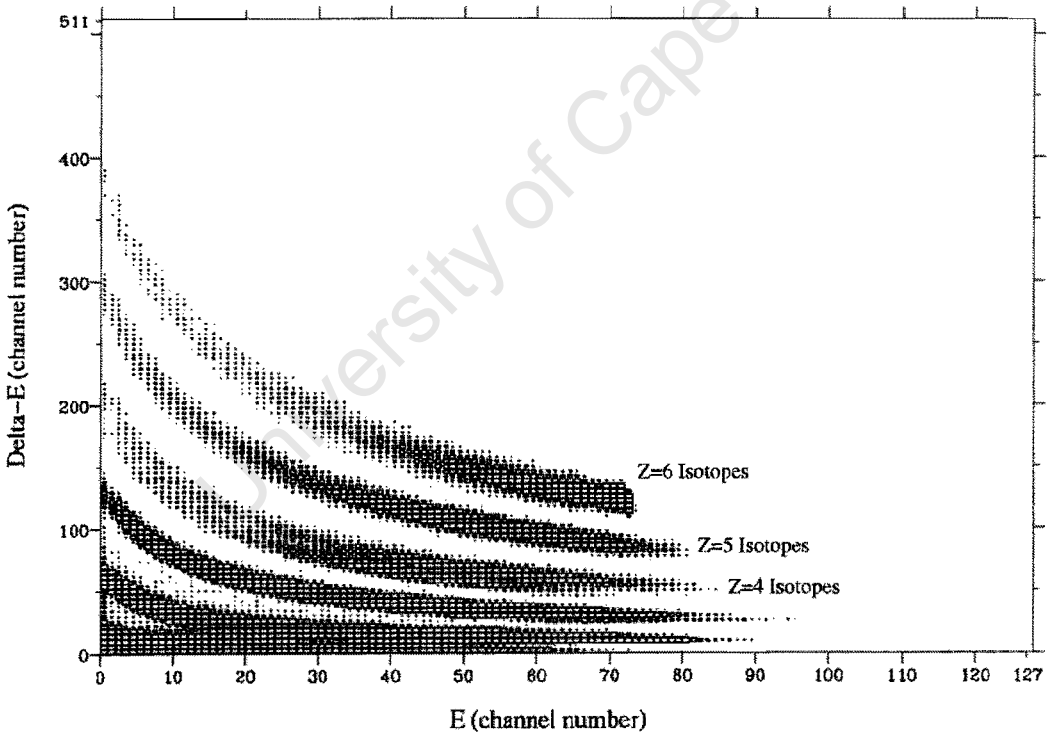

Figure 4.1: A sample PID spectrum showing the broadening of the kinematic loci. Note that it is impossible to separate the ^{7}Be and ^{9}Be loci within the Z=4 locus.

ambiguity of parameter selection due to the size of particle loci.

To overcome this, we decided to use a light output model of scintillator detectors based on a theory of energy deposition from secondary electrons. Although very sophisticated models exist for the calculation of the electron energy deposition and response of scintillators [50, 51], it was decided to follow a method developed by Michaelian *et al.* [48, 49]. The reasons for this decision are described below.

A phenomenological model of detector response [52] was developed previously, which gave similar results to those obtained by Michaelian. In that case, however, the mass-dependance of the response was not taken into account, whereas in this study, it was attempted to incorporate it in a consistent manner. The model describes the response of inorganic detectors (such as CsI, or in our case NaI(Tl)) as well as organic scintillators (such as plastic or liquid scintillator). A discussion of the model and our implementation thereof will follow.

4.3 Theoretical light output model

4.3.1 Introduction

While phenomenological models of the luminescence response of scintillators have existed since the early 1950's [45, 46, 47], experimenters using organic and inorganic scintillators usually ignored them, relying instead on an arbitrary n-parameter fit to experimental data in order to calibrate their detectors. This was principally due to the complexity of existing secondary electron energy deposition models, which made implementation of such models impractical, but also due to the fact that these models had not been shown to unambiguously describe the data over a wide range of incident charges and energies[49]

A phenomenological model of detector response [52] was developed previously, which gave similar results to those obtained by Michaelian. In that case, however, the mass-dependance of the response was not taken into account, whereas in this study, it was attempted to incorporate it in a consistent manner. The model describes the

response of inorganic detectors (such as CsI, or in our case NaI(Tl)) as well as organic scintillators (such as plastic or liquid scintillator). A discussion of the model and our implementation thereof will follow.

4.3.2 Secondary electron production and specific luminescence

If one is to understand the scintillation response of secondary electrons produced by the heavy ions, then an understanding of the interaction of charged particles with matter is essential. The energy loss per unit length of charged particles traversing matter is usually described by the Bethe-Bloch equation[1], which gives the energy loss of a particle moving through matter as a function of it's mass A, charge Z and velocity β [53]:

The light output for all scintillation detectors shows a strong (non-linear) dependance on the properties of the incident ion - *e.g.* the incident energy E, the charge Z and, to a lesser extent, the mass A. As stated above, the simplest way to calibrate a detector is to produce beams of the required ions, but one could also model the light output, relying on knowledge of the underlying physical processes at work. This kind of model would give us the *relative* light output of various ions. An absolute calibration is then obtained by normalising the relative light output curves, using the absolute responses of the detector to ions for which we *had* taken measurements. In our case, these known data were for ^{12}C and ^{4}He.

The basis of this model is the assumption that the scintillation light-output produced by energetic ions is related to the energy distribution of the secondary electrons produced along the ion's track. The initial momentum transfer from the ion to the electron is computed in the so-called *impulse approximation*, where it is assumed that the interaction takes place over a time which is small compared to the characteristic period of revolution of the electron in it's orbital. In this approximation, which is good at intermediate energies and still better as the incident energy increases, the secondary electron is constrained to be scattered along a path perpendicular to the track of the

[1] See section 5.3 for a detailed expression

ion. Once one knows the initial momentum, and specific energy loss of the electrons[2], calculated using Lindhart's [54] potential theory, one can calculate the total energy deposited by the electron until it is stopped in the detector.

Modelling the relationship between the light output and the electron energy deposition, one can predict the scintillation response of the detector, for a given ion with a given incident energy, by integrating the energy deposition of secondary electrons over the ion's path until it is finally stopped in the detector. To a first approximation, the light output dL per unit length dx is directly proportional to the energy carrier density dN_e [60]:

$$\frac{dL}{dx} \propto \frac{dN_e}{dx}. \tag{4.1}$$

Here, the energy carriers are either secondary electrons or holes. The local production of electron-hole pairs is assumed to be proportional to the local energy deposition density $\rho(r)$ deposited by the ion, where r is the radial distance from the ion's track. $\frac{dL}{dx}$ in equation (4.1) is also called the *specific luminescence*.

4.3.3 Prompt quenching effects

Equation (4.1) is not quite accurate however, since one has to take into account quenching effects [60], which are introduced into the model by assuming that there is a maximum energy density ρ_q above which prompt quenching predominates. Prompt quenching can be understood in terms of competition between electron capture at the so-called luminescence centres (mainly the Tl^+ activator sites in the NaI crystal) and non-radiative recombinations of electron-hole pairs. The quenching density ρ_q is an inherent property of the scintillating material and is a constant for a given detector.

There is a distance r_q perpendicular to the track (the so-called *quenching radius* of the ion), where the deposited energy density falls below the quenching density. If the energy density as a function of radial distance from the ion's track, $\rho(r)$ is known, one can solve for the quenching radius by setting $\rho(r_q) = \rho_q$.

[2]Specific energy loss is the energy loss per unit length - dE/dx - of the electrons

4.3.4 Energy carrier density

Before one can calculate the energy carrier density dN_e/dx, one needs to find an expression for the energy deposited by the incident ion, as a function of the radial distance from its track–$\rho(r)$. Taking into account the electron energy loss and contributions from backscattered electrons, one has a general expression for the energy deposition density [49]

$$\rho(r) = N\frac{e^4}{(n \cdot m_e)} \cdot \frac{(z^*)^2}{V^2} \cdot \frac{1}{r^2} \cdot \left[1 - \frac{r}{R_{max}}\right]^{d+1/n}, \tag{4.2}$$

where N is the number density of electrons in the material which is given by:

$$N = N_A \cdot \frac{Z_{eff}}{A_{eff}}\varrho. \tag{4.3}$$

Here, N_A is Avogadro's number, ϱ is the average density of the material and Z_{eff} and A_{eff} are the effective charge and mass of the material respectively. The effective charge z^* of the incident ion is less than the nominal charge of the ion, especially at lower energies, because of electron pickup. An expression for the effective charge is given by Montenegro *et al.* [55]. V is the velocity of the ion, $R_{\max}$ is the maximum electron range, which is dependant on the initial momentum transfer from the ion to the electron, or equivalently the impact parameter of the two interacting particles. The constant n features in the range-energy relation of the secondary electrons and has been found by Kanaya and Okayama [56] to be best described by 5/3; d depends on the charge of the incident ion as $d = 0.045\, Z_{\text{eff}}$.

Once the quenching radius and prompt quenched energy density have been determined, the specific quenched energy carrier density is given by:

$$\frac{dN_e}{dx} = K \cdot \left[\pi r_q^2 \rho_q + \int_{r_q}^{R_{max}} 2\pi r \rho(r) dr\right]. \tag{4.4}$$

Here, the integration is performed over a cylinder concentric with the path of the ion, with the radius being measured perpendicularly outwards. The constant K in (4.4) relates the number of energy carriers produced to the energy deposition.

One now needs to integrate (4.4) at each point along the ion's trajectory to obtain the number density of energy carriers, which the reader will recall is related to the light

output (see equation (4.1)). It has been found [49] that this can be done analytically if the exponent $d + 1/n$ in (4.2) is a rational number. If we now define $\mathcal{D}$ and $\mathcal{R}$ as

$$\mathcal{D} = \frac{6}{5}\pi K \cdot N \cdot \frac{e^4}{m_e} \cdot \frac{(z^*)^2}{V^2} \tag{4.5}$$

and

$$\mathcal{R} = 1 - \frac{r}{R_{\max}} \tag{4.6}$$

respectively, one obtains for our specific case of NaI(Tl) [49] :

$$\frac{dN_e}{dx} = \mathcal{D}\left[-\ln(1-\mathcal{R})\right]. \tag{4.7}$$

This now gives us a relation for the specific energy carrier density in terms of the energy deposition density. We can use relation (4.7) to calculate the light output per unit length and integrate along the trajectory of the detected ion until it is stopped in the scintillator material. Before we can continue, however, we need a better understanding of the energy transport mechanism from the creation of the energy carriers to the actual light emission.

4.3.5 Energy transport to luminescence centres

The light production in the crystal is related to the process of energy transport *via* the thermal diffusion of the energy carriers, from the point where they were created to the activator (Tl^+) sites. Prompt quenching leaves a number $\frac{dN_e}{dx}$ unquenched electron-hole pairs. The electrons are quickly trapped at the Tl^+ sites and the holes are trapped in the NaI lattice. These two energy carriers types then decay from their trapped states with an exponential lifetime. The decay constants are of the order of a nanosecond and are roughly equal for the electrons and holes [60].

There is a competition between two types of electron-hole recombination, namely radiative recombination and non-radiative recombination. As one might expect, radiative recombinations are so-named since they are recombinations of the type where visible light is emitted; non-radiative recombinations are conversely the type where no light is given off or where light is emitted in the UV part of the spectrum. Since the

Tl in the NaI lattice makes the crystal very opaque to ultra-violet radiation, if light is emitted in this frequency range, it is quickly absorbed and only partially re-emitted in the visible range, which has the effect of contributing to the non-radiative emissions, since we cannot detect a fraction of it.

To take account of the fact that we may over-estimate the light production if we do not include non-radiative recombinations, we assume that the number of recombinations at Tl sites is proportional to the density of Tl activators in the crystal, ρ_a. Next, we assume that the number of non-radiative recombinations is proportional to the number of holes left after prompt quenching, which is proportional to the number density of quenched energy carriers $\frac{dN_e}{dx}$. The observable light emitted per unit path length of the ion is then given by:

$$\frac{dL}{dx} = C\frac{dN_e}{dx}\left[1 - \mathcal{F}\left(\frac{\frac{dN_e}{dx}}{\epsilon\rho_a + \frac{dN_e}{dx}}\right)\right], \tag{4.8}$$

where C is an overall normalisation constant (chosen to scale the scintillation curves to reproduce the experimental data), ϵ is a constant relating the cross-section for capture at a Tl site to the cross-section for electron–hole annihilation and $\mathcal{F}$ is the fraction of recombinations which produce no light, or which produce UV light which is not re-emitted in the visible range. A detailed description of the calculation of $\mathcal{F}$ was done recently by the INDRA collaboration, for CsI(Tl) detectors [50], although for our purposes, we may treat it as a free parameter.

Since the Tl activator sites make the crystal so opaque to UV light, the constants ϵ, $\mathcal{F}$ and ρ_a are true constants of the material and only need be determined once, since they don't depend on the incident particle at all. These constants are obtained by varying them one at a time and comparing, as before with ρ_q, the model-predicted light output to the experimentally obtained values for a particular ion.

4.4 Implementation of the light output model

4.4.1 Choice of parameters

The stage was now set to implement the theoretical light output model, but first it was necessary to determine the parameters that described our detector - the quenching density ρ_q, the non-radiative coefficient $\epsilon\rho_a$ and the overall absorption constant, $\mathcal{F}$. During the experiment, we had taken calibration runs using a ^{12}C beam and a ^{4}He beam, and these points were used in the analysis. A FORTRAN code [57] (LE4) asked for the input calibration points and choice of parameters, and then plotted the predicted light output for the ions for which we had experimental data, as well as their normalisation constants. The normalisation in this case was with respect to the experimental data points.

The fit was described by two factors: the χ^2 of the fit and the fractional deviation of the normalisation constants for the two ions, $\frac{\Delta C}{\overline{C}}$. Here C is the normalisation introduced in equation (4.8) and ΔC is the deviation of this normalisation coefficient obtained for each ion from the average, $\overline{C}$, *i.e.* $\Delta C = \left|C_{\text{ion}} - \overline{C}\right|$. The best fit of the model to the data, and thus the best set of parameters, would be the one where these two factors were near to their minima. In the case of a minimum in $\frac{\Delta C}{\overline{C}}$, this would mean that all ions would have nearly the same normalisation coefficient, which is desirable in that the model becomes projectile-independent to some extent.

It was decided to begin with a choice of parameters which had been quoted in the literature, for NaI(Tl) [58], *i.e.*

$$\rho_q = 2.3 \cdot 10^6 \text{ erg/g} \;\; ; \;\; \epsilon\rho_a = 9.0 \cdot 10^{-4} \; \% \;\; ; \;\; \mathcal{F} = 0.4 \tag{4.9}$$

It was found immediately that changing the value of $\mathcal{F}$ did not improve anything, so it was decided to fix that parameter to it's initial value of 0.4 and vary the other two one at a time. Upon doing this, two sets of parameters were obtained that provided a minimum χ^2 sum, namely:

First Set		Second Set	
ρ_q (erg/g)	$\epsilon\rho_a$ (%)	ρ_q (erg/g)	$\epsilon\rho_a$ (%)
$2.3 \cdot 10^6$	$6.4 \cdot 10^{-4}$	$1.2 \cdot 10^6$	$9.0 \cdot 10^{-4}$

Both of these sets gave very small fractional deviation from the average normalisation constant ($\frac{\Delta C}{C} < 0.05\%$) and plots of the predicted light output for these two sets look almost identical. Figure (4.2) shows the predicted light output curves for ^{4}He (upper curve) and ^{12}C (lower curve), compared to experimental data obtained at NAC. The

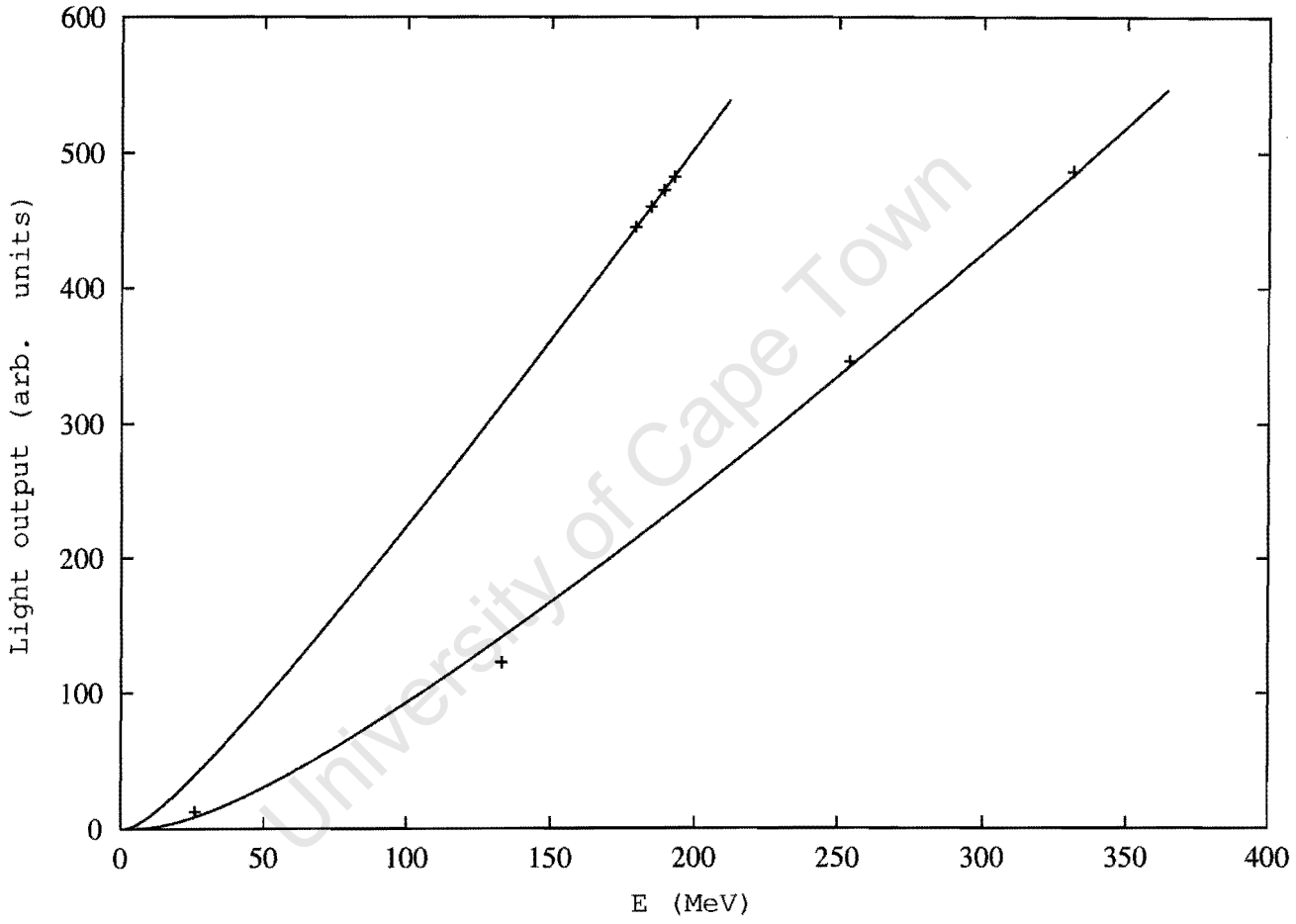

Figure 4.2: Predicted light output curves for the choice of parameters : $\mathcal{F}= 4$; $\rho_q = 2.3 \cdot 10^6$ erg/g and $\epsilon\rho_a = 6.4 \cdot 10^{-4}$ %, along with the calibration points obtained from ^{12}C and ^{4}He elastic scattering data. Note that the calibration points have errorbars which are smaller than the plotting symbols.

former set of parameters was favoured, since this value of ρ_q gave the best fit to previous

data for NaI [49] and there were indications that the value of $\epsilon\rho_a$ was dependant on the concentration of Tl activators in the crystal. This would be unique to our detectors, but the value of ρ_q depends only on the properties of the NaI lattice and should be independent of the detector. Figure 4.3 shows the model predicted energy calibration for all the ions of interest, as a function of normalised light output, or equivalently, channel number.

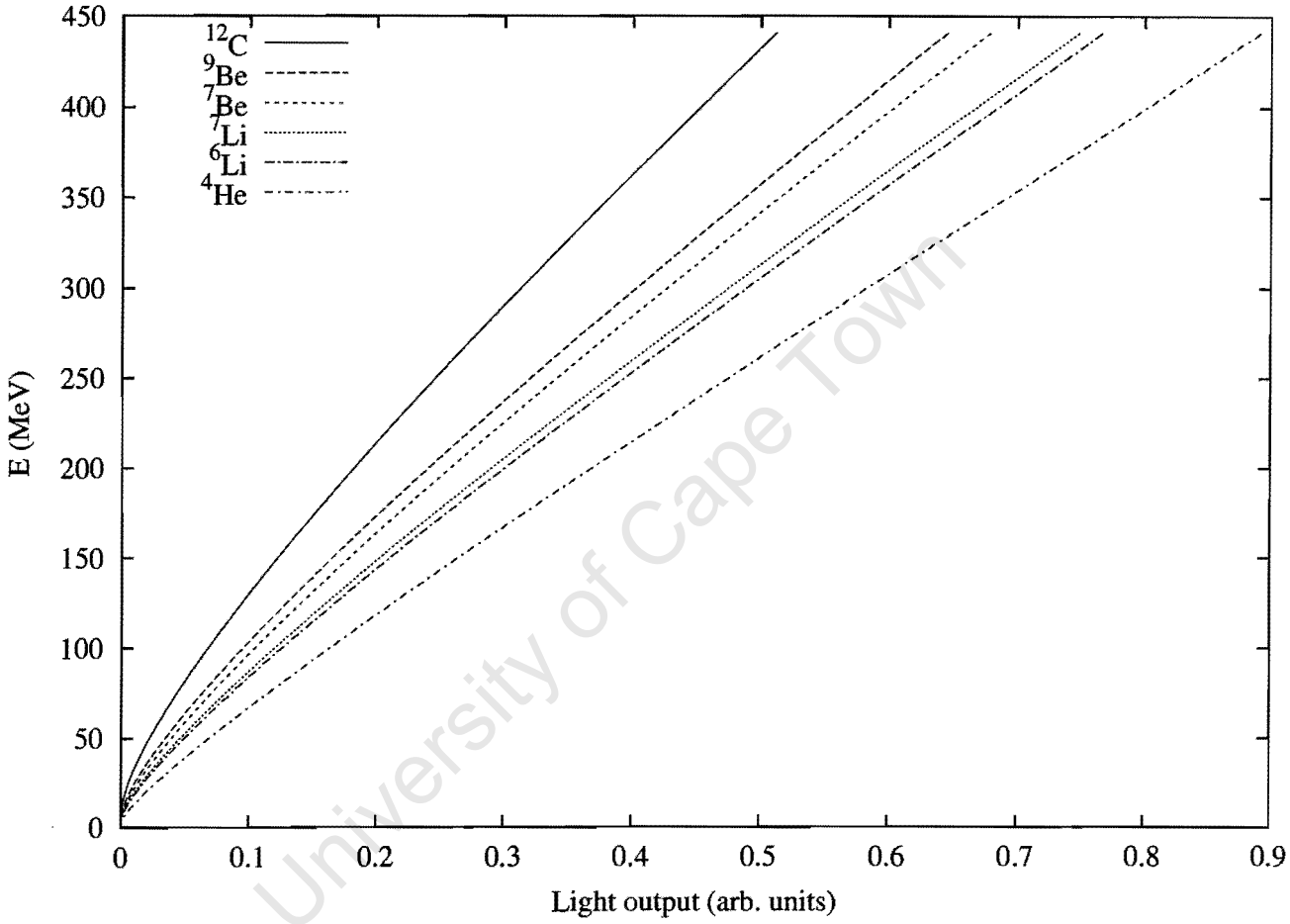

Figure 4.3: Model predicted energy calibration as a function of light output (channel number). Shown here are curves for ^{4}He, ^{6}Li, ^{7}Li, ^{7}Be, ^{9}Be and ^{12}C. Note the separation for the Be curves.

4.4.2 Parameter Sensitivity Test

Introduction

Having found a parameter set that models the calibration data points we have for ^{4}He and ^{12}C, we would like to know if our choice is a wise one. It may be that there is another set of parameters ($\varepsilon\rho_a$ and ρ_q) that also describe the calibration points well (giving a low χ^2 and $\frac{\Delta C}{C}$), but give a different prediction for the ions that we are actually interested in: ^{7}Be and ^{9}Be. Since we had no compelling physical argument for choosing one such set of parameters over any other, it would be encouraging to observe that the predicted curves $E(L)$ (for which the parameters $\varepsilon\rho_a$ and ρ_q gave a good fit to the experimental calibration data) of the Be isotopes (indeed of *all* of the detected ions) are similar. If this were to be the case, we would not have to justify our choice of parameters, since all sets would give the same result.

A way to show this is to vary $\varepsilon\rho_a$ and ρ_q and in doing so, record sets of these parameters that give a good fit. As stated above, a good fit to the experimental data is described by a low variation in normalisation constants C between various ions. A FORTRAN code `BRUTO` was written which, for a selection of fixed ρ_q values steadily decreased $\varepsilon\rho_a$, calling the light output code `LE4` as a subroutine and calculated $\frac{\Delta C}{C}$ and the average normalisation constant for all ions, $\overline{C}$. For each set, `BRUTO` checked whether $\frac{\Delta C}{C}$ fell below some tolerance, say 0.05 % and if so, recorded the values of $\varepsilon\rho_a$, ρ_q and $\overline{C}$. We would thus obtain a large (more than 100) number of sets of parameters that gave good fits, which we could use to generate respective light-output curves for ^{7}Be and ^{9}Be.

Relative Deviation at Constant Energy

Since it is difficult to compare entire curves to each other, it was decided to compare the different light-output curves produced by each set of parameters at 2 constant energies. The light output of ^{7}Be and ^{9}Be at these energies would then be normalised to that of ^{12}C at the same energy. Constructing two new sets of parameters, $\xi^7_{1,2}$ and $\xi^9_{1,2}$ defined as:

$$\xi_i^{7,9} = \left. \frac{L_{^{7,9}\mathrm{Be}}(E_i)}{L_{^{12}\mathrm{C}}(E_i)} \right|_{E_i} \tag{4.10}$$

we can investigate the relative deviation of the predicted light output curve at constant energy. Here the energy cuts E_i were free to be chosen; since the most nonlinearity is at low energy, we chose the energies E_i to be 50 and 100 MeV respectively.

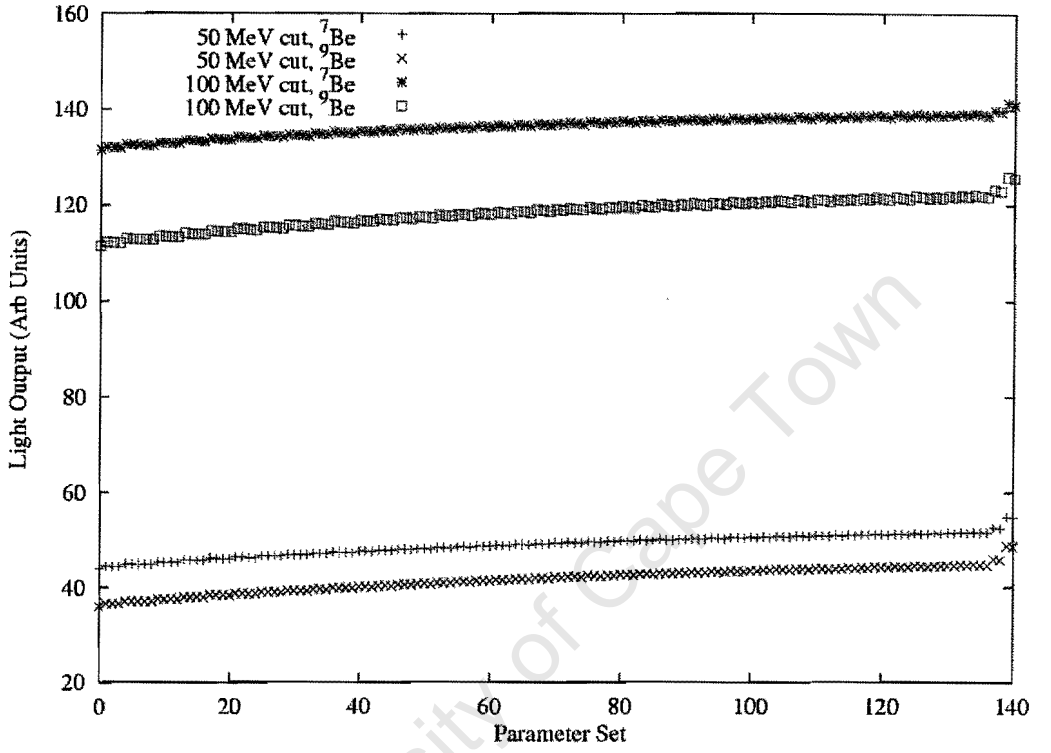

Figure 4.4: Plots of the model-predicted relative light output of the ions ^{7}Be and ^{9}Be, at constant incident energies of 50 MeV and 100 MeV . The horizontal axis refers to the particular set of parameters ρ_q and $\varepsilon\rho_a$ used in the model, which gave a good fit to the experimental data - see the section 4.4.2 for an explanation. Note that even though the value of ρ_q spans an order of magnitude, the relative light intensity is rather stable at constant energy.

Figure 4.4 shows that even though the value of ρ_q spans an order of magnitude and more than 130 sets (the horizontal axis of the figure) of parameters were found that gave a good fit, the relative deviation of the predicted light output is remarkably constant at a fixed energy, *i.e.* the values of ξ_i^7 and ξ_i^9 are constant for all practical

purposes. There is seen to be a deviation when ρ_q becomes too large, so it is not possible to choose *any* value, but if one is in a reasonably realistic range, then the model prediction is rather insensitive to the actual set of parameters that one chooses

4.4.3 Parameterisation of the predicted light output calibration curve

We had now found a good set of parameters to describe our detector when implementing the theoretical light output model. It was now necessary to include this calibration in our sorting code (EVAL file). We could proceed in one of two directions : we could write a subroutine into the sorting code which would perform the entire light output calculation for each detected particle, or we could parameterize the predicted light output curve which we had obtained. The former operation, apart from taking up a large amount of CPU time whilst sorting and thus slowing down the data-analysis procedure, would present a fairly large and unnecessary computational task. On the other hand, parameterization of the light output curve is comparatively simple, given the vast library of built-in functions that most commercial mathematical software packages contain. A decision was thus taken in favour of the latter procedure.

The primary parameter which described our detector was the normalization constant $\mathcal{C}$. This was needed to scale the predicted light output curves in order to satisfactorily reproduce the experimental data used for calibration (*i.e.* the ^{4}He and ^{12}C data). This factor was determined by the fitting procedure, concurrently with the other primary parameters, ρ_q and $\epsilon\rho_a$. It was found that this constant was best described by $\mathcal{C} = 1775.7$ for both detector telescopes T1 and T2.

The first choice of the function to parameterize the light output was arbitrarily chosen to be a power series, with a square-root of the form

$$E(L) = a + bL + cL^2 + d\sqrt{L}, \tag{4.11}$$

where E is the energy of the detected particle and L is the corresponding light output. The coefficients a, b and d were found for this choice of function to be of the order

of unity, whereas the value of c was much smaller by comparison, $\sim 10^{-5}$. For this reason, and since we do not expect there to be a detected light pulse if there is no particle ($E(0) \equiv 0$) the values of a and c were forced to zero. As seen from fig 4.5, even with this function, there was excellent agreement between the predicted data points given by the implementation of the scintillation model, and the parameterisation. Our

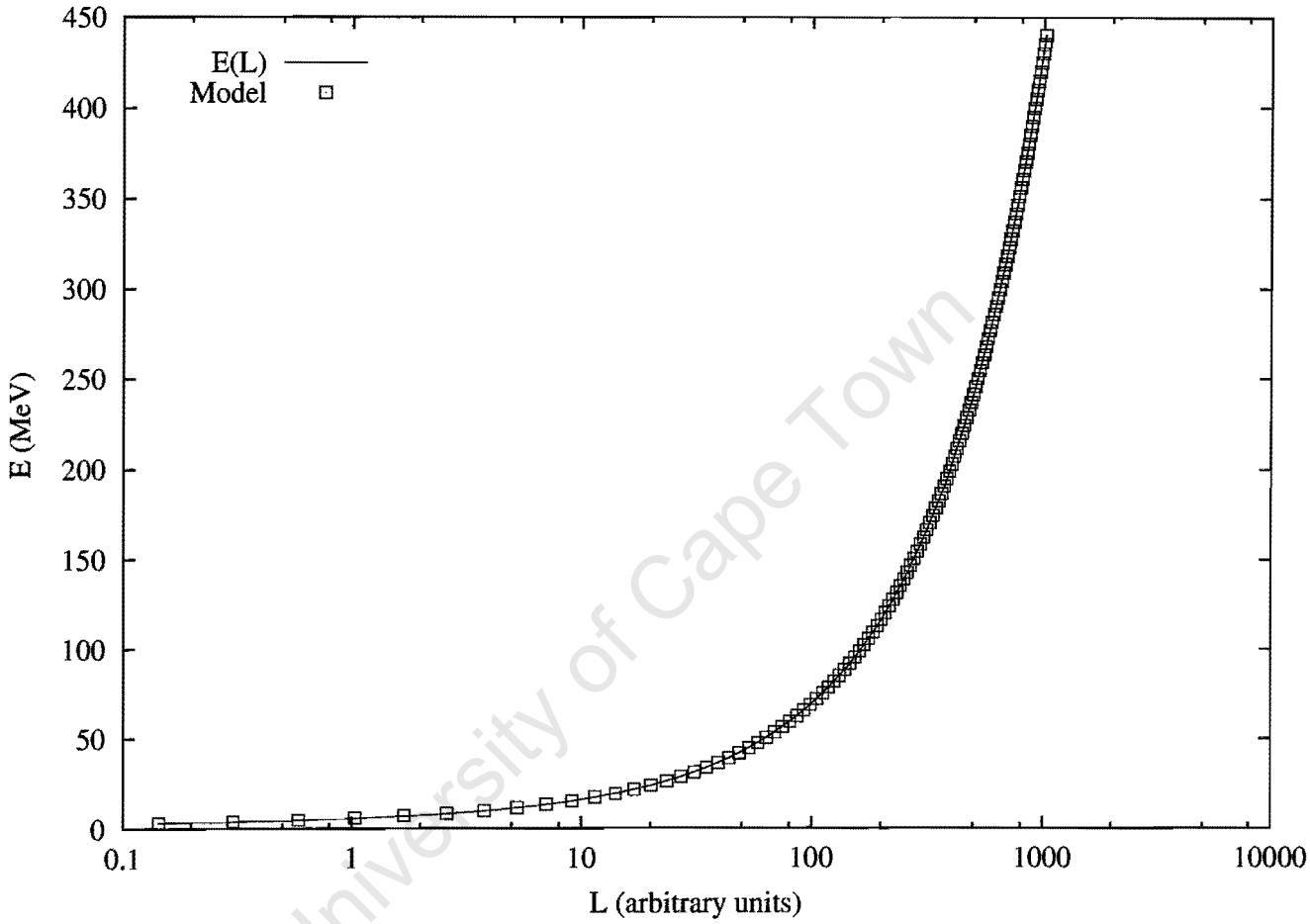

Figure 4.5: Comparison of model-predicted ^{7}Be (400 MeV incident energy) calibration and first-approximation power series. Note the excellent agreement even at low energies.

modified light output parameterisation thus took the form of

$$E(L) = c_1 L + c_2 \sqrt{L}. \tag{4.12}$$

The least-squares fit of this general parameterisation showed that there was a mass and charge dependance of the constants c_1 and c_2. Upon further investigation, it

was found that while there was seen to a dependance of c_1 solely on the charge of the detected particle, the coefficient c_2 varied with mass as well as charge. This is shown in table 4.1 and figure 4.6.

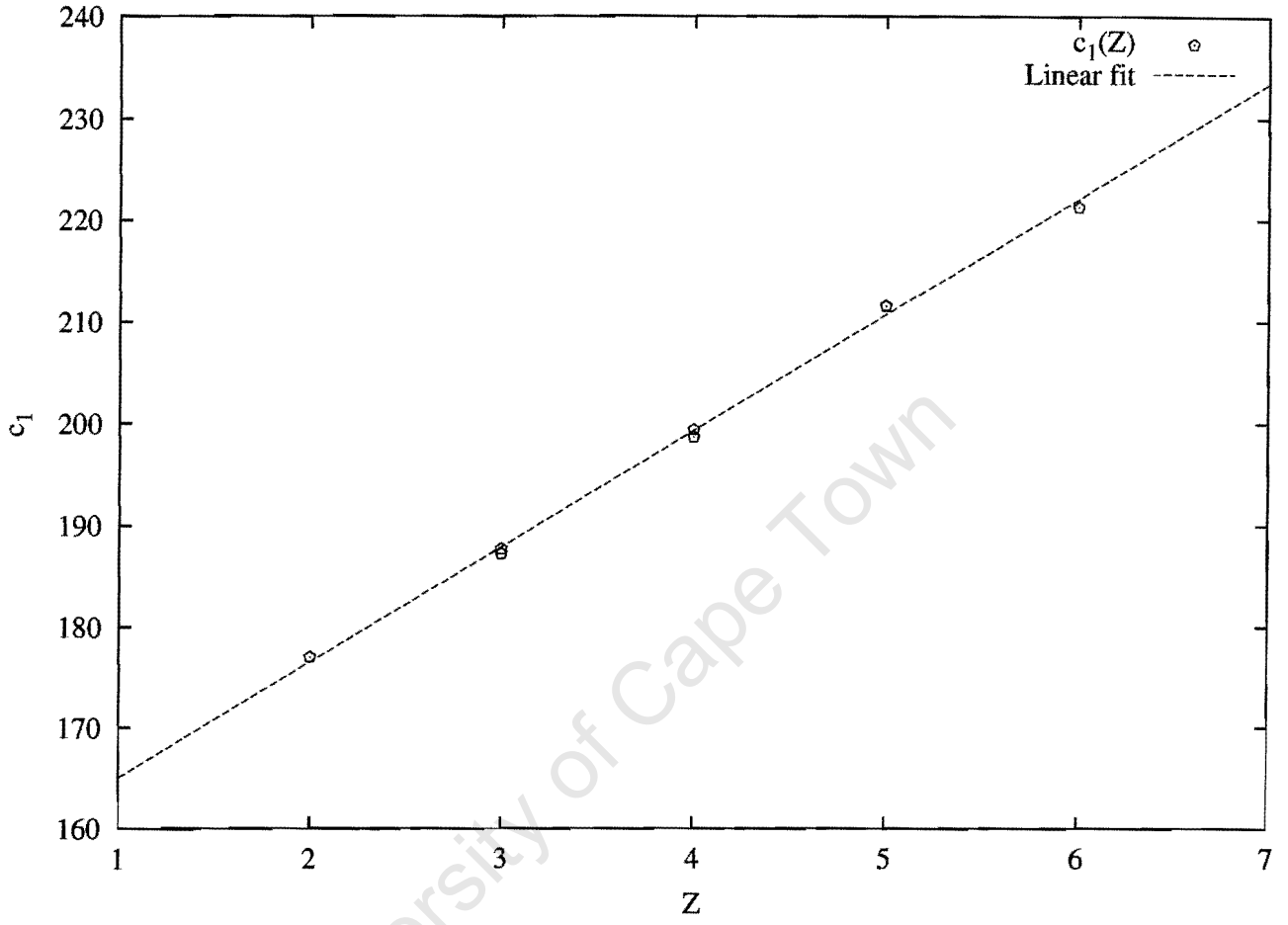

Figure 4.6: The coefficient c_1 used in the parametrisation, as a function of ion charge. As can be seen from the proximity of the points at $Z = 3$ and $Z = 4$, the coefficient c_1 shows very little mass dependance, and is well-described by a straight line of the form $c_1(Z) = 153.669 + 11.410Z$.

On the other hand, it is interesting to note that the non-linear term of the calibration curve ($\sqrt{L}$) has a coefficient that is dependant on both the mass A and the charge Z. Since there was no apparent reason to choose any specific form of the combination of A and Z, dependance of the form AZ was assumed and then fitted, since it was the simplest combination. Upon inspection of the variation of the coefficient c_2 with AZ,

Ion	Charge	Mass	c_1	c_2
^{4}He	2	4	176.977	55.807
^{6}Li	3	6	187.228	86.442
^{7}Li	3	7	187.719	92.900
^{7}Be	4	7	198.670	108.063
^{9}Be	4	9	199.382	121.977
^{10}B	5	10	211.608	171.777
^{11}B	5	11	211.556	148.732
^{12}C	6	12	221.327	168.142

Table 4.1: Table of values found for the parameters c_1 and c_2 appearing in the calibration function $E(L) = c_1 L + c_2\sqrt{L}$. Note the difference in dependance of c_1 and c_2.

it was found that the function

$$\ln g(AZ) = 2.93 - 1.173 \cdot 10^{-5} \cdot (AZ)^2 + 0.52 \cdot \ln(AZ). \tag{4.13}$$

smoothly fits the points rather well, as is seen from figure 4.7. This was thus chosen as the functional form of $c_2(A, Z)$. We now had fully parameterised the relationship between the detector response of a particle detected by our detectors, and the energy of that particle. Of course, it has to be kept in mind that this parameterisation may only be valid for our mass and charge range and that if one wants to use this method for a significantly heavier beam, or detected fragments, then the issue should be approached entirely afresh.

To code this parameterization, a FORTRAN subroutine (ENERGY) was written which was called by the EVAL sorting code for each detected particle event (see chapter 2).

Thus, we had successfully and rigorously calibrated our experiment by implementing a model of the luminescence production of ions based on a theory of secondary electron production, determining all of the parameters which described our detectors. A large amount of uncertainty was done away with, since all the parameters in the model are known to less than 1 %.

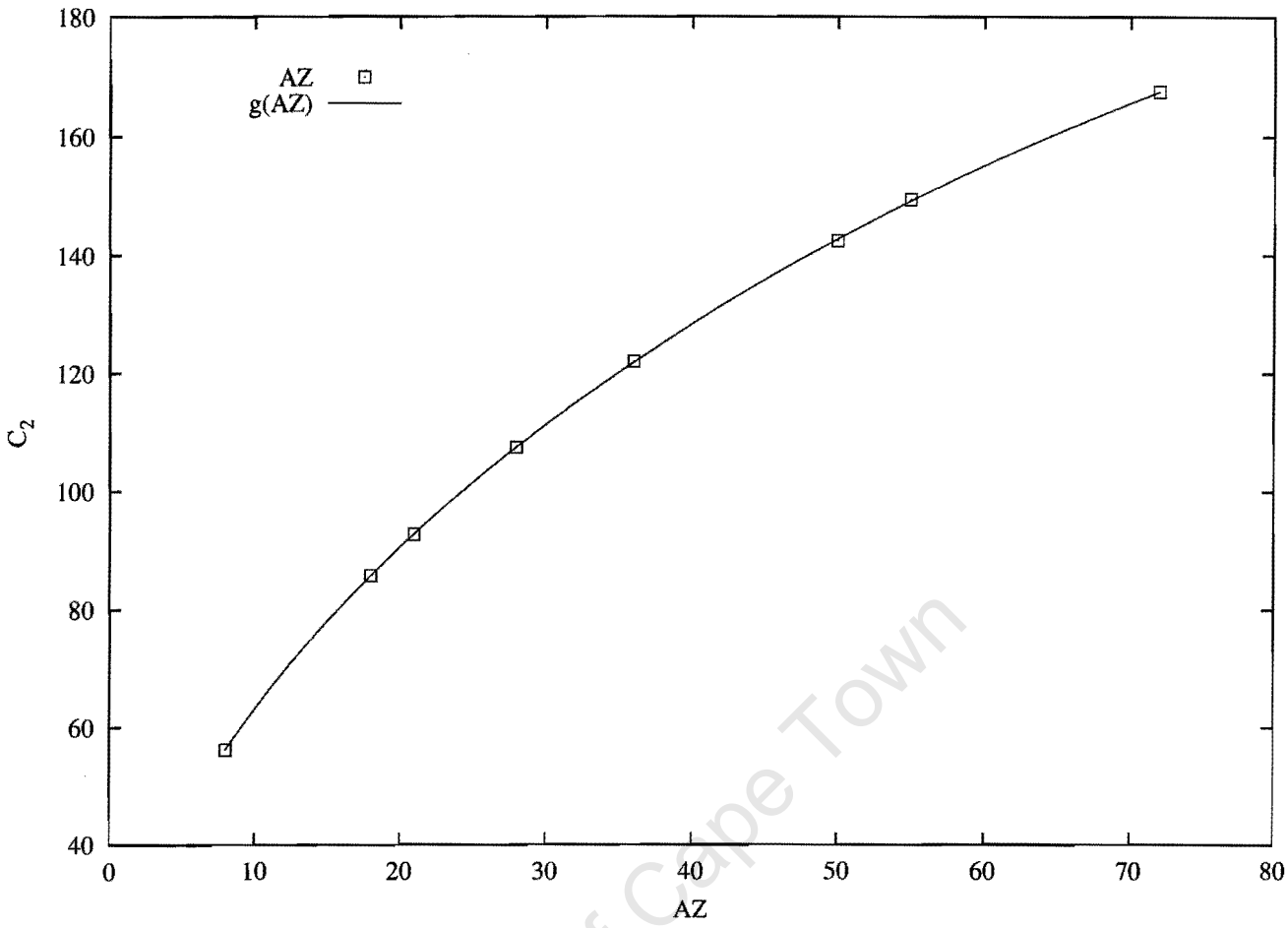

Figure 4.7: The coefficient c_2 as a function of the variable AZ. It is seen that there is a smooth interpolation of the constant c_2 in the parameterised light output curve, described by equation 4.13. Note that this parameterisation may only be valid for our mass and charge range, *i.e.* $4 \leq A \leq 12$ and $3 \leq Z \leq 6$.

Chapter 5

Data Analysis

5.1 Overview

This chapter will deal with the procedure which was followed during the offline replay of data runs and software used in extracting differential cross-sections from the data which we had taken. A summary of the calibration is given.

5.2 Calibration of the detectors

5.2.1 Si-ΔE detectors

The response of Si detectors is close to linear with the incident particle energy. In order to calibrate our Si detectors, we used a ^{228}Th source, which is a long-lived α emitter. By fitting a linear function to the points that we obtained from this source, we were able to calibrate the Si detectors.

5.2.2 NaI(Tl)E detectors

The calibration of the stopping NaI(Tl) detectors was a more complicated procedure than that of the Si-ΔE detectors, which implemented a model of the relative light output of energetic ions, normalised with experimental data for ^{12}C and ^{4}He. The

implementation of this model is fully described in chapter 4.

5.3 Replay of the data files

5.3.1 Particle Identification

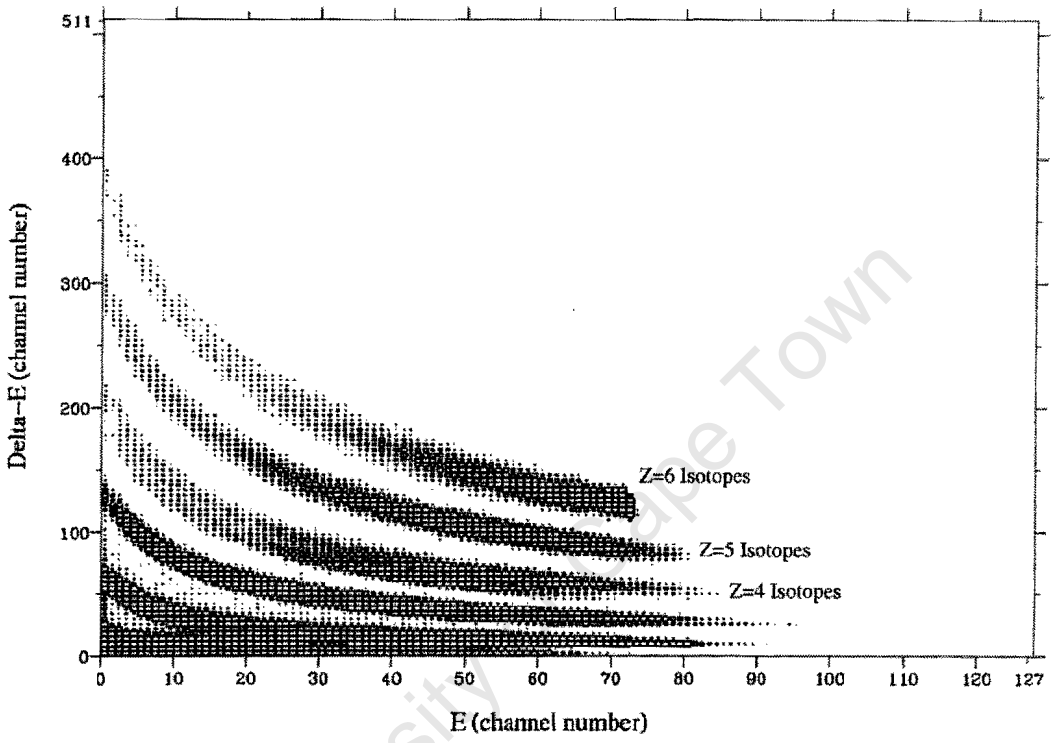

Figure 5.1: A sample PID spectrum (at an incident energy of 400 MeV) showing the partial overlapping of kinematic loci.

The first step in the reduction of the data, once the detectors had been accurately calibrated, was the identification of particles. The standard $\Delta E - E$ method was used, where advantage was taken of the fact that the energy loss (ΔE) of particles as they pass through an ionising medium is dependant on their properties, specifically charge Z, mass A and velocity β. The dependance is given by the well-known Bethe-Bloch

equation [53, 59]), which is given by

$$-\frac{dE}{dx} = 2\pi N_A r_e^2 m_e c^2 \rho \frac{Z}{A}\frac{z^2}{\beta^2}\left[\ln\left(\frac{2m_e\gamma^2 v^2 W_{max}}{I^2}\right) - 2\beta^2 - \delta - 2\frac{C}{Z}\right] \quad (5.1)$$

where

r_e : classical electron radius

m_e : mass of the electron

N_A : Avogadro's number

I : mean excitation potential

Z : atomic number of absorbing material

A : atomic mass of absorbing material

ρ : density of absorbing material

z : charge if incident particle

β : velocity of incident particle $\left(\beta = \frac{v}{c}\right)$

γ : relativistic factor $\left(\gamma = \frac{1}{\sqrt{1-\beta^2}}\right)$

δ : density correction

C : shell correction, and

W_{max} : maximum energy transfer in a single collision $\left(W_{max} = \frac{2m_e c^2\eta^2}{1+2s\sqrt{1+\eta^2}+s^2}\right)$ where

- $s = \frac{m_e}{M}$ where M is the mass of the projectile
- $\eta = \beta\gamma$.

If $M \gg m_e$, which is the case with all the measured ejectiles, then $W_{max} \simeq 2m_e c^2\eta^2$.

This is essentially of the form

$$-\frac{dE}{E} \propto \frac{MZ^2}{E} \tag{5.2}$$

in the non-relativistic limit, where it is clear that the energy loss is more sensitive to the charge than the mass. Thus, particles with a given set of A and Z would have a particular energy loss profile and one could use this to identify them.

Particle **ID**entification spectra (PID) of all the detected ions from H to C were measured, but the nonlinearity of these made the setting of accurate gates around loci somewhat difficult. To overcome this, a linearised form of the Bethe-Bloch equations was used, which mapped the **PID** to a so-called 'mass spectrum', as described below.

5.3.2 Mass Spectra gates

The main objective of the experiment was to measure the double differential cross-sections of the ^{7}Be and ^{9}Be fragments. To do this, their energy spectra had to be extracted from the linearised **PID** spectra - the so called 'mass spectra'. The loci were well separated at low incident energies, but as the beam energy increased, their separation became less and less distinct, until at 400 MeV there were several loci that became partly fused with their neighbours. To overcome this problem, the **PID** were mapped to a so-called 'mass spectrum', using the following parameter M :

$$M \propto [(E + \Delta E)^\gamma - E^\gamma]$$

where M is the approximate mass of the ion, E is the energy (channel number) detected in the stopping NaI(Tl) detector, ΔE is the energy (channel number) detected in the Si detector and γ is a constant which is chosen to optimise the separation of the loci. Usually γ lies in the range $1.6 \leq \gamma \leq 1.9$; in our experiment, it was chosen to be $\gamma = 1.75$. With this new mass spectrum, the particle loci are better defined and largely linear, simplifying the process of drawing gates around them. An example of a mass spectrum is shown in figure 5.2. Naturally, this introduced some uncertainty into our calculations, but this was estimated to be less than 5 % .

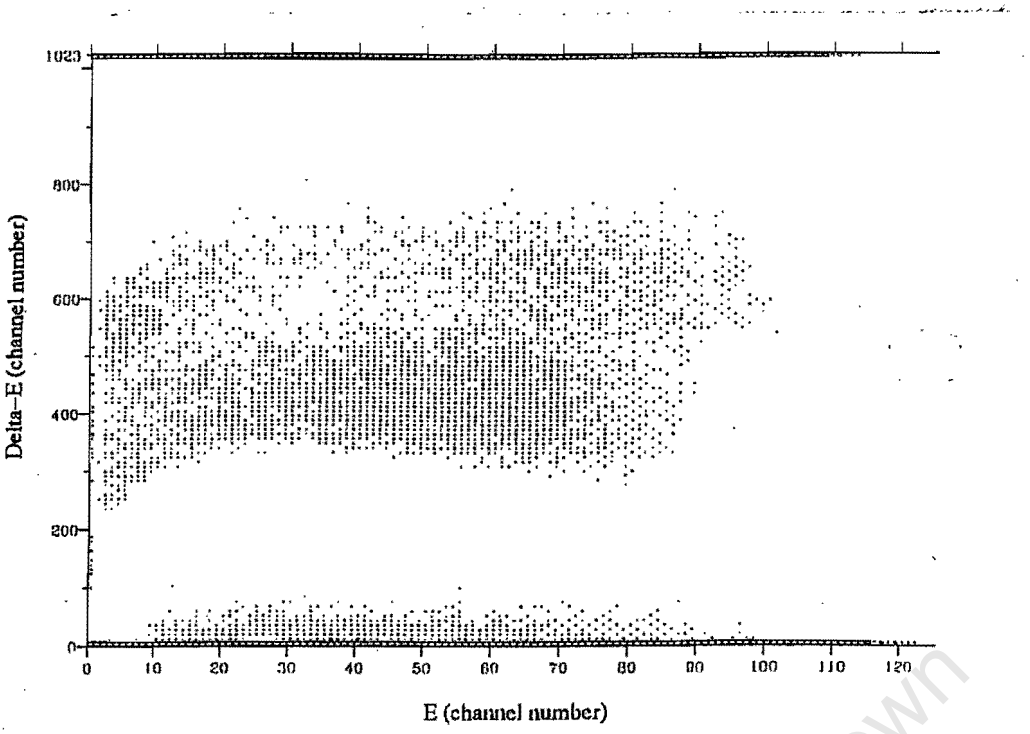

Figure 5.2: An example of a mass spectrum, showing the loci of ^{7}Be (lower) and ^{9}Be (upper) at an incident energy of 400 MeV. Note that although the loci are partially overlapping, they are nearly linear with energy, except at low energy. This facilitates the setting of PID gates.

5.4 Data Acquisition Procedure

The data acquisition procedure was entirely computer-controlled. Events were written directly onto disk storage by the data acquisition software (for replay later) and were also processed by a rough online sorting code for real time information. Once all the experimental runs had been taken and backed up to magnetic tape, the online sorting code was modified to include rigorous calibration and various correction factors (see below). A file was needed to declare the necessary memory allocation. While this file (which only needed to be compiled and run once) set up the data areas, another file would take care of the actual event-by-event offline replay sorting. This file, known as the **EVAL** file, would process each event one by one, ensuring that they were properly identified and that the relevant histograms were incremented. The other functions of the **EVAL** file were to

- declare the necessary 1-D and 2-D histograms (**PID** spectra, mass functions, calibrated particle energy spectra, pulser spectra, *etc.*),
- define experimental settings, such as the current integrator range
- define normalisation factors for the two telescopes (*i.e.* bins per MeV), pulser reference values, *etc.*
- define mass function variables for the various ions, so that they would be displayed properly on the terminal.

As intimated in the previous chapter, the **EVAL** code contained certain subroutines necessary for the sorting and calibration of the data.

CIGET (Current Integrator GET) Was necessary to get the range and integrated current from the CI electronics (used later in calculating the normalised cross-section).

BACK Subroutine to calculate the pulser centroid every 100 counts and correct all NaI raw spectra for drift.

ENERGY Subroutine to calibrate the NaI energy. Parameterisation based on Michaelian's code predictions.

LIDEAD, BE7DEAD, BE9DEAD,*etc.* Subroutines to calculate the energy correction due to the 7 μm HAVAR dead layer of the NaI detectors.

Once the XSYS sorting package had been initialised and an event file read, the sorting procedure would proceed automatically until the end of the last buffer. One could then save the sorted and calibrated data set, in preparation for its conversion into absolute cross-section (see below). A schematic outline of the sorting procedure followed by the **EVAL** code is shown in figure 5.3.

5.5 Corrections

5.5.1 Gain drift corrections built into the EVAL code

The photomultiplier tube of a NaI detector converts a weak electronic signal from the photocathode of a few hundred to a couple of hundred thousand electrons into a measurable pulse. This pulse is shaped by the preamp and then sent to the amplifier to be processed by the electronic modules. The PMT's are very sensitive instruments and changes in count rate could result in a change in the gain of the device [53]. It is thus very important to monitor the gain of the PMT's and keep it as a reference value, so that any shift in gain over time can be corrected for.

Gain drifts were monitored by a LED built into each NaI detector. These were fired by a pre-scaled pulser signal (see chapter 3). The pulser peaks were monitored every 100 pulser events, when their centroid was calculated and compared to the reference value. If the pulser peak position had changed, a drift correction parameter was generated by the EVAL code and applied to the data in a relevant fashion. In this way, we were able to maintain the original gain of the PMT's, and so eliminate any errors that might have arisen from a change in gain over time.

5.5.2 Dead layer corrections

In each of our detector telescopes, we had a so-called *dead layer* which resulted in a reduction in the energy of an incoming particle before it entered the NaI detector. It was necessary to calculate this "*missing energy*" and add it to the nominal value detected by the NaI detector, to obtain the true energy of the incident particle. The dead layer was a 7 μm thick Havar foil in front of the scintillator to protect the hygroscopic NaI crystal.

A FORTRAN subroutine was written and called by the EVAL sorting code, to correct for the energy deficit due to these dead layers. The energy loss ΔE was parameterised as a function of the detected energy E, by a function of the form

$$\Delta E = \left[a + b \cdot \left(\frac{E}{\ln E}\right) + \frac{c}{E^2}\right], \tag{5.3}$$

Ion	a	b	c
Li	0.030894	0.042319	0.154072
^{7}Be	0.0268199	0.0220656	1.7087239
^{9}Be	0.0335562	0.0178579	0.1832457
Be_{tot}	0.030188	0.019962	0.945985
B	0.028951	0.009932	0.285088
^{12}C	0.0251635	0.0030783	0.2267269

Table 5.1: Dead layer parameters used in the sorting code subroutines

where E is the calibrated energy measured in the NaI(Tl) detector. The constants a, b, c were different for each ion. Their respective values are given in table 5.1.

5.6 Conversion to Absolute Cross-Section

Once we had carefully calculated and applied all the correction factors, we were in a position to calculate the cross-sections of the data we had recorded. This is considered as the probability of a particular reaction taking place, and is calculated by converting the counts per channel into an absolute number by applying the appropriate conversion factor. This conversion factor is obtained from relevant experimental quantities and details of a particular run,

- Total charge collected during a run Q
- Dead time correction factor DT (see chapter 3)

Combining these values, we obtain a relation for the double differential cross-section:

$$\frac{d^2\sigma}{dEd\Omega} = N(E) \cdot \frac{eq}{\rho Q} \cdot \frac{10^{30}}{\Delta E \Delta\Omega} \cdot \cos\theta \cdot DT \tag{5.4}$$

where:

- e — Electronic charge : $1.19 \cdot 10^{-19}$C

- ρ — Target density (g/μm) $= \frac{\lambda}{A} \cdot N_A$ where
  - λ — Target thickness : 1.7205 (μm)
  - A — Target molecular weight : 92.9064(g/mol)
  - N_A — Avogadro's number : $6.022045 \cdot 10^{23}$
- ΔE — Energy/bin : 4 MeV
- $N(E)$ — Corrected counts per bin
- $\Delta\Omega$ — Target solid angle : $1.057 \cdot 10^{-3}$ sr.
- q — Charge of incoming ion (assumed to be +6, since all electrons would be stripped once the ion entered the target.)
- θ — Target angular offset (≈ 0).
- The factor 10^{30} is necessary for the conversion between cm to μb.

A FORTRAN code `SIGMA` was written to implement equation (5.4), which called as input the above quantities and converted an `XSYS` spectrum of counts(channel) to a double differential cross-section, in $\frac{\mu b}{MeV \cdot sr}$.

5.7 Error analysis

5.7.1 Statistical errors

The errorbars shown in the plots of the cross-sections represent the statistical errors in the experiment only, calculated from the Poisson distribution. The uncertainty of measurement is given by the square root of the number N of counts obtained during a run:

$$\sigma = \frac{\sqrt{N}}{N} \tag{5.5}$$

Thus, to obtain a statistical accuracy of ~3%, the number of counts in a bin had to be more than 1000 counts, which was achieved for most of the runs.

5.7.2 Systematic errors

This subsection deals with the various uncertainties which were assumed to contribute to the overall systematic error in the experiment. These uncertainties are listed in Table 5.2.

Target thickness

The uncertainty in the target thickness was no larger than 5% and was estimated using energy-loss predictions of α-particles from a ^{228}Th source. Its uncertainty came primarily from the unevenness of the surface.

Detector solid angle

The uncertainty in the solid angle subtended by the detector from the target is determined by the uncertainty in the radius of the collimator opening, the distance from the target centre to the centre of the collimator exit, and the beam spot diameter on the target. The combined error in the solid angle was thus estimated from these values (which are given in chapter 2). With an uncertainty of ~ 0.2 mm (which corresponds to $< 1\%$)in the distance from the target centre to the centre of the exit of the collimator and an uncertainty of ~ 0.03 mm ($< 5\%$) in the radius of the collimator opening, the maximum uncertainty in the solid angle is estimated to be <1%.

Detector calibrations

The uncertainty in the energy spectra was mostly due to the resolution of the NaI(Tl) detectors. This led to an uncertainty of $\sim$1 MeV.

Particle identification

The uncertainty of accurately identifying a particle came primarily from the overlapping loci of neighbouring ions, so gates were carefully set so as to minimise the contributions of neighbouring loci. The possibility also exists that an event would lie outside the gate, but this was minimised by selecting the gates so as to include all of the high-ΔE events.

Source	Percentage Error
target thickness	5
detector solid angle	1
detector calibrations	< 1
particle identification	< 10
electronic dead time	2
current integrator	< 15

Table 5.2: Summary of the systematic errors in the experiment

While it is difficult to estimate the uncertainty introduced into the experiment by this factor, all efforts were made to reduce it as much as possible, by carefully selecting gates. An estimate of 10% was thus chosen as a conservative upper limit.

Electronic dead time

Electronic dead time was monitored throughout the experiment and kept to less than 2%. This did not significantly contribute to the systematic error, since the dead time was corrected for during offline replay of the data, in the EVAL file. The uncertainty in the dead time correction is negligible.

Current Integrator

The uncertainty in the amount of charge collected by the current integrator (Q) is another factor which contributed to the overall systematic error. This was estimated to be no more than 15 % [44]

In summary, the combination of all these systematic errors resulted in a total estimated uncertainty of no more than 20%, which is a conservative upper limit.

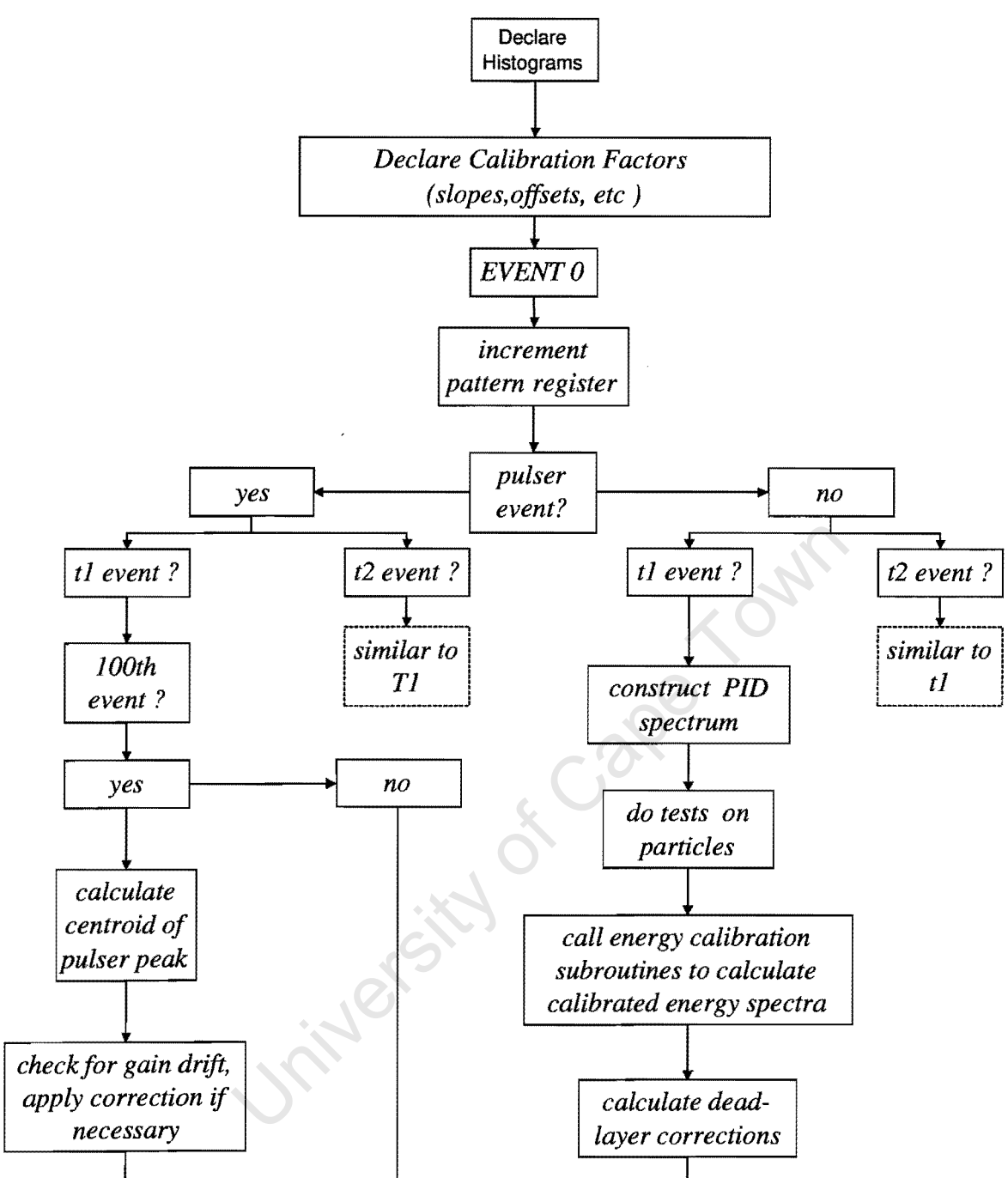

Figure 5.3: Schematic diagram showing the data sorting procedure followed by the EVAL code

Chapter 6

Results

6.1 Overview

Using the theoretical approaches described in chapter 2, particle multiplicities were calculated for the breakup and coalescence contributions [70]. To convert these particle multiplicities to differential cross-sections, the relevant normalisation had to be applied to each component, in order to compare the spectra to the experimental data. For the coalescence contribution, this normalisation was the product of the complete fusion cross-section σ_{cf} and the survival probability factor (see equation 2.30) R : $\lambda_{BME} = \sigma_{cf}R$. For ^{7}Be, $R = 0.2$ was used, while for ^{9}Be, $R = 0.4$ [71].

For the breakup contribution, the relevant normalisation of the multiplicities was

		^{7}Be		^{9}Be	
E_{inc} (MeV)	σ_{cf} (mb)	λ_{BME}	λ_{bu}	λ_{BME}	λ_{bu}
200.	766.	153.2	10	306.4	80
300.	511.	102.2	20	204.4	66
400.	383.	76.6	30	153.2	90

Table 6.1: Parameters used in the calculation of the normalised theoretical cross-section. The BME normalisation factor λ_{BME} is the product of the complete fusion cross-section σ_{cf} and the survival probability R, as described in the text.

Beam Energy (MeV)	8°	10°	12°
	λ'		
200	1.8	1.6	1.2
300	1.6	1.43	1.00
400	1.35	1.00	1.00

Table 6.2: Free parameters λ' that were applied the approximate ^{7}Be breakup cross-section λ_{bu}, which is used to normalise the calculated ^{7}Be breakup multiplicities in order to reproduce the experimental data (see explanation in the text).

the breakup reaction cross-section. As the true breakup reaction cross-section for the processes we were investigating ($^{12}C \longrightarrow {}^{7}Be + {}^{5}He$ and $^{12}C \longrightarrow {}^{9}Be + {}^{3}He$) are not well known at all, they have to be estimated. This is done by trying to reproduce the total breakup cross-section for the particular isotopes, ^{7}Be and ^{9}Be, although even this value is used only as an input parameter in the Monte-Carlo calculation of the predicted breakup multiplicities. A free parameter λ' was applied to the calculated multiplicities which scales them in order to reproduce the experimental cross-section. This free parameter is an expression of the fact that the breakup 'cross-section' that is given as input to the Monte-Carlo code is not well known.

If one assumes a constant $\lambda' = 1$ for all angles, then the theoretical prediction does fairly well to describe the experimental cross-sections, but fails at very small angles ($\theta < 14°$). Here, the theoretical calculation tends to underestimate the emission of ^{7}Be and overestimate the emission of ^{9}Be. This should not be seen as anything other than an inaccurate choice of λ_{bu}

It must be emphasized that the 'cross-section' that is provided as an input is not the true cross-section of the breakup reaction, since that is not known, but an approximation to it. If the true cross-section where known, or if the cross-section were known better (as is the case when one is normalising the coalescence contribution), then λ' would possibly be closer to unity for all energies and angles. The factors λ' are given in tables 6.2 and 6.3 for the respective isotopes, energies and angles..

Beam Energy (MeV)	8°	10°
	λ'	
200	0.6	0.75
300	0.66	1.00

Table 6.3: Free parameters λ' that were applied the approximate ^{9}Be breakup cross-section λ_{bu}, which is used to normalise the calculated ^{9}Be breakup multiplicities in order to reproduce the experimental data (see explanation in the text).

As discussed in chapter 2, a friction dissipative model of breakup was used to describe the breakup spectra of the ejectiles. With reference to equation 2.19, values of $E_{l,min}$ and kk' were estimated [70] and used to calculate theoretical breakup spectra. These values, along with the total breakup cross-section σ_{bu} and the average energy loss $\overline{\Delta E}$ for the two isotopes of interest in this experiment, ^{7}Be and ^{9}Be, are shown in tables 6.4 and 6.6[1]. The values of the same parameters for ^{8}Be are also shown for comparison in table 6.5.

E_{inc} (MeV)	$E_{l,min}$ (MeV)	kk' (MeV^{-1})	$\overline{\Delta E}$ (MeV)	σ_{bu} (mb)
200	27	0.1	37	10
300	60	0.07	74	20
400	75	0.06	92	30

Table 6.4: Parameter values for the breakup of ^{12}C into ^{7}Be and ^{5}He as a function of incident energy.

6.2 Double differential cross-sections

Contributions due to binary breakup and coalescence to the overall cross-section were calculated, as described above and in chapter 2. A comparison between these calculated

[1]Note again that the value for σ_{bu} should not be seen as the true breakup cross-section (since that is not known), but a model parameter

E_{inc} (MeV)	$E_{l,min}$ (MeV)	kk' (MeV^{-1})	$\overline{\Delta E}$ (MeV)	σ_{bu} (mb)
200	50	0.2	55	80
300	55	0.06	72	105
400	70	0.04	95	109

Table 6.5: Parameter values for the breakup of ^{12}C into ^{8}Be and ^{4}He as a function of incident energy.

E_{inc} (MeV)	$E_{l,min}$ (MeV)	kk' (MeV^{-1})	$\overline{\Delta E}$ (MeV)	σ_{bu}
200	10	0.072	24	80
300	35	0.1	45	66
400	35	0.07	49	90

Table 6.6: Parameter values for the breakup of ^{12}C into ^{9}Be and ^{3}He as a function of incident energy.

contributions and the experimentally measured cross-sections of ^{7}Be is shown in figures 6.1-6.2.

6.2.1 400 MeV Spectra

An examination of the global features of the data at 400 MeV shows that satisfactory overall agreement between the model and the measured cross-sections is apparent. At small emission angles (below about 12°), one notices a slight shift between the measured breakup peak and that predicted by the model. The shift is quite small (less than $\sim$ 20 MeV at 8°) and disappears quickly as the angle increases; it appears more significant in the case of ^{7}Be than ^{9}Be. At 14° it is unnoticeable. As the detector angle increases, there is seen to be an underestimation of the measured cross-section in the so-called *transition régime*, which is the energy region where the dominant reaction mechanism moves from breakup to coalescence. At an incident energy of 400 MeV, this region is estimated to be roughly 80 MeV - 120 MeV for ^{7}Be and a similar range for ^{9}Be.

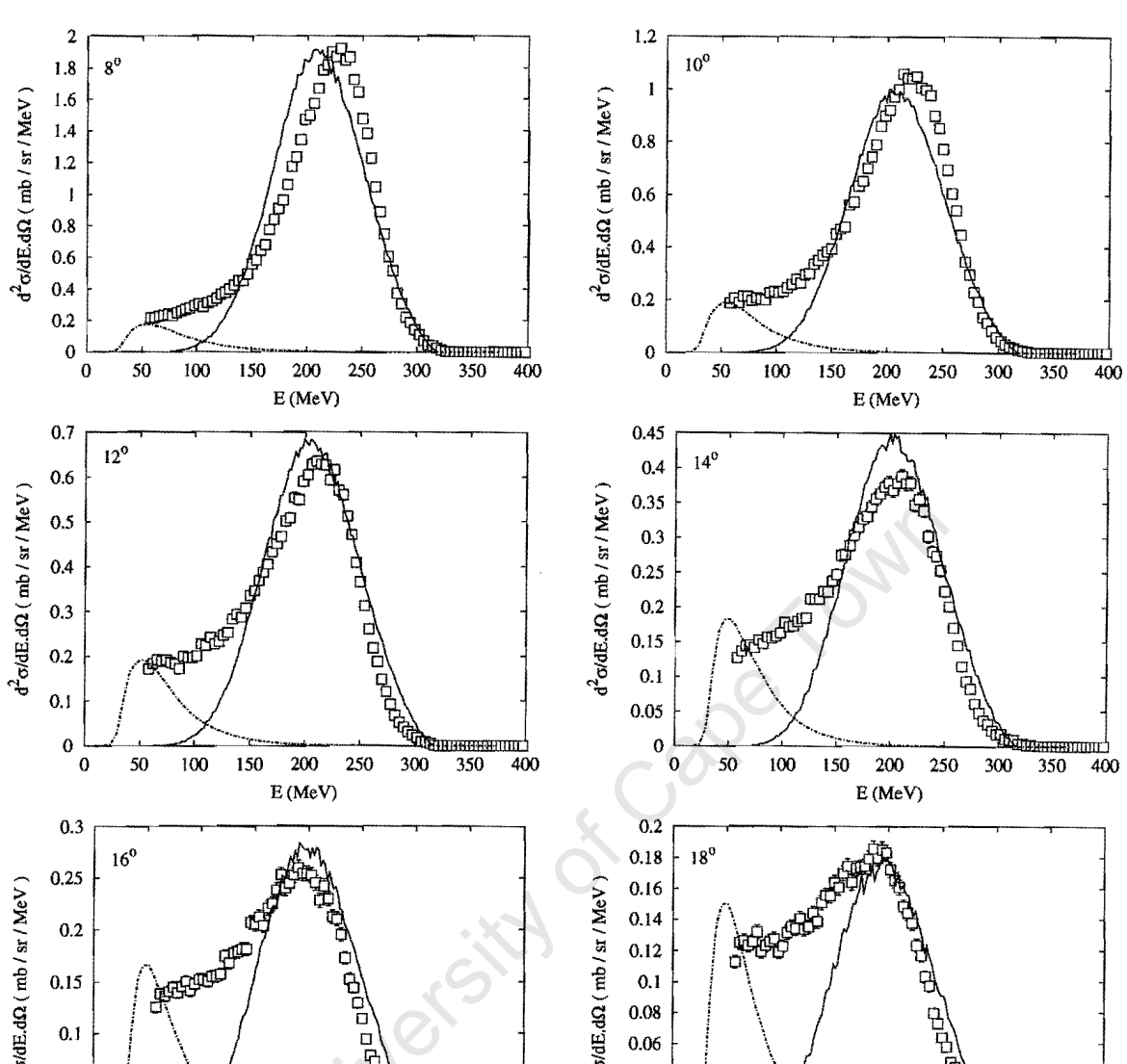

Figure 6.1: The double-differential cross-sections of ^{7}Be at an incident energy of 400 MeV. The calculated contributions due to breakup (solid line) and coalescence (dashed line) are shown, along with the experimental data. Note that the statistical errorbars on the experimental data may be smaller than the plotting symbol used. See table 6.4 for the relevant normalisation factors.

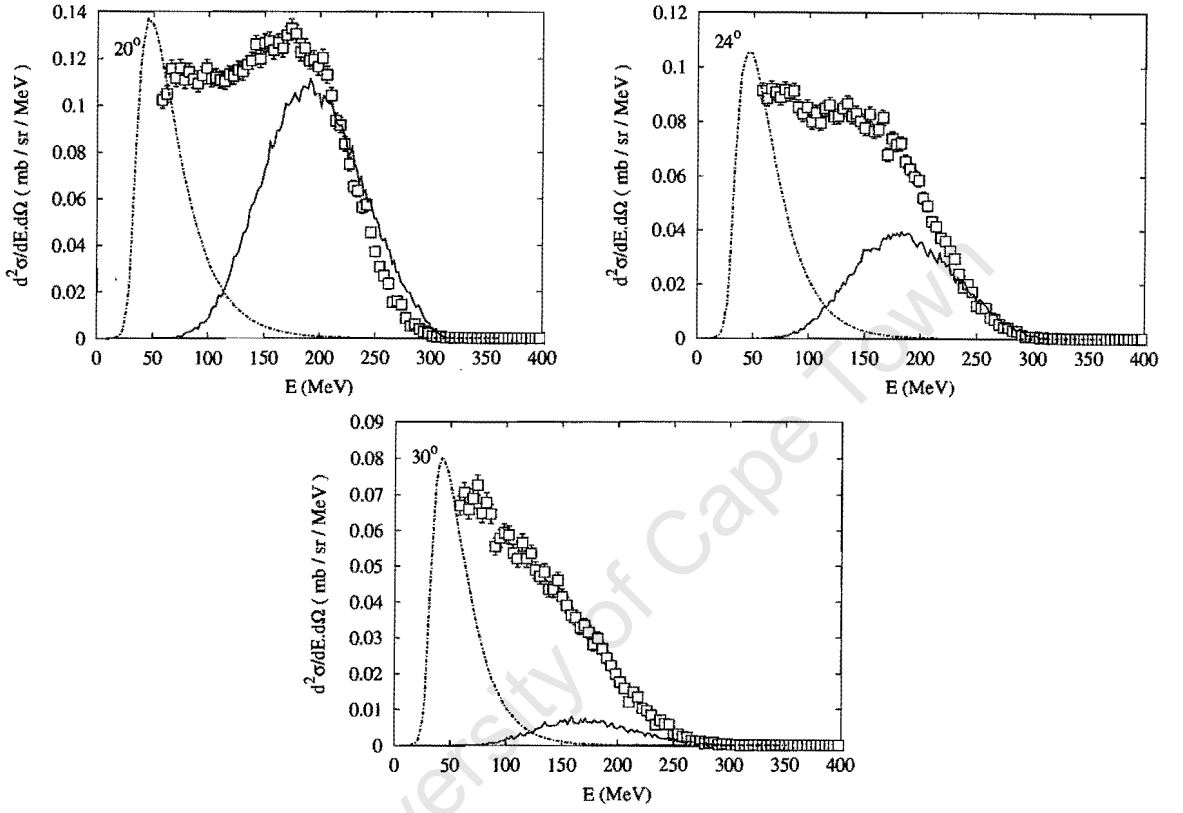

Figure 6.2: Measured and calculated double differential cross-sections for ^{7}Be with an incident energy of 400 MeV. Shown are data for the large emission angles (20° - 30°). See the caption to figure 6.1

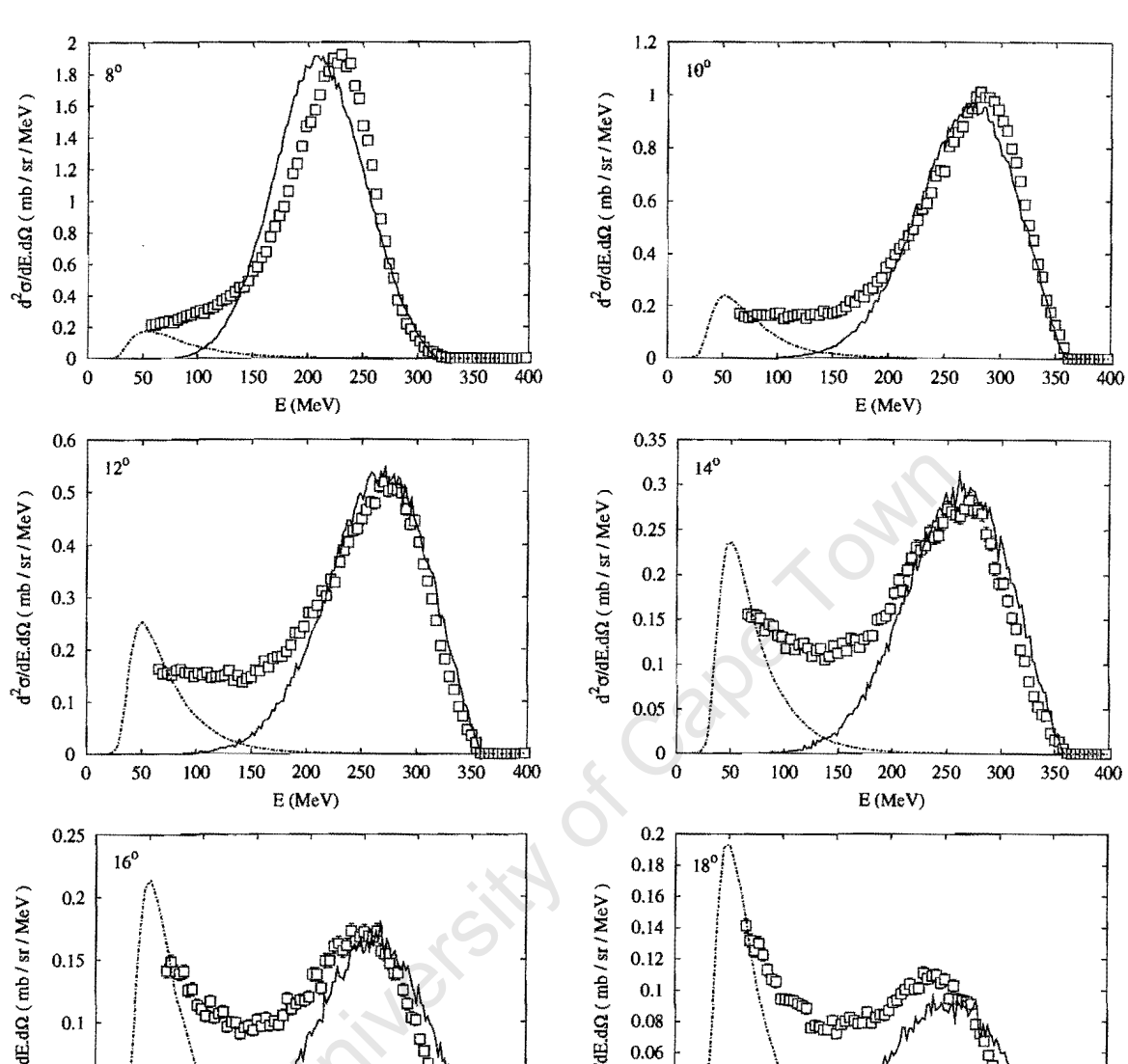

Figure 6.3: The comparison between calculated contributions from breakup and coalescence for ^{9}Be and corresponding experimental data at an incident energy of 400 MeV, for emission angles between 8° and 18°. See the caption to figure 6.1

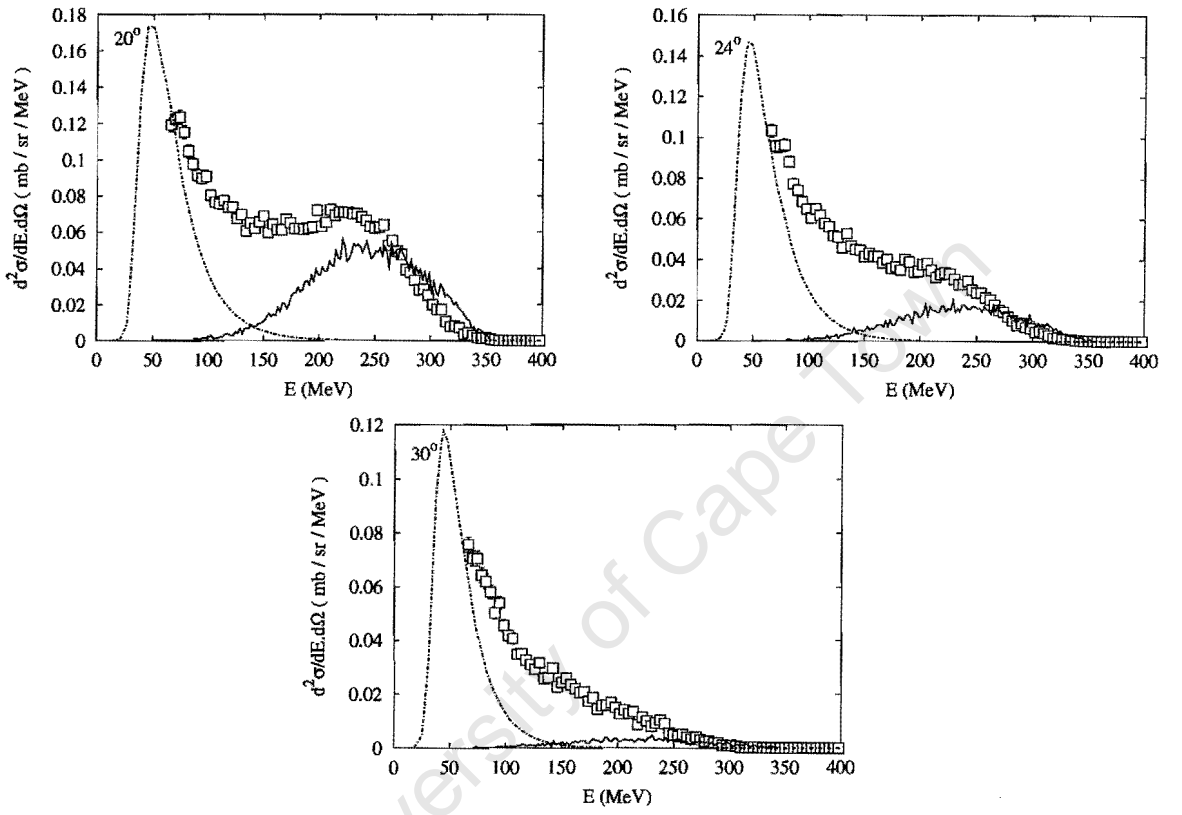

Figure 6.4: The comparison between calculated contributions from breakup and coalescence for ^{9}Be and corresponding experimental data at an incident energy 400 MeV, for emission angles between 20° and 30°. See the caption to figure 6.1

From 16° the disagreement is more noticeable and accompanied by an asymmetry of the breakup peak of especially ^{7}Be; the slope of the peak on the low-energy side is less steep than on the high-energy side. The effect is less noticeable in the case of the ^{9}Be, although it cannot be confirmed or discounted.

For ^{9}Be, there is a consistent slight overestimation of the breakup peak, except at 12° and 14°, where the data are very well described by the model. It should be noted that the peak of the coalescence contribution lies outside the experimental low-energy threshold, so reliable comparisons between the predicted and measured cross-sections cannot be made with any confidence in this region (below ~50 MeV).

6.2.2 300 MeV Spectra

The ^{7}Be data obtained for the 300 MeV projectile energy are shown in figures 6.5 and 6.6 and the corresponding ^{9}Be data are shown in figures 6.7 and 6.8. For ^{7}Be, there seems to be good overall agreement between the experimental and theoretical cross-sections, apart from two notable exceptions :

- at very small angles (8° and 10°)there is again a slight shift towards lower energy of the theoretical breakup peak, compared to the experimental peak and while, upon very careful examination, one may be able to detect a similar shift at 12°, it cannot be stated with any confidence that the shift is significant;
- at 14° there is a slight underestimation of the breakup peak, although it is impossible to draw any definite conclusion from this isolated discrepancy between the data and model.

There seems to be a trend at low energies for the coalescence contribution to overestimate the measured cross-section, although it must once again be stated that the proximity to the experimental threshold in this region prevents one from making any statement with confidence.

A more interesting fact is that, as in the case for the 400 MeV data, there is an underestimation in the transition régime, where the two reaction mechanisms overlap.

For a projectile energy of 300 MeV, this region is estimated to be from 75 MeV to 125 MeV.

6.2.3 200 MeV Spectra

As in the case of the 400- and 300 MeV data set, when one considers the comparison between the global features of the model's predictions and the measured cross-sections there is seen to be a consistent agreement, apart from a few deviations (see figures 6.9-6.12. The shape of the breakup peak is well described over the full angular range for both isotopes, although there are notable underestimations of the breakup cross-sections at the peak value at small angles. This effect is possibly due to the contamination of other isotopes while setting the gates on the **PID** spectra during data analysis, since the shape of the measured breakup peaks at this energy are quite different to those at 300 MeV and 400 MeV.

While it can be fairly confidently stated that the friction-dissipative breakup description is generally applicable at this energy, the coalescence contribution lies wholly below the experimental threshold for small to intermediate angles ($\theta \leq 24°$) and it is impossible to come to a confident conclusion regarding the accuracy of this description.

In fact, there is some disagreement of the total cross-section of the full angular range at this energy, in both the case of ^{7}Be and ^{9}Be. While the shape is fairly well reproduced for intermediate angles ($12° \leq \theta \leq 18°$), there is significant overestimation for larger angles.

6.3 Discussion

Upon overall investigation of the data, it may be seen that the model is in general a fairly accurate description of the data, with a few consistent deviations. As the incident energy increases, one expects the coalescence contribution to decrease, since the incomplete fusion cross-section will drop due to the fact that the emitted fragment can no longer be contained by the target field. This is indeed observed. The energy

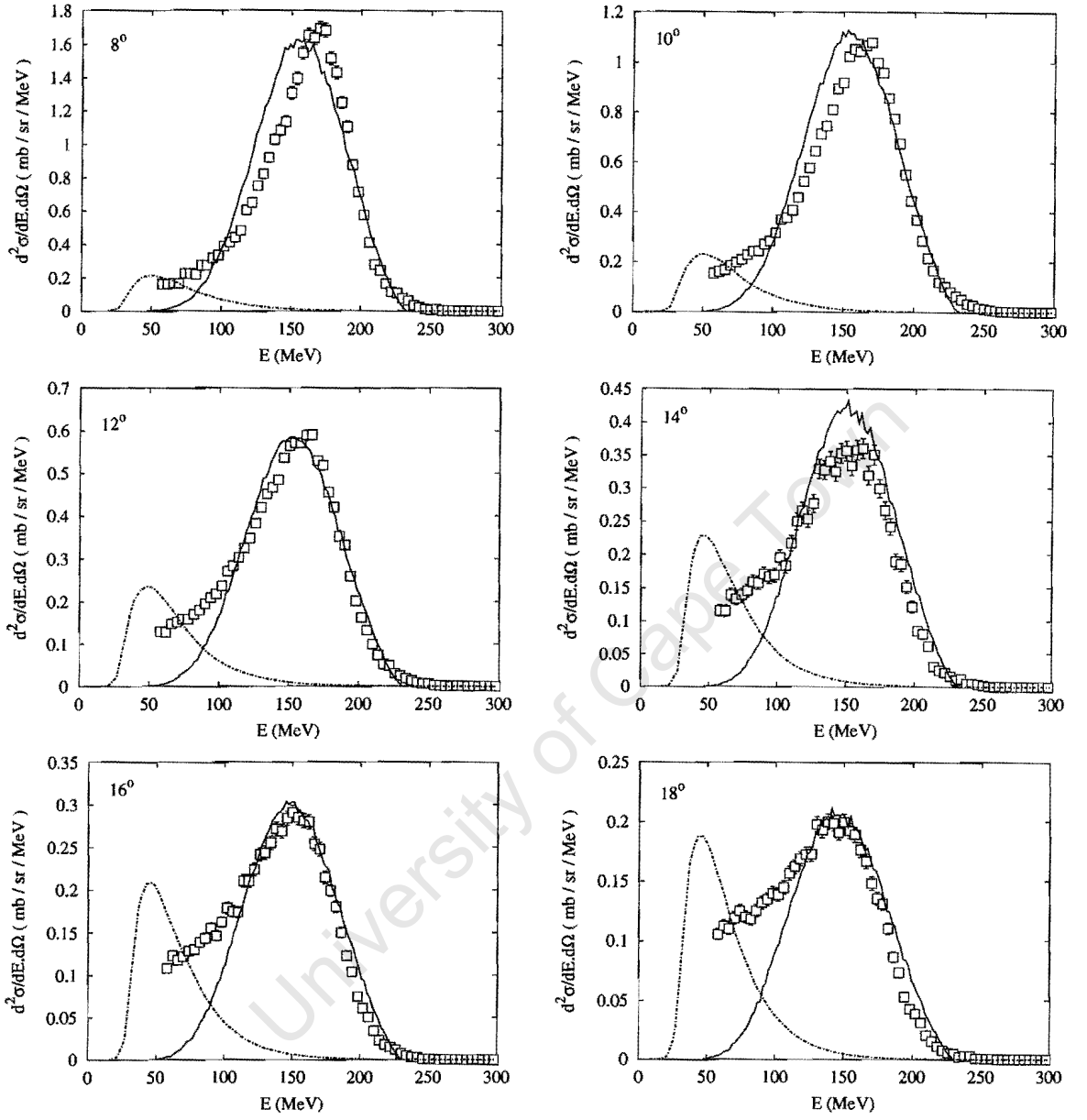

Figure 6.5: The comparison between calculated contributions from breakup and coalescence for ^{7}Be and corresponding experimental data at an incident energy 300 MeV, for emission angles between 8° and 18°. See the caption to figure 6.1

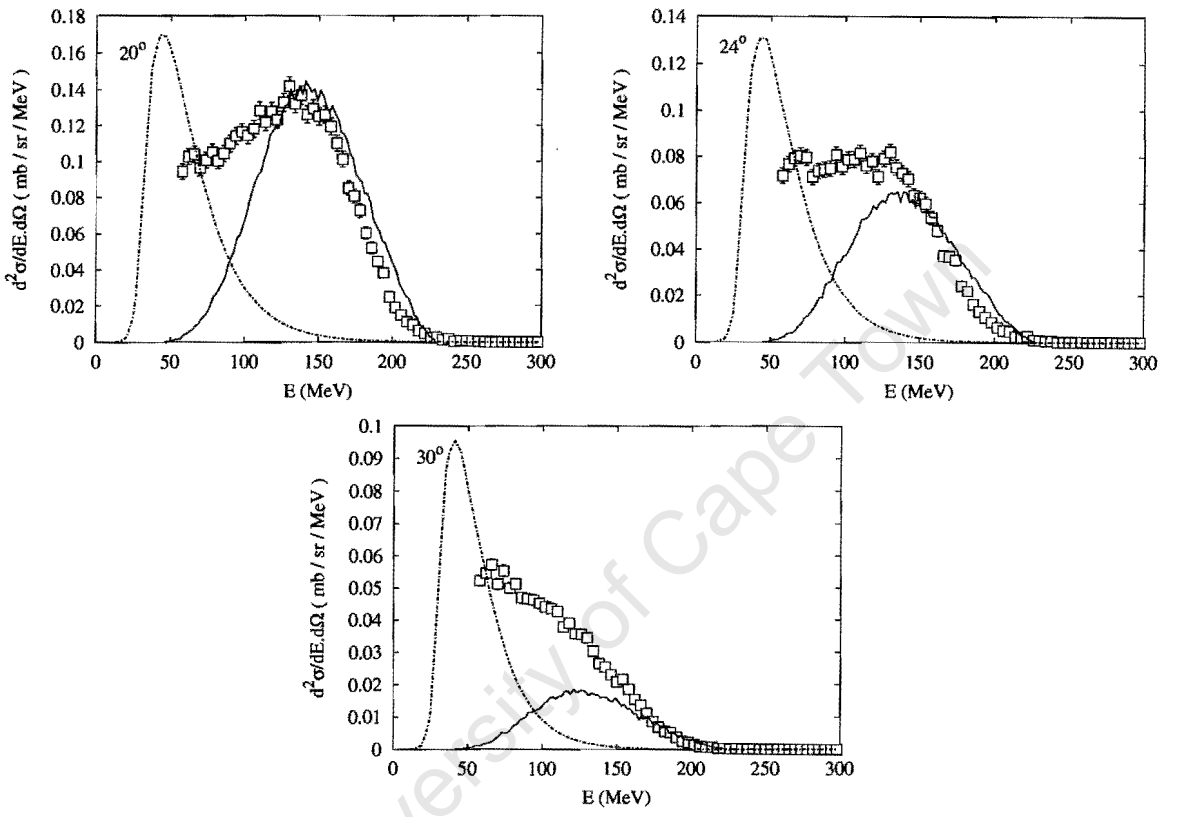

Figure 6.6: The comparison between calculated contributions from breakup and coalescence for ^{7}Be and corresponding experimental data at an incident energy 300 MeV, for emission angles between 20° and 30°. See the caption to figure 6.1

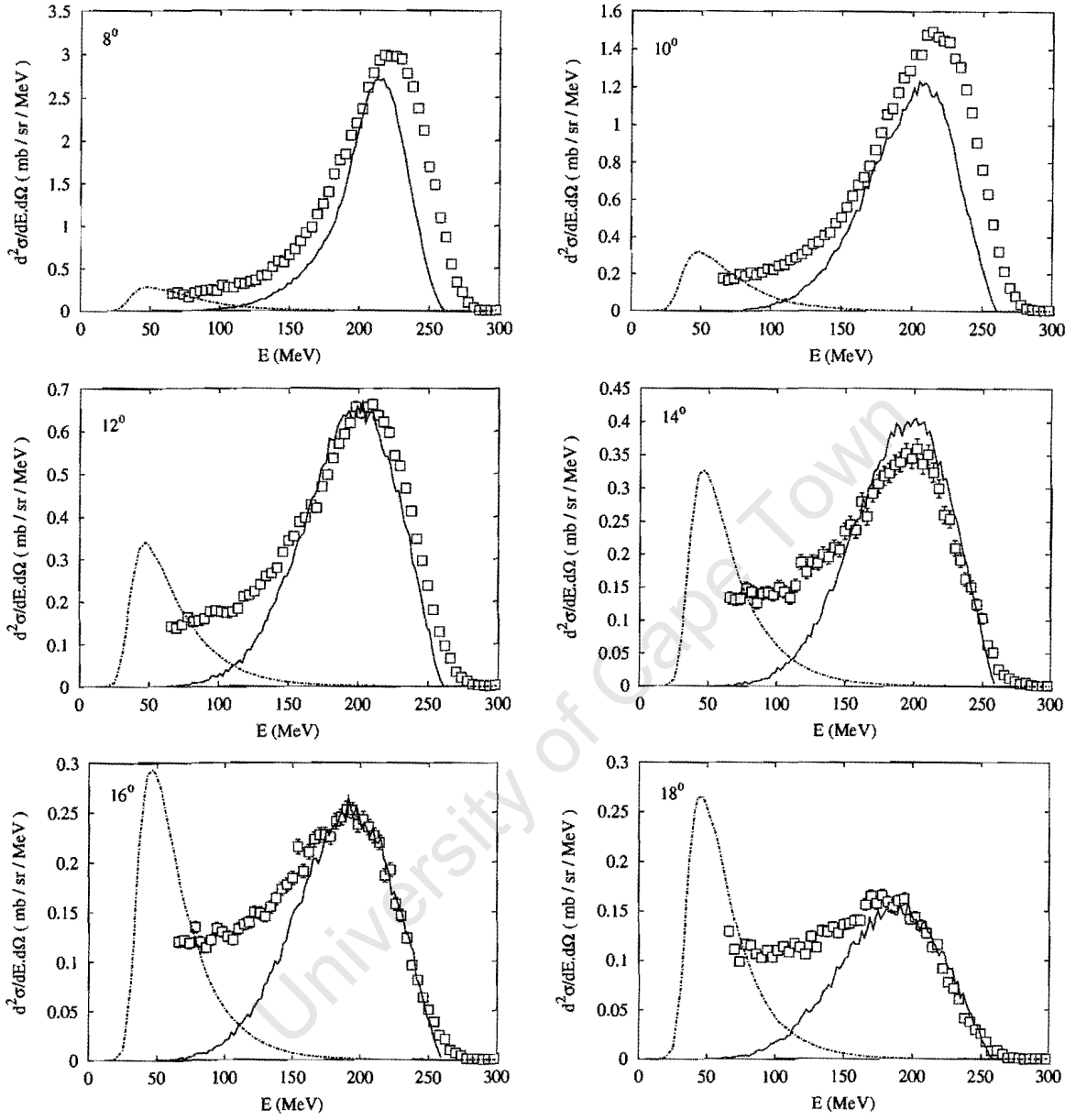

Figure 6.7: The comparison between calculated contributions from breakup and coalescence for ^{9}Be and corresponding experimental data at an incident energy 300 MeV, for emission angles between 8° and 18°. See the caption to figure 6.1

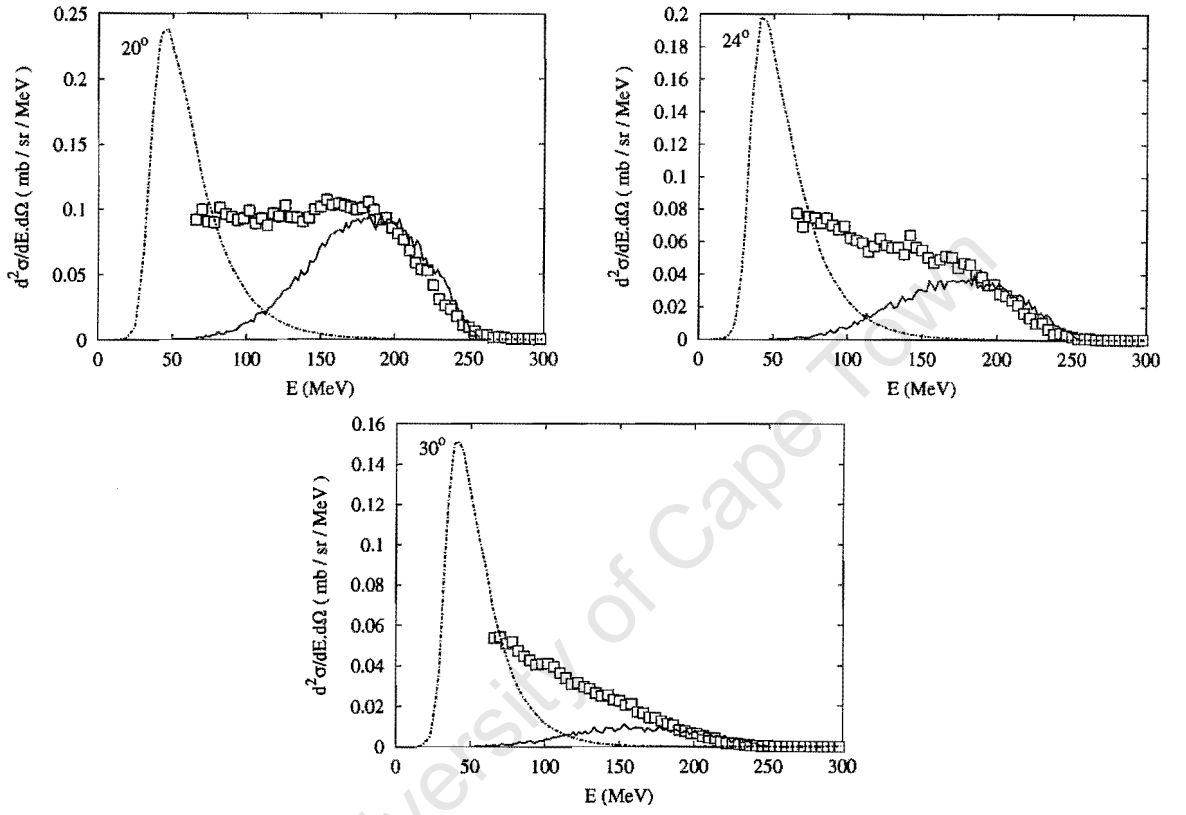

Figure 6.8: The comparison between calculated contributions from breakup and coalescence for ^{9}Be and corresponding experimental data at an incident energy 300 MeV, for emission angles between 20° and 30°. See the caption to figure 6.1

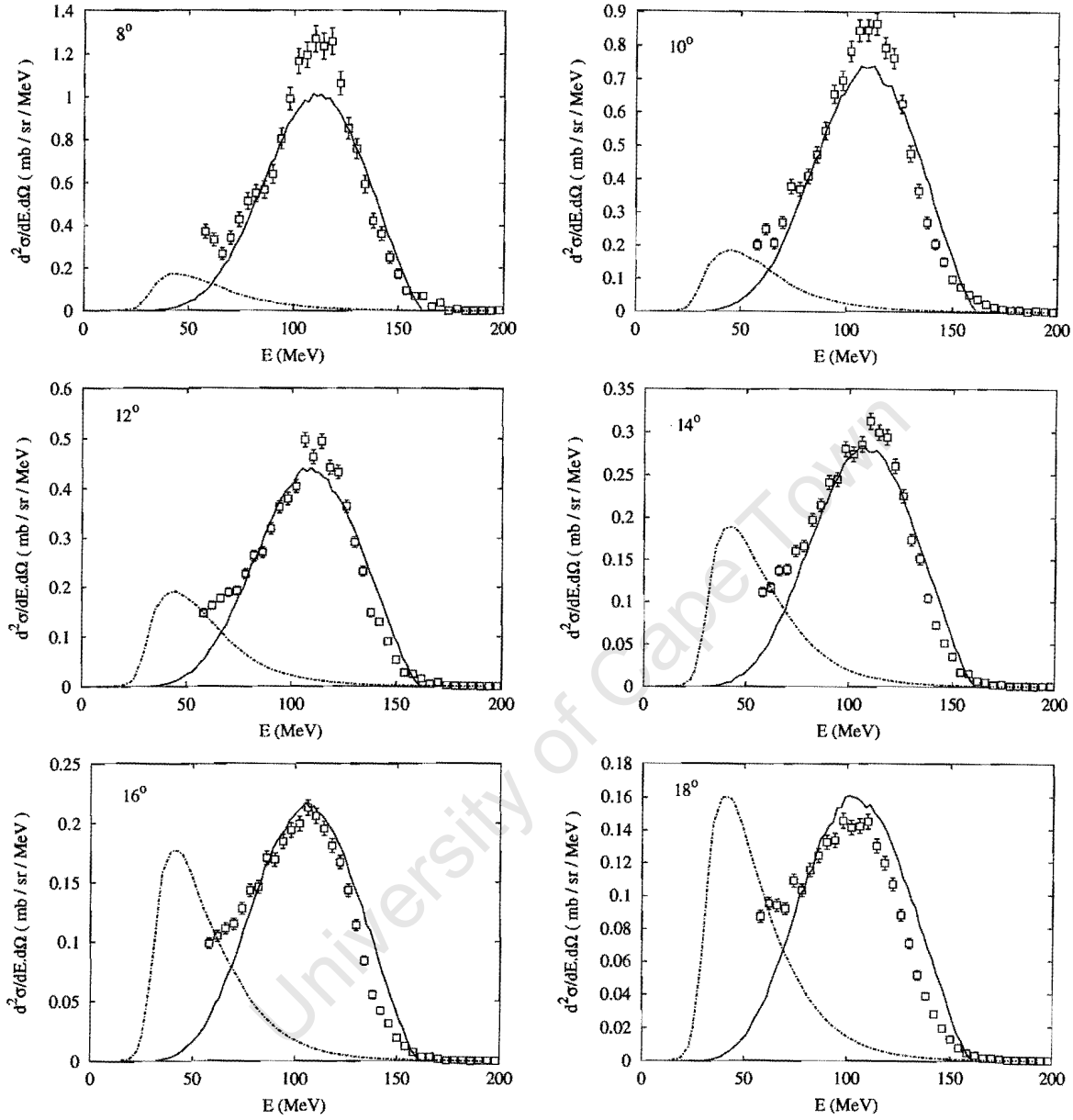

Figure 6.9: The comparison between calculated contributions from breakup and coalescence for ^{7}Be and corresponding experimental data at an incident energy 200 MeV, for emission angles between 8° and 18°. See the caption to figure 6.1

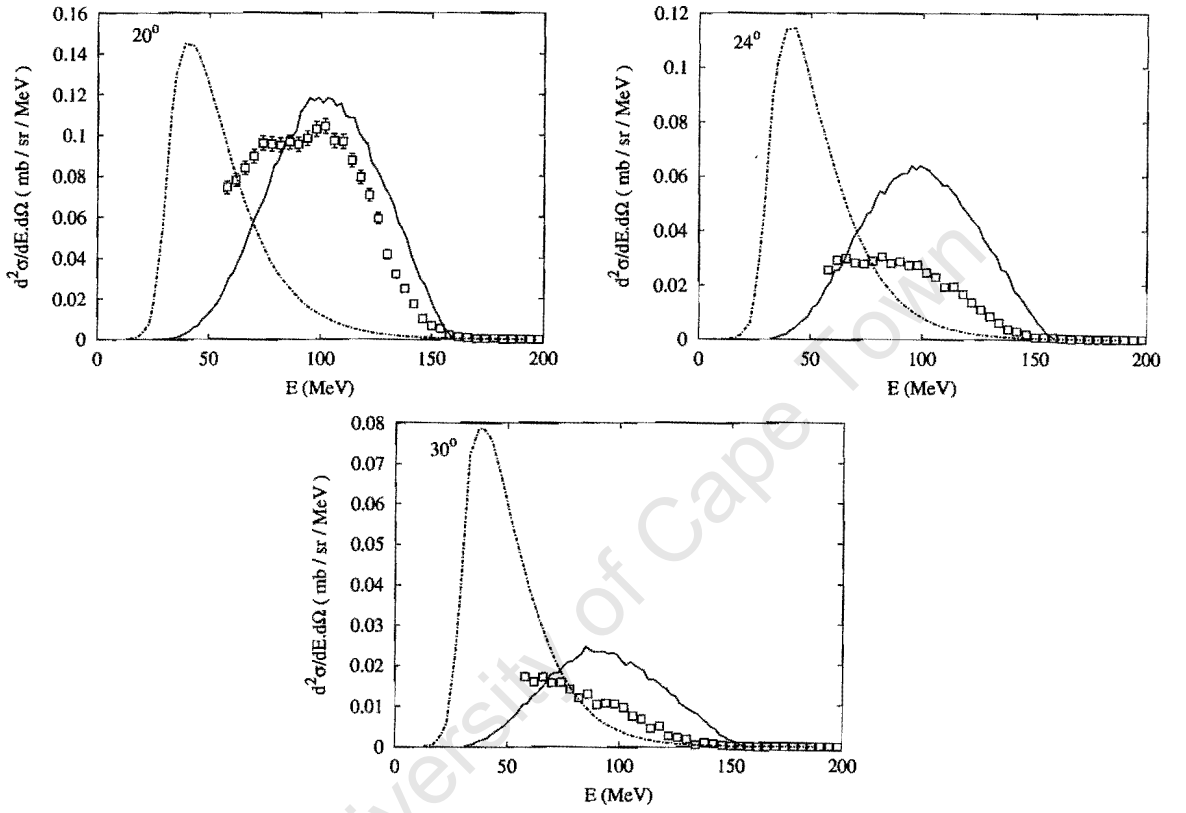

Figure 6.10: The comparison between calculated contributions from breakup and coalescence for ^{7}Be and corresponding experimental data at an incident energy 200 MeV, for emission angles between 8° and 18°. See the caption to figure 6.1

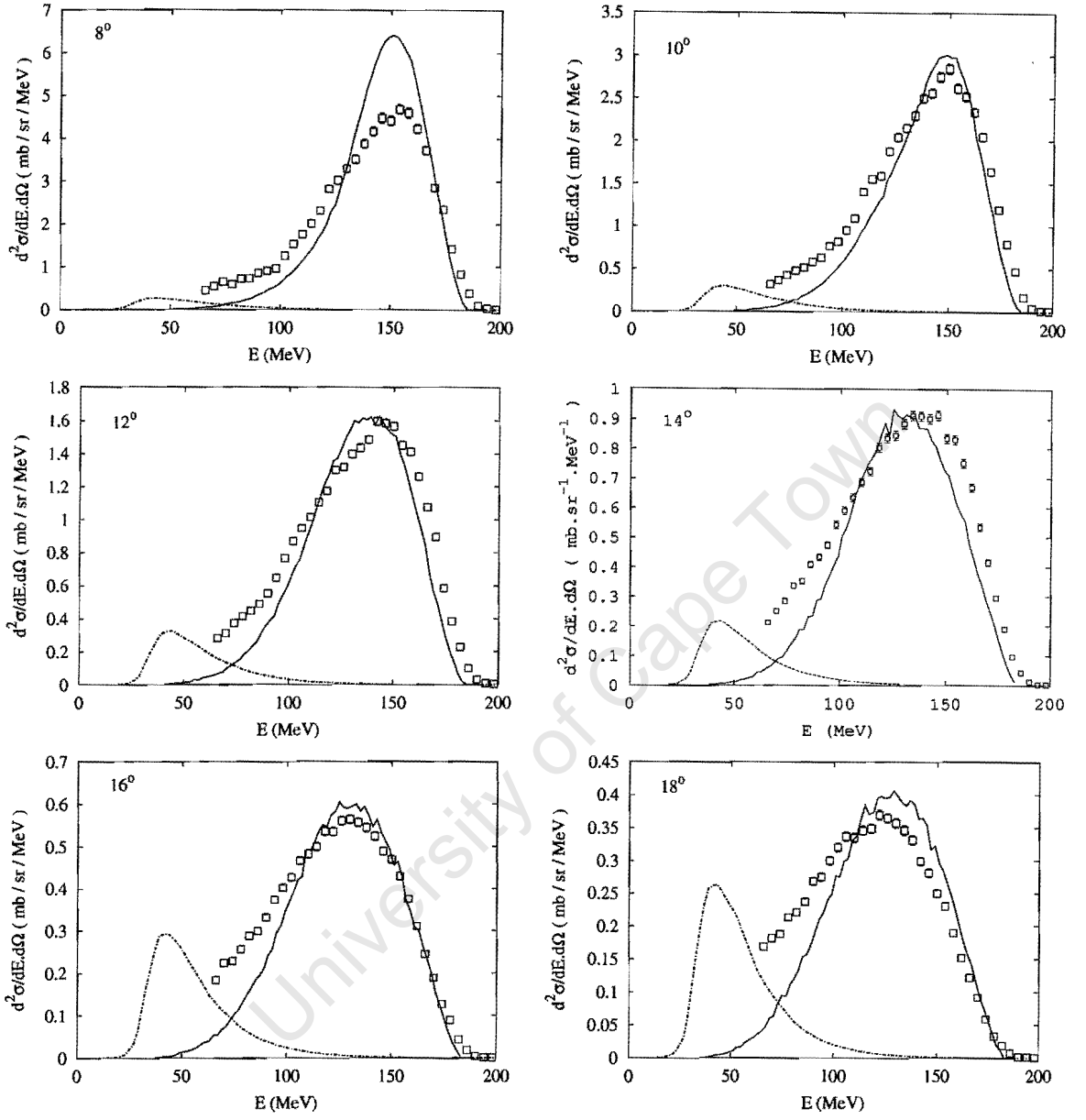

Figure 6.11: The comparison between calculated contributions from breakup and coalescence for ^{9}Be and corresponding experimental data at an incident energy 200 MeV, for emission angles between 8° and 18°. See the caption to figure 6.1

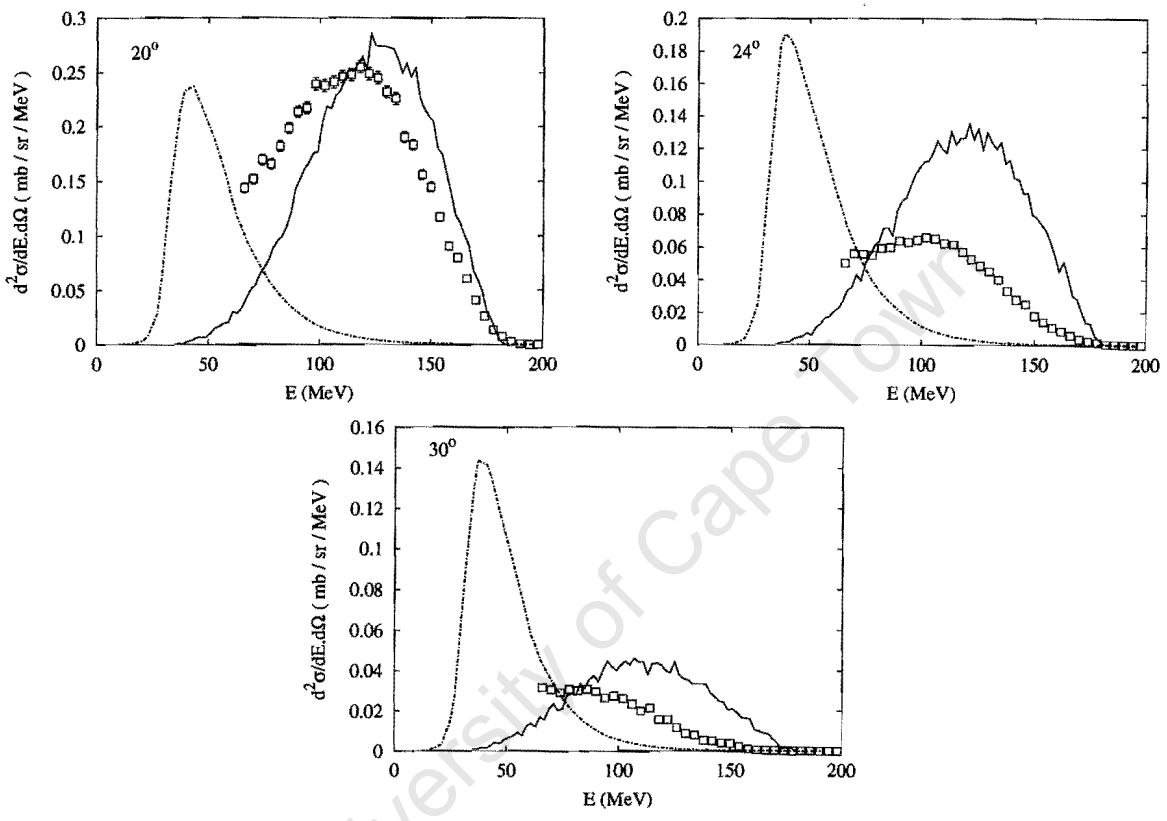

Figure 6.12: The comparison between calculated contributions from breakup and coalescence for ^{9}Be and corresponding experimental data at an incident energy 200 MeV, for emission angles between 20° and 30°. See the caption to figure 6.1

dependance and angular distribution of the cross-sections are reproduced satisfactorily, while the differences between the model and the data indicate, in some cases, areas where the model has taken an overly simplistic view.

The underestimation of the experimental cross-sections in the transition régime may be indicative of the naïve approach taken when describing the friction-dissipative breakup mechanism. In the calculation of the cross-sections, a folding function $P(E_l)$ is used, which is a function of energy alone, and does not take into account the emission angle. The folding function also has a sharp cutoff value, which may not be the optimal description of the situation. The disagreement is more noticeable as the emission angle increases, pointing to the possibility that the value of kk' could vary with angle. In fact, it is not unreasonable to think that the constant kk' could decrease with angle, as suggested by the inelastic scattering data [71]

As seen in figures 6.1, 6.3 and 6.5, even after the multiplication of the the calculated breakup spectra by the factors given in tables 6.2 and 6.3, there is some underestimation of the experimental cross-section at very small angles.

6.4 Angular distribution

Once all of the theoretical spectra for both the coalescence and breakup contributions had been calculated, they were integrated over the energy range, to give a total cross-section at each angle. These total cross-sections were then compared with the energy-integrated cross-sections (see figures 6.13-6.18)

At 200 MeV, it is seen from figures 6.13 and 6.14 that for ^{7}Be, the cross-section at small angles has been somewhat underestimated, while for ^{9}Be in the same region, the agreement between the experimental data and the predicted cross-section is remarkable. For both isotopes, the cross-section is overestimated at large angles, but the effect is larger in the case of ^{7}Be than for ^{9}Be. Above 20°, the ^{7}Be experimental cross-section drops sharply, which we do not observe in the case of ^{9}Be.

In the case of the 300 MeV data, we see a from figures 6.15 and 6.16 that the model gives a fairly good description of cross-sections of both isotopes of interest. Between

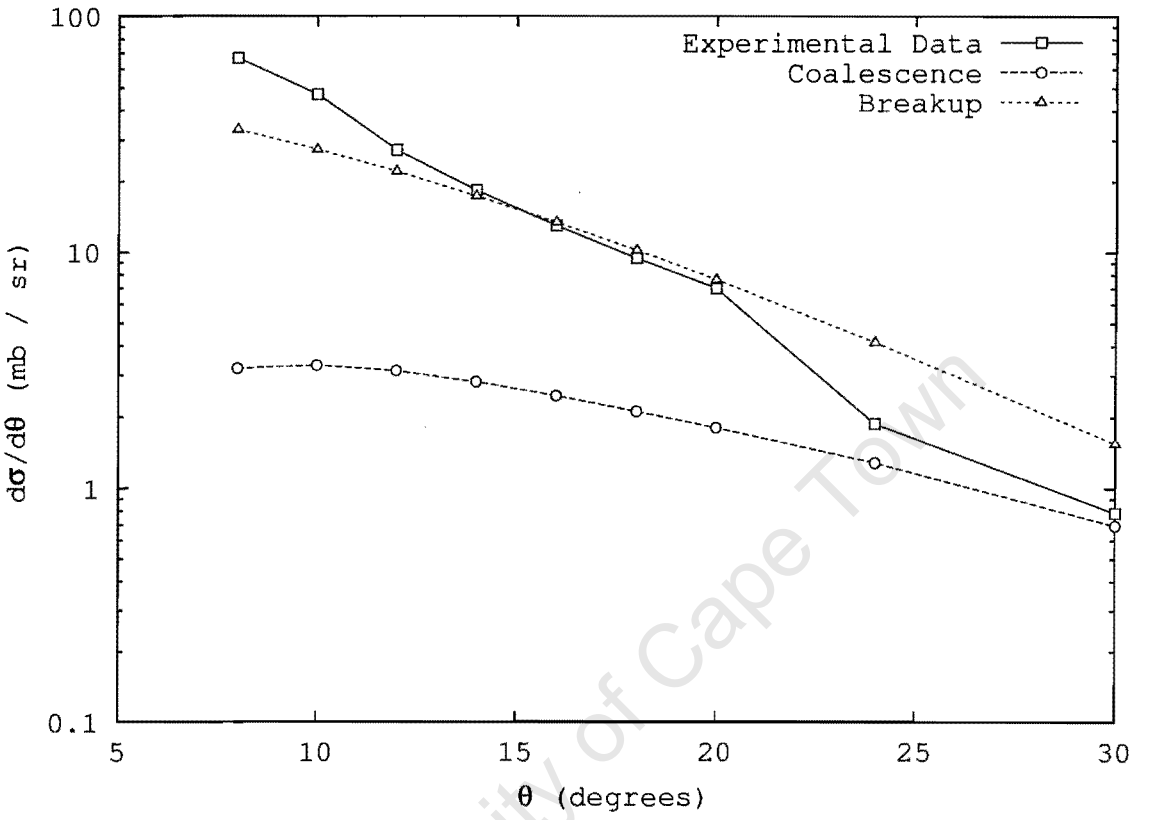

Figure 6.13: Comparison between calculated energy-integrated cross-sections of ^{7}Be at a beam energy of 200 MeV, and experimental angular distribution at the same energy. The contributions from breakup and coalescence are shown separately, with the latter represented by the open circles and the former represented by open squares; the experimental data points are represented by the open triangles. The points are connected by solid (experimental), dashed (coalescence) and dotted (breakup) lines, as a guide to the eye. Note that the total theoretical prediction is the sum of both theoretical components

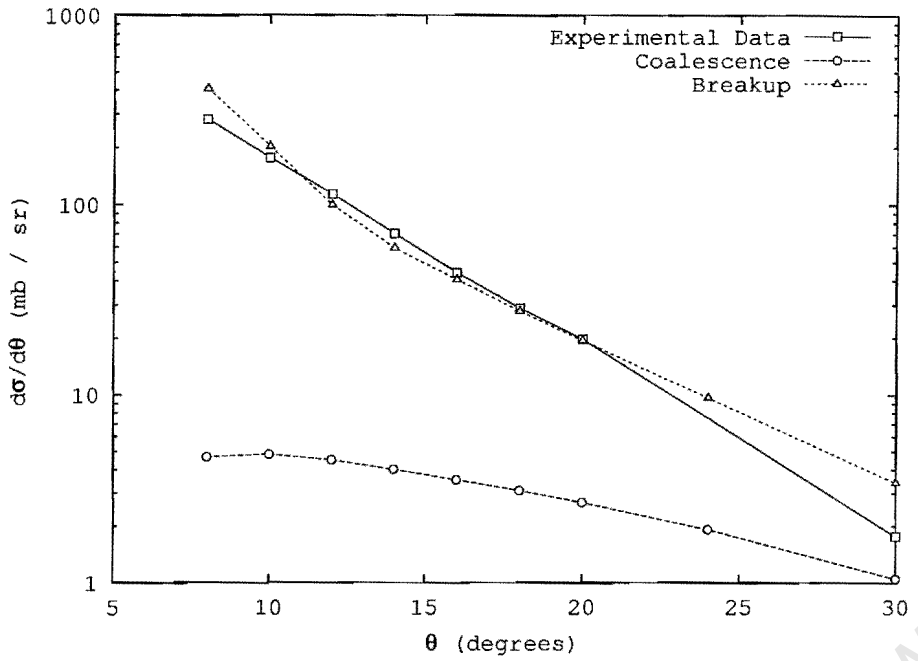

Figure 6.14: Comparison between calculated energy-integrated cross-sections of ^{9}Be at a beam energy of 200 MeV, and experimental angular distribution at the same energy. See the caption to figure 6.13

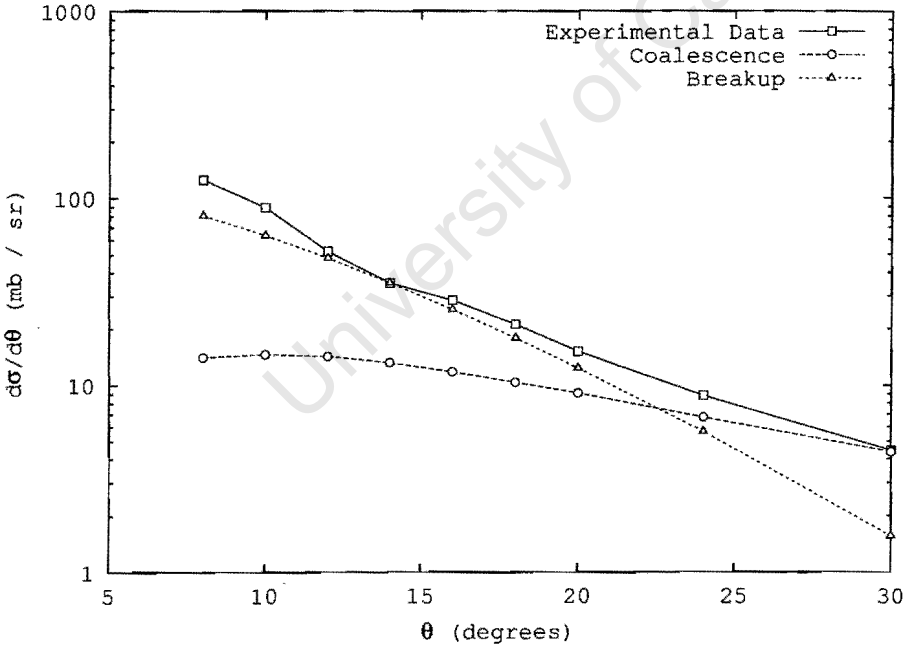

Figure 6.15: Comparison between calculated energy-integrated cross-sections of ^{7}Be at a beam energy of 300 MeV, and experimental angular distribution at the same energy. See the caption to figure 6.13

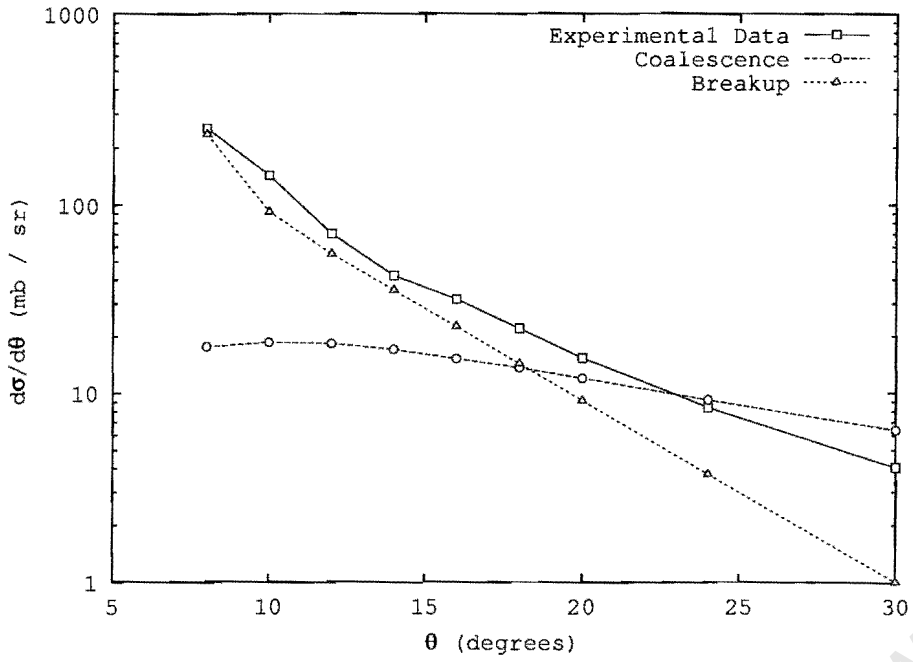

Figure 6.16: Comparison between calculated energy-integrated cross-sections of ^{9}Be at a beam energy of 300 MeV, and experimental angular distribution at the same energy. See the caption to figure 6.13

10° and 16°, there seems to be a slight overestimation of the ^{7}Be cross-section, but it is not significant. On the other hand, for ^{9}Be, there is a significant overestimation of the cross-section at large angles ($\theta > 20°$).

The most noticeable discrepancy between the data and the theoretical predictions at 400 MeV is that the experimental cross-section is highly underestimated at large angles. Once again, the theoretical prediction underestimates the data at small angles for ^{7}Be (see figure 6.17) and overestimates the data in the same region for ^{9}Be (see figure 6.18). In the case of ^{9}Be, in the angular range of $10° < \theta < 16°$, there is almost an identification of the experimental data with the calculated breakup contribution. This might lead one to suspect that the contribution from coalescence in this range is suppressed. Since the coalescence contribution is this region is nevertheless almost an order of magnitude smaller than the corresponding breakup contribution, a further suppression would not have much effect.

In general, it can be stated that the model shows significant deviations from

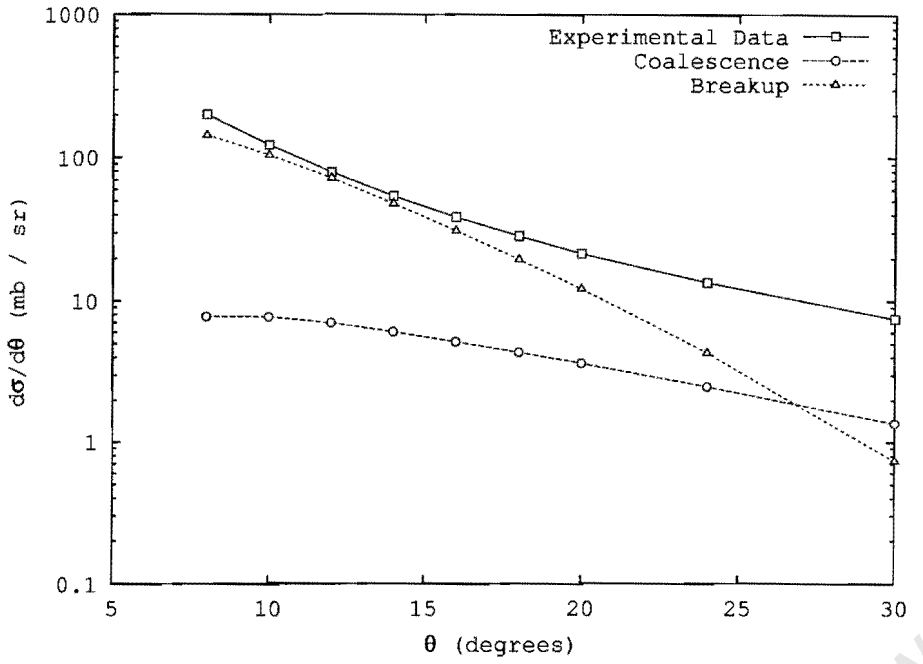

Figure 6.17: Comparison between calculated energy-integrated cross-sections of ^{7}Be at a beam energy of 400 MeV, and experimental angular distribution at the same energy. See the caption to figure 6.13

the data at small angles, where the theoretical predictions tend to overestimate the angular distribution of ^{9}Be and underestimate ^{7}Be, and at large angles, where the total cross-section is underestimated in certain cases.

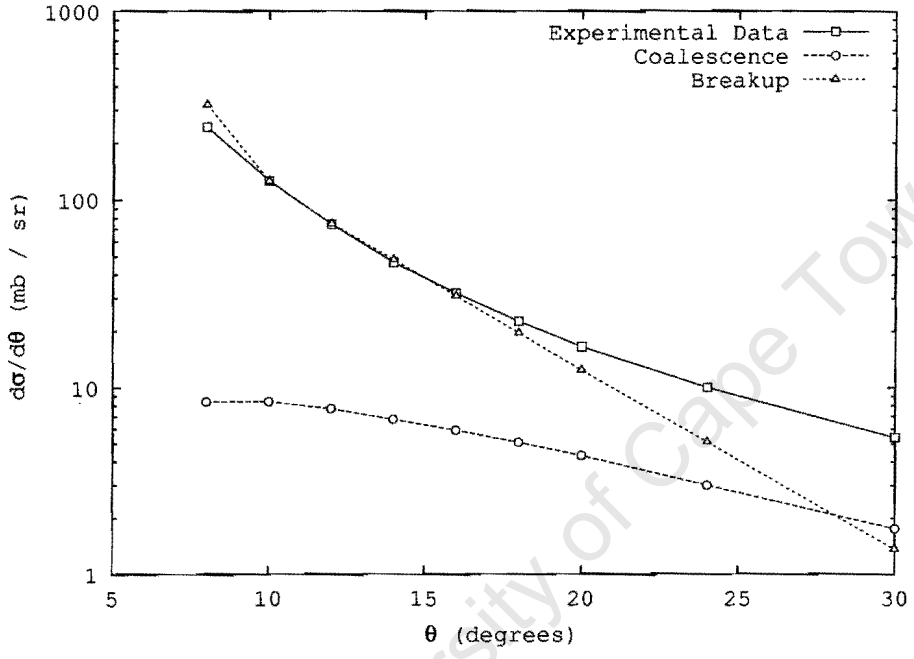

Figure 6.18: Comparison between calculated energy-integrated cross-sections of ^{9}Be at a beam energy of 400 MeV, and experimental angular distribution at the same energy. See the caption to figure 6.13

Chapter 7

Conclusion & Summary

7.1 Overview

The aim of this work was to investigate the isotopes ^{7}Be and ^{9}Be created in the interaction of ^{12}C with a heavy target. A medium mass target, ^{93}Nb was chosen. As is detailed in section 3.4, the choice of target was dictated by the physics we wished to observe since, with a mass of around $100A$, it was not too heavy (and would be thus be fairly stable against fission decay) and not too light (which would not allow sufficient nucleon interactions to justify a statistical model such as BMET). The isotopes of interest had been noticed previously while investigating the energy spectra of ^{8}Be in a reaction similar to the present one. Since it is known that ^{8}Be is created primarily in elastic breakup reactions, the question was posed as to whether it's neighbours ^{7}Be and ^{9}Be were created in a similar fashion, or whether some other reaction channel was open to them. With this in mind, an experiment was designed to accurately measure the cross-sections of these ions.

As is described in chapter 4, the calibration of the stopping NaI E detectors was of crucial importance to the interpretation of the data and a model of the detector response had to be implemented in order to rigorously calibrate them. This model of the detector showed that the nonlinear part of the detector response depends on both the mass and charge of the detected ion, whereas only the linear part was dependant

only on the charge of the detected particle.

A theoretical approach very similar to the one taken before when describing the spectra and angular distributions was applied to the cross-sections of the ^{7}Be and ^{9}Be fragments. A friction-dissipative breakup mechanism was shown to be adequate when reproducing the overall shape of the experimental data, although certain deviations from the model were observed. This would seem to suggest that final-state interactions between the ejectile and residue are not a significant contribution to the total cross-section. Recent calculations done by our theoretical collaborators in Milano have shown that when one tries to take into account a final-state interaction between ejectiles, the agreement deteriorates significantly, further leading one to reject such reaction mechanisms as a valid exit channel [31].

7.2 Summary of experimental data and theoretical description

Adopting an inelastic breakup mechanism as the origin of the observed ^{7}Be and ^{9}Be, theoretical cross-sections were calculated, taking into account contributions from friction-dissipative breakup and coalescence, as described in chapter 2.

In terms of the friction dissipative breakup mechanism (see section 2.4), the parameters needed to reproduce the data best are given in tables 6.4 and 6.6. For completeness, a table showing the resulting parameters for ^{8}Be is shown too. Table 6.6 shows that when ^{12}C fragments into a ^{9}Be and ^{3}He, the heavier fragment (Be) loses less energy than is the case for breakup into ^{7}Be and ^{5}He. This is quite reasonable, since the corresponding trajectory should be further from the target, where it experiences a much smaller nuclear interaction. This is due to the fact that the wavefunction describing the relative motion of ^{9}Be and ^{3}He is an $l = 1$ state and thus more spatially separated.

The presence of ^{9}Be and ^{7}Be was at first thought to suggest that nucleon-transfer type reactions might also be present and it was thought that these nearby isotopes

might have found their origin in the ^{8}Be that were involved in the initial breakup reaction of ^{93}Nb (^{12}C,^{8} Be).

It has been shown that this is very likely not the case, since the spectra of ^{7}Be and ^{9}Be are generally quite well-described by using the *exact* same formalism as that used when describing the ^{8}Be spectra previously. Since the ^{8}Be is so unstable, consisting merely of two spatially correlated α particles [1] with correlated momenta, the very fact that one observes it in a breakup reaction would imply that it was created in the entrance channel [13]. It is possible that it may undergo some sort of neutron-transfer reaction, but it is far more likely that the result of such a reaction would be to destroy the correlation of the two α's, resulting in the production of a ^{5}He+^{4}He pair in the case of pickup, or a ^{3}He +^{4} He in the case of stripping. Since our experiment was designed to detect the Be fragments, however, we would not have been able to resolve any of the He ejectiles.

As seen from the figures in chapter 6, we may note that the spectral shape is generally well reproduced, except at the lowest emission angles, where the absolute value of the breakup contribution is also underestimated. The extra normalisation factors that had to be applied to the calculated breakup spectra at these small emission angles is indicative of a discrepancy between the data and the theoretical description. It appears too that there is an increased asymmetric contribution at lower energy to the breakup peak, especially at larger angles (above 18°).

A possible explanation for the disagreement between the data and the theory in this range may lie in the implementation of our friction folding function. As calculated in this work, the factor which describes the breakup probability per unit energy loss, kk' has been made angle independent. This is a rather naïve approach, which was used as a starting point in the investigation of the friction-dissipative mechanism. It is not unreasonable to think that the value of kk' may depend on the angle of emission (as is suggested by inelastic scattering data), increasing with increasing angle. Indeed, this

[1] In fact, this is exactly what was investigated during the experiment which is referred to above. Pairs of α particles closely correlated in time, with energies which implied that they originated from the same ^{8}Be, were detected during the experiment at NAC in 1998.

study suggests fairly strongly that progress may be made in this direction.

On the whole, it can be confidently stated that the friction-dissipative breakup interaction is a good description of the double-differential cross-sections of ^{7}Be and ^{9}Be produced in the interaction of ^{12}C with ^{93}Nb. Having said that, it was also shown that there are areas where the agreement between model and experimental data are less impressive, notably at low emission angles. It is unclear, however, whether the observed disagreements between the data set at 200 MeV and the theoretical predictions are due to deficiencies in the theoretical description or due to experimental uncertainties introduced when selecting isotopes.

This thesis shows that there is certainly room for further investigation and has provided a useful set of data against which to compare and refine the theoretical predictions in the future.

Appendix A

Fitting the Theoretical Curves to the Data

A code was written (VERNOCA.F90) that calculated the theoretical breakup cross-section, given the experimental situation (beam energy, angle of emission, *etc*). The output from this code had to be fitted to the data to obtain the optimal parameters of interest, most notably the normalisation and the energy shift of the peak. A method was found which does thus numerically, by R. D. Lockett [68], using the *cross-covariance function* of the data and theoretical curve. A brief explanation of this method of non-linear least-squares fitting will follow.

A.1 Discrete Cross-Covariance Function DCCF

For two general functions $f(t)$ and $g(t)$, we can define their cross-covariance function as

$$i(\tau) = \int_{-\infty}^{\infty} f(\tau)g(t-\tau)d\tau$$

In an experimental situation, when one is dealing with real data points, the *discrete* version of the above expression is of more use :

$$I_i = \frac{\sum_{j=i+1}^{N} F_j G_{j-i}}{\sqrt{\sum_{j=i+1}^{N} F_j^2 \sum_{j=1}^{N-i} G_j^2}}$$

and for $i \geq 1$, $i < 0$, this becomes:

$$I_i = \frac{\sum_{j=i}^{N+i} F_j G_{j-i}}{\sqrt{\sum_{j=i}^{N+i} F_j^2 \sum_{j=i-1} G_j^2}}$$

Now I_i has it's maximum when F_i and G_i are maximally overlapped.

The normalised cross-covariance function is the same as a non-linear least-squares fit. For F_i and G_i, the normalised non-linear least-squares minimisation criterion is written as:

$$\alpha_{min}^{j} = min \left[\sum_{i=1}^{N-j} \left(\frac{F_i}{\sqrt{\sum_{k=1}^{N-j} F_k^2}} - \frac{G_{i+j}}{\sqrt{\sum_{k=j}^{N} G_k^2}} \right)^2 \right]$$

where the parameter j would become the energy shift that we are interested in, later. Here F_i and G_i are normalised to their root mean-square values. Multiplying out, we can write :

$$\alpha_{min}^{j} = min \left[2 - 2 \left(\frac{\sum_{i=1}^{N-j} F_j G_{i+1}}{\sqrt{\sum_{i=j}^{N-j} F_j^2 \sum_{i=j}^{N} G_j^2}} \right) \right]$$

The minimum of α occurs when the second term (let's call it β) is a maximum:

$$\beta^{j} = \frac{\sum_{i=1}^{N-j} F_j G_{i+1}}{\sqrt{\sum_{i=j}^{N-j} F_j^2 \sum_{i=j}^{N} G_j^2}}$$

The above expression was coded into a FORTRAN subroutine (`DCCF`), which was included into the code that generated cross-sections from the expression of Vergani *et al.* [27]. The calculated theoretical spectra and the experimental spectra were compared via the cross-covariance function and a shift was found for each set of data that would maximally overlap the two arrays. This shift would then be scaled to give an energy loss parameter. The theoretical spectra were calibrated with respect to the experimental data via a parameter

$$\lambda = \frac{max\,(\sigma_{exp})}{max\,(\sigma_{th})}.$$

When calculating this, one would assume that the maximum of the theoretical cross-section should coincide with that of the experimental cross-section. All of the calculated theoretical data points were then scaled by this parameter :

$$\sigma_{th}\,(i) \longrightarrow \lambda \cdot \sigma_{th}\,(i)$$

These new (shifted and calibrated) calculated cross-sections were then fitted to the experimental data, using a nonlinear least-squares routine - the 'Levenberg-Marquardt' minimisation procedure. In this case, it was called as a built-in `FORTRAN-IMSL` math library [69].

A parameter which determined not only the relative magnitude of the calculated cross-section, but also it's width was the binding energy ε of the fragments within the projectile (see chapter 2). The binding energy is not a well-defined, calculable number and as such, it was estimated by minimising the cross-covariance function while varying ε. Again, the `FORTARN-IMSL` library was used. To find an optimal value for the binding energy, we compared the all the calculated spectra to their respective experimental spectra, while varying the binding energy. The calibration coefficients of the calculated spectra are related to the cross-section and their angular dependance is of interest. Once all the normalisation coefficients were calculated for a particular ion and energy, their respective values were normalised to the value at 8° (*cf* Matsuoka *et al.* [16]) and written to a file.

A.2 Results of the DCCF fit

Figures A.1 and A.2 show the angular dependance of the normalisation constant on the emission angle θ. It is seen that even the estimated points follow an exponential trend quite well, as stated in the literature by, amongst others, Gadioli *et al.* [12, 13, 14].

		200 MeV		300 MeV		400 MeV
θ	^{7}Be	^{9}Be	^{7}Be	^{9}Be	^{7}Be	^{9}Be
8°	$1.843 \cdot 10^{2}$	$9.764 \cdot 10^{2}$	$1.124 \cdot 10^{2}$	$3.187 \cdot 10^{2}$	$9.697 \cdot 10^{1}$	$1.760 \cdot 10^{2}$
10°	$1.295 \cdot 10^{2}$	$6.246 \cdot 10^{2}$	$8.459 \cdot 10^{2}$	$1.835 \cdot 10^{2}$	$6.324 \cdot 10^{1}$	$9.838 \cdot 10^{1}$
12°	$8.114 \cdot 10^{1}$	$3.844 \cdot 10^{2}$	$5.304 \cdot 10^{1}$	$9.689 \cdot 10^{1}$	$4.527 \cdot 10^{1}$	$6.329 \cdot 10^{1}$
14°	$5.470 \cdot 10^{1}$	$2.386 \cdot 10^{2}$	$3.640 \cdot 10^{1}$	$6.144 \cdot 10^{1}$	$3.265 \cdot 10^{1}$	$4.362 \cdot 10^{1}$
16°	$4.015 \cdot 10^{1}$	$1.638 \cdot 10^{2}$	$3.435 \cdot 10^{1}$	$5.278 \cdot 10^{1}$	$2.703 \cdot 10^{1}$	$3.361 \cdot 10^{1}$
18°	$3.127 \cdot 10^{1}$	$1.164 \cdot 10^{2}$	$2.805 \cdot 10^{1}$	$4.147 \cdot 10^{1}$	$2.354 \cdot 10^{1}$	$2.818 \cdot 10^{1}$
20°	$2.398 \cdot 10^{1}$	$8.980 \cdot 10^{2}$	$2.215 \cdot 10^{1}$	$3.118 \cdot 10^{1}$	$2.071 \cdot 10^{1}$	$2.242 \cdot 10^{1}$
24°	no peak vis.	no peak vis.	$1.834 \cdot 10^{1}$	$2.240 \cdot 10^{1}$	$1.906 \cdot 10^{1}$	$1.743 \cdot 10^{1}$
30°	3.980	$1.666 \cdot 10^{1}$	no peak vis.	no peak vis.	no peak vis.	no peak vis.

Table A.1: Table of approximate relative normalisation coefficients used in the calculation of predicted spectra, using the formalism of Vergani *et al.*. The entries labelled *no peak visible* denote spectra where the normalisation could not be unambiguously determined.

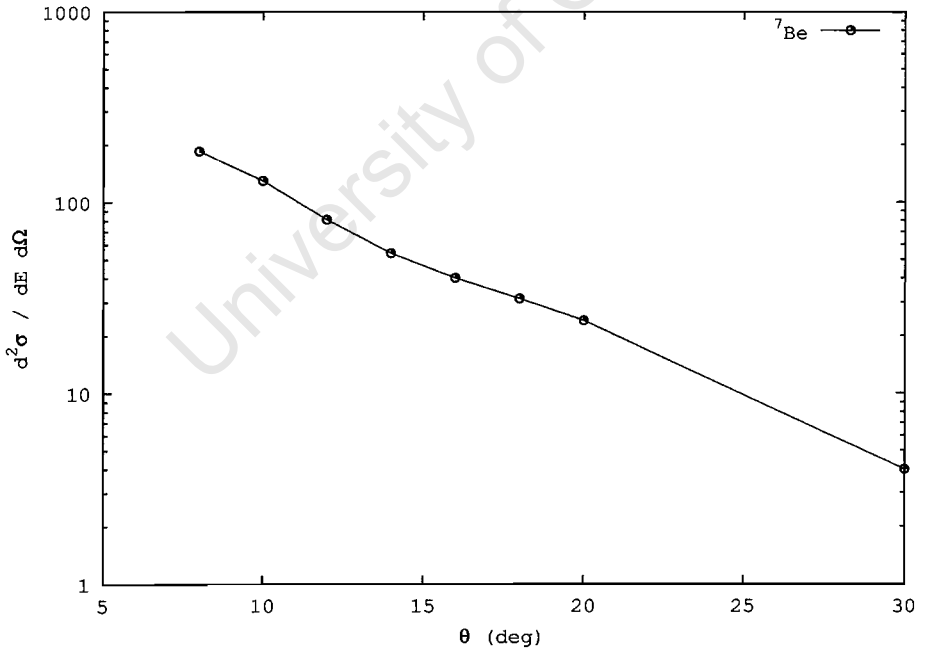

Figure A.1: Angular dependance of the the normalised cross-section of ^{7}Be at an incident energy of 200 MeV

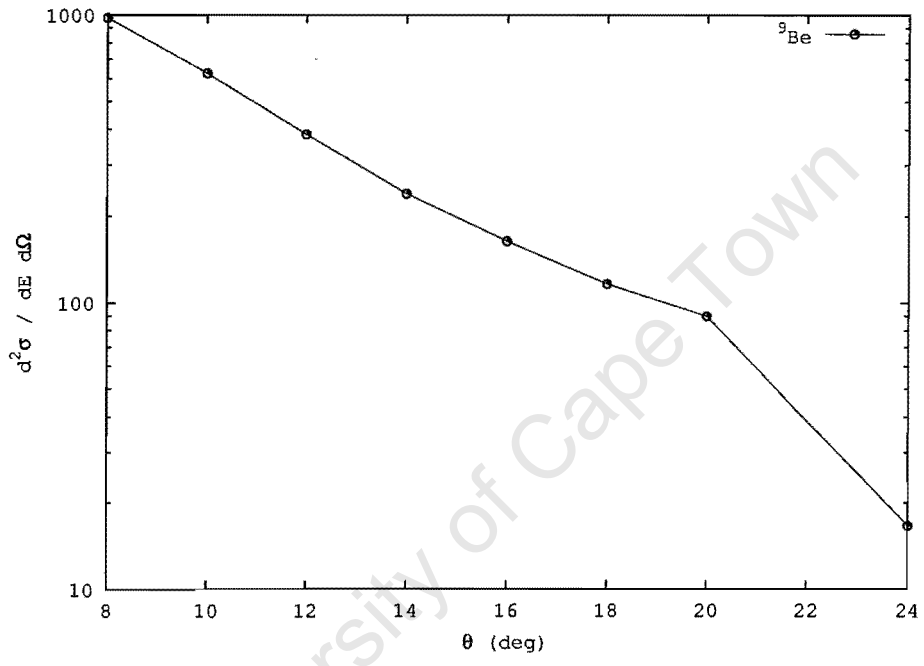

Figure A.2: Angular dependance of the the normalised cross-section of ^{9}Be at an incident energy of 200 MeV

Appendix B

Other reaction mechanisms

Although the main reaction mechanisms encountered during the analysis of the data were outlined in chapter 2, we will make a note here of other interactions which were nonetheless important or present.

B.1 Statistical evaporation

Statistical evaporation is the last stage in the decay chain of an excited nucleus. The theory of Hauser and Feshbach [65], developed over 40 years ago describes in a statistical manner, the probability of an excited nucleus to decay to a lower energy state via γ emission. One is not likely to observe the effects of evaporation in an experiment such as ours.

B.2 Elastic Scattering

The elastic scattering of nuclei was indirectly important to our experiment. Although we were not aiming to detect and analyse the cross-sections of elastically scattered ^{12}C, the elastic scattering process was used to calibrate our detectors (see chapter 4) and for beam offset measurements (see chapter 3).

Appendix C

Acknowledgements and Thanks

I would like to thank the following people and organisations who directly contributed to the success of this project. Their knowledgable advice, suggestions and comments made the experiment and the write-up all the more enjoyable:

Dr. Zeblon Vilakazi who took a chance on me and guided me expertly through the initial stages of my project

Dr. Simon Connell whose invaluable advice, leadership and experience as a physicist have come in handy many times over the past 2 years

Dr. Deon Steyn for many (patient) discussions that helped me to gain amongst other things a better understanding of the experimental and data analysis procedures that were used during this experiment

Drs Siggie Förtsch, Ricky, Kobus Lawrie for all their help during the experiment and after

Dr. Elias Sideras-Haddad at Schonland who was always a great wealth of knowledge and motivation during late-night experimental runs and conference after hours.

beam technicians for doing their best to give us decent beams

John Pilcher for his helpful assistance during data replay at NAC

Sean Murray and David Roux for many lifts to and from NAC and help learning the software at NAC during the beginning phase of the analysis

Mark Horner and Sahal Yacoob for keeping me motivated and making life bearable at varsity. Special thanks to Mark for teaching me the value of airstrikes and ponytails; Sahal for the Del Mar legend.

Prof. Ettore Gadioli and his fine team of theoreticians, for all the theoretical guidance and hospitality while visiting Milano. Special thanks to Francesca Albertini, who made sure that I received all of the theoretical calculations quickly.

Dr. Karo Michaelian for his great scintillation-modelling code which made the calibration of the NaI(Tl) E detectors possible

Korir who always managed to confuse me, when discussing the theory at leisure, but who always had a apoint.

Prof. Brooks , ever-present next door, who always gave me a guilty conscience when I felt tired and thought about quitting for the day... I couldn't quit when a *retired* prof was still here a\h !!

This project would not have been possible without the financial support of the following institutions :

- A grant-holders bursary from the NRF (thanks Simon)
- Ablett scholarship fund, NAC and NRF mobility grant for my trip to the 2nd International Balkan School on Nuclear Physics in Bodrum, Turkey and my working visit to the dipartmento di fisica nucleare all'università degli Studi di Milano in September 2000
- The Joseph Stone scholarship fund of UCT.

This document was prepared with **MikTeX 2.1**, made immeasurably easier with the help of **WinEdt 5**. Many figures were prepared with el plotting routine magnifico, **GnuPlot**. You guys rock... seriously...

Although the aforementioned persons directly played an important role in the success of this thesis, there are those souls without whom I could just not have gotten up some mornings, and without whom life would've just been too dreary to continue. I would like to thank the following for (by happy coincidence, or design) preventing me from giving up and joining the Marines or something. In absolutely no order whatsoever :

J. L. Hooker, the Tsitsikamma forest, B. B. King, Cynthia at Schonland, C. J. DuPree, H. Wolf, G. Puccini, G. Verdi, M. Bizet, R. Wagner, Beethoven, P. Merrimée, P. J. O'Rourke, A. de Saint-Exupéry, Sgt. A. McNabb DCM MM, E. A. Poe, E. Piaf, C. Filosofov, A. C. Milan, C. dos Santos Fernandes, V. Hugo, D. Dobur, M. R. Chi, E. Girolo, J. P. Goldstone, J. Daniels, Pericles, J. Sutherland, F. Pessoa, Christina. G. Rosetti, J. Beam, my kleinsus Jade en my grootsus Shael, S. Rachmaninov, Cpt. A. Corelli, M. Kaichis, C. Debussy, K. Fleming, W. A. Mozart, Mirko, bar staff of 'Halikarnas', 'Vacca Matta' and CornerHouse, Madame H. Czèrniwicz, D. G. Aschman, K. Twynam, M. Cervantes, A. Massaferri, Jenn, Sarah, l'Alhambra, espresso & nutella makers everywhere, Val & Eran and their fantastic large coffee, L. Pavarotti, G. J. Gibbon, M. Gagliano, M. Freni, R. Tebaldi, F. C. Valencia, J. Carréras, A. Dainty, H. Boden, S. Blyth, H. Troyat, Plato, E. M. Sorenson, Cahit S. Tarançı, Nicoletta, J. Livingstone-Seagull, F. Albertini, Dilbert, C. Giannoccaro, C. mcKinnon, Weatherman Pete, Garfield, oilve grissini, my beloved car Catherine-Anne West, J. Brèl, O. Redding, Alpen Tropical Muesli, Themistocles, Pooh, E. Brontè, A. Gide and Prof. B. Warner, who inadvertently set this beautiful process in motion.

Finally, thanks to my mother for her unfailing support and interest in my work.

Bibliography

[1] U. Schröder and J. R. Huizenga, *Treatise on Heavy-Ion Science* (New Tork-Plenum) pp113 - 726

[2] C. Grégoire and B. Tamain, Annals of Physics **11** (1986), p323-455

[3] C. K. Gelbke and D. H. Boal, Progress in Particle and Nuclear Physics **19** (1987), pp33-106

[4] C. K. Gelbke, D. K. Scott, M. Bini, D. L. Hendrie, J. Mahoney, M. C. Mermaz and C. Olmer, Physics Letters **70 B** p415-417

[5] H. Fuchs and K. Möhring, Reports on Progress in Physics **57** (1994), p231

[6] H. Frölich, T. Shimoda, M. Ishihara, K. Nagatani, T. Udagawa and T. Tamura, Physical Review Letters **42** (1979) pp 1518-1520

[7] T. Udagawa, T. Tamura, T. Shimoda, H. Frölich, M. Ishihara and K. Nagatani, Physical Review **C20** (1979), pp 214-221

[8] T. Udagawa, D. Price and T. Tamura, Physics Letters **116B** (1982), pp 311-314

[9] K. W. McVoy and M. C. Nemes, Z. Physik **A295** (1980), pp 177-186

[10] M. S. Hussein, K. W. McVoy and D. Saloner, Physics Letters **98B** (1981), p162

[11] E. Gadioli *et al* , Physics Letters **B 394** (1997), pp 29-36

[12] E. Gadioli *et al* , Nuclear Physics **A641** (1998), p 271

[13] E. Gadioli *et al* , Nuclear Physics **A654** (1999), pp 523-540

[14] E. Gadioli *et al* , European Journal of Physics **A8** (2000), pp 373-376

[15] R. Serber, Physical Review **72** (1947), p 1008

[16] N. Matsuoka *et al* , Nuclear Physics **A311** (1978), pp 173-187

[17] E. Gadioli & P. E. Hodgson, *Pre-Equilibrium Nuclear Reactions*, Oxford University Press (1992)

[18] E. Gadioli *et al.*, Proceedings of the 9^{th} Inernational Conference on Nuclear Reaction Mechanisms, Varenna (2000)

[19] R. Bimbot, D. Gardès and M. F. Rivet, Nuclear Physics **A 189** (1972), pp 193 - 219

[20] K. Siwek-Wilcyńska, E. .H. du Marchie van Voorthuysen, J. van Popta, R. H. Siemssen and J. Wilczyński, Nuclear Physics **A 330** (1979), pp 150-172

[21] K. Siwek-Wilcyńska, E. .H. du Marchie van Voorthuysen, J. van Popta, R. H. Siemssen and J. Wilczyński, Physical Review Letters **42** (1979), p 1599

[22] Thesis of Francesca Albertini, Università degli Studi di Milano, 2002 (unpublished)

[23] Thesis of Trevor Stevens, University of the Witwatersrand 2001, unpublished

[24] P. E. Hodgson, E Gadioli and E. Gadioli Erba, *Introductory Nuclear Physics* Oxford University Press (1997)

[25] Y. le Beyec *et al* , Nuclear Physics **A 192** (1979), pp 405 - 416

[26] H. Feshbach and K. Huang., Physics Letters **47B** (1973), p 300

[27] P. Vergani *et al* , Physical Review **C48** (1993), pp 1815-1827

[28] D. J. Parker *et al*, Physical Review **C35** (1987), pp 161-176

[29] A. Bonnaccorso, private communication (September 2001)

[30] D. J. Parker *et al* , Physical Review **C44** (1991),pp1528-1540

[31] Thesis of Chiara Catarisano, Università degli studi di Milano, 2001 (unpublished)

[32] J. J. Griffin, Physical Review Letters **17** (1966), p 478

[33] G. Harp, J. Miller and B. J. Bern, Physical Review **165** (1968), p1166

[34] G. Harp, J. Miller and B. J. Bern, Physical Review **C 3** (1971), p1847

[35] M. Blann, Physical Review **C 23** (1981), p205

[36] M. Blann, Physical Review **C 31** (1985), p1245

[37] E. Fabrici *et al.*, Physical Review **C 40** (1989), p2548

[38] E. Fabrici *et al.*, Physical Review **C 42** (1990), p2163

[39] E. Fabrici *et al.*, Zeitschrift Für Fisik **A 338** (1991), p17

[40] M. Cavinato *et al.*, Zeitschrift Für Fisik **A 347** (1994), p237

[41] M. Cavinato *et al.*, Physics Letters **b 382** (1996), p1

[42] M. Cavinato *et al.*, Physics Letters **B 405** (1997) p 219-233

[43] M. Cavinato *et al.*, Nuclear Phyics **A 643** (1998), pg 15-29

[44] Dr. G. F. Steyn, private communication (December 2001)

[45] J.B. Birks, Physical Review **86** (1952), 569

[46] E.J. Kobetich and R. Katz, Physical Review **170** (1968), 391

[47] E.J. Kobetich and R. Katz, Physical Review **170** (1968), 397

[48] K. Michaelian, A. Menchaca-Rocha, E. Belmont-Morena, Nucl. Instr. & Methods. **A356**, (1994), 297

[49] K. Michaelian and A. Menchaca-Rocha, Phys. Rev. **B 49**, (1995) 15550

[50] M. Pârlog *et al.*(INDRA collaboration), arχiv:nucl-ex/0106002 (2001)

[51] M. Pârlog *et al.*(INDRA collaboration), arχiv:nucl-ex/0106003 (2001)

[52] N. Colonna *et al.*, Nuclear Instrumentation and Methods **A321** (1992), 529

[53] W. R. Leo, Techniques in nuclear and particle physics experiments, Springer-Verlag (1994)

[54] J. Lindhart, M. Schaaf and H. E. Schiott, Math. -Fys. Meddr. **33**, (1963), 1

[55] E. C. Montenegro, S. A. Cruz and C. Vargas-Alberto, Phys. Lett. **A 92**,(1982), 195

[56] K. Kannaya and S. Okayama, J. Phys. D: Applied Physics **5**, (1972), 43

[57] K. Michaelian, private communication, 2000

[58] K. Michaelian, private communication, 2000

[59] G.F. Knoll *Radiation detection and measurement* , Wiley & Sons, New York (1979)

[60] J. B. Birks, *"Theory and practice of scintillation counting"*, Pergammon Press, New York (1964)

[61] S. Förtsch, PhD thesis, University of Pretoria (unpublished), 1992

[62] E. Gadioli and E. Gadioli Erba, Zeitschrift Für Fisik **A 299** (1981) p1

[63] E. Gadioli *et al.*, private communication (2001)

[64] E. Gadioli *et al.*, private communication (2001)

[65] P. E. Hodgson, *Nuclear Heavy Ion Reactions.* Clarendon Press, Oxford , 1978

[66] M. Böning, Nuclear Physics **A 152** (1970), p529

[67] Prof. E. Gadioli (private communication), *'Fundamental and Applied Aspects of Modern Physics'* conference, Lüderitz, Namibia (2000)

[68] R.D. Lockett, Ph.D. thesis, unpublished (1991)

[69] Compaq Visual Fortran 90 Manual, *IMSL Math Library Vol. 1* (1999), Visual Numerics

[70] E. Gadioli *et al.*, private communication, Dec. 2001

[71] E. Gadioli, private communication, February 2002